Chapter 3

Applications and Results

In this chapter the theoretical results outlined in the last chapter are applied to different systems. First, the different methods for control of quantum-systems are tested on some model potentials. Then several *ab initio* calculations on exemplary molecules are presented, which are needed for the development of the CRS Hamiltonian for these systems. Finally the dynamics of one of these molecules is studied within the CRS approximation using the MCTDH method.

3.1 Model Systems

Here calculations are presented on one- and two–dimensional model systems of a double minimum potential for the proton transfer reaction. The parameters for the model potential were either chosen in a way to highlight some special feature of the dynamics or fitted to *ab initio* data to represent a specific molecular system.

3.1.1 Driven Quantum Tunneling

The 1d–model system used in this section consists of a slightly asymmetric double minimum potential, which is a generic model case for proton transfer. The potential parameters have been fitted to *ab initio* data for substituted malonaldehyde (presented in Scheme 3.1). In experiments, this molecule allows easy changes of the potential properties by exchanging one of the O–atoms with a different atom, e.g. sulfur. Therefore a wide range of potential shapes can be represented with this type of proton transfer system. In the following calculations the possible coupling of the proton transfer to the heavy atom modes, which would lead to a 2d–model system, is neglected. This leads to a potential for a single reaction coordinate $V(q)$, in the characteristic form of a double minimum potential with the minima located at $q = \pm q_0$ and separated by a barrier of height V^B at or near $q = 0$. The respective energies at these minima are slightly offset by a difference of δ. The appropriate potential

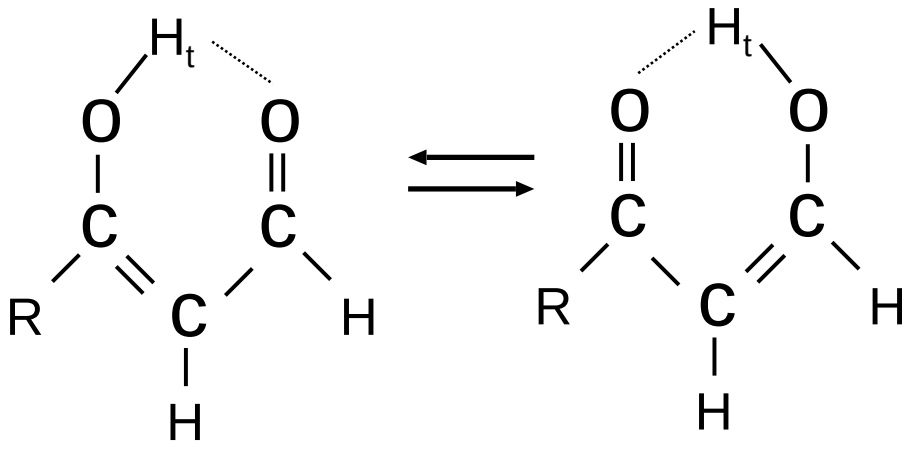

Figure 3.1: By means of a non-symmetric substitution of one of the H atoms in malonaldehyde the previously symmetric double minimum potential describing the transfer of H_t develops a slight energy asymmetry.

is given as

$$V(q) = \frac{\delta}{2q_0}(q - q_0) + \frac{V^B - \delta/2}{q_0^4}(q - q_0)^2 (q + q_0)^2 . \tag{3.1}$$

This potential is shown in Figure 3.2 for a set of parameters taken from Ref. [124] (and given in the figure caption). In this reference the parameters were chosen in accordance with previous theoretical studies on malonaldehyde [125]. The eigenstates and energy eigenvalues resulting from the solution of the stationary Schrödinger equation (2.1) are plotted in Figure 3.2. As can be seen there, the first two levels are nearly degenerate and have eigenfunctions belonging to states being rather localized in either the reactant or product potential well. For this set of parameters all higher lying states are characterized by delocalized wavefunctions, which cannot be clearly associated with one of the minima.

To simulate the isomerization reaction, the system initially was put into a reactant state, represented by the lowest eigenstate Ψ_1 of the potential curve. The coupling to the field was modeled with the semi-classical dipole approximation, as presented in Section 2.5.1. Effects of rotation are neglected, which in effect means that the molecule is kept in a fixed position with respect to the polarization of the electric field. This allows for both the field and the dipole to be treated as a scalar instead of a vector property, resulting in a system Hamiltonian $\hat{\mathbf{H}}_S = \hat{\mathbf{H}}_0 - \mu\mathcal{E}(t)$ depending only on the absolute values of $\mathcal{E}(t)$ and μ. The dipole operator is modeled as a linear function of the proton transfer coordinate in the form $\mu = \mu(q) = eq$ even though the amount of charge transferred during isomerization is likely to be less than one elementary charge e.

The study of this molecular model by Došlić *et al* [125, 124] as an isolated system without coupling to the environment showed the potential of using optimal control strategies

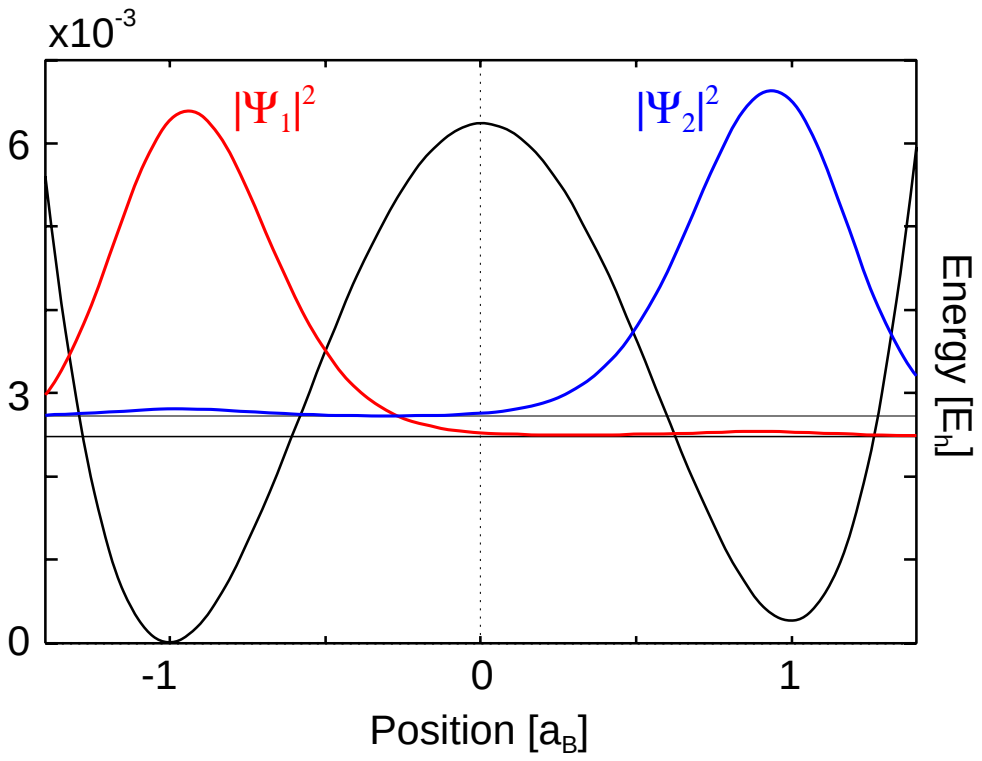

Figure 3.2: Potential, energy levels and the first two eigenfunctions of the system tailored to represent a substituted malonaldehyde. The parameters used for the potential Eq. (3.1) are $V^B = 6.25 \times 10^{-3} E_h$, $\delta = 0.257 \times 10^{-3} E_h$ and $q_0 = 1 a_0$.

to design the necessary laser fields to drive the transfer reaction. In this reference the application of the optimal control theory led to a laser field which initiates a driven quantum tunneling in the system [126]. The optimal control method with a very low penalty factor for the total field intensity produced an optimal field, which quite closely reproduces the field obtained from a pump–dump approach with two analytical $\sin^2$ laser pulses, where the population transfer occurs via a delocalized state above the barrier. Introducing a higher penalty for the allowed time–integrated intensity resulted in a completely different picture: For this set of parameters the algorithm produces an optimal field, which consists mainly of a more or less constant plateau, flanked by short switch on and switch off regions. The population dynamics generated by this field takes place entirely between the lowest two eigenstates Ψ_1 and Ψ_2, as plotted in Figure 3.2. No population is transferred via energetically higher states, delocalized above the barrier. This leads to the conclusion, that the plateau field drives the transfer through and not over the potential barrier. The resulting electrical field not only has a lower maximum intensity, reducing the chance of competing processes like ionization during the transfer, but also reaches the goal of complete isomerization earlier (only 1.5 ps opposed to the 2 ps required for the pump–dump pulse). This

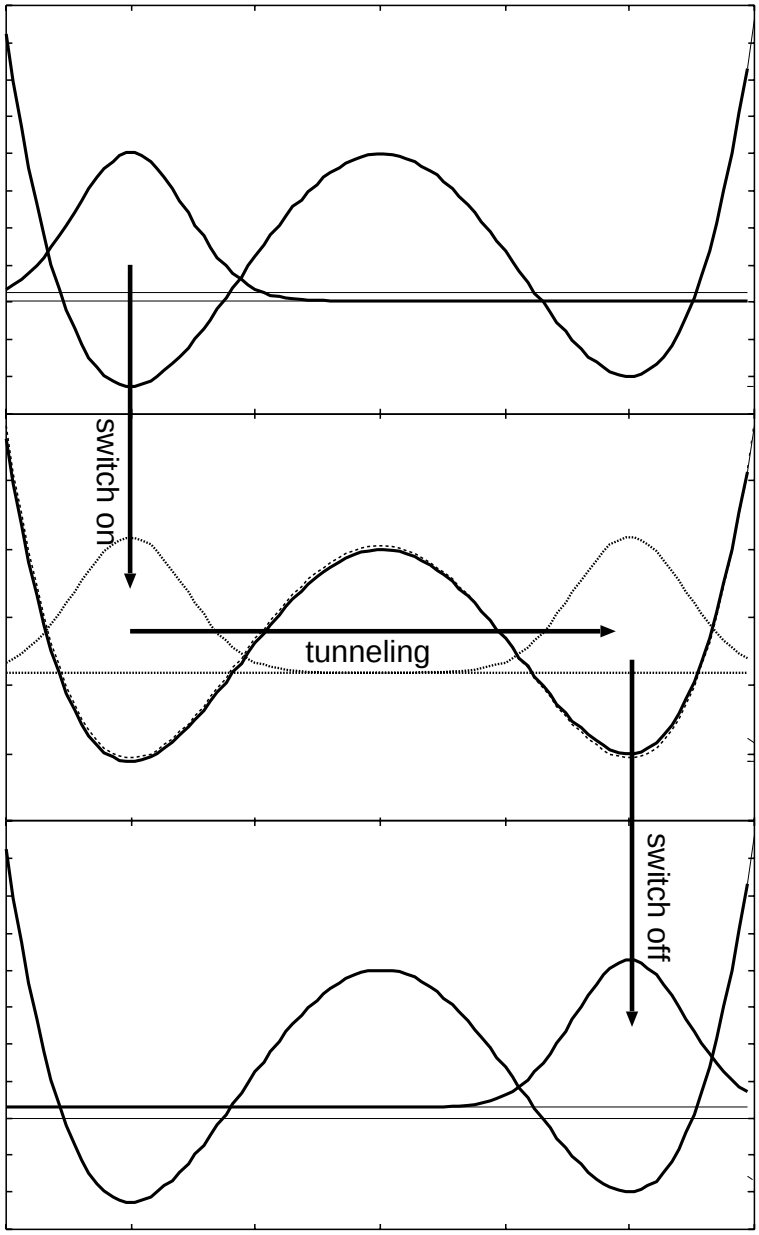

Figure 3.3: The situation before, during and after the plateau field starts to drive the population from the left to the right well (from top to bottom). In the middle panel the effective potential $V - \mu\mathcal{E}$ created by the plateau field is plotted as a dashed line.

reaction pathway is plotted in Figure 3.3 and can be described in the following steps:

1. The initial wavefunction $\Psi(t=0) = \Psi_1$ is an eigenfunction of the undisturbed model potential $V(q)$. During the switch on phase this state is converted into a coherent superposition of the states ϕ_i, obtained from the solution of

$$\left(\hat{\mathbf{H}}_0 - \mu\mathcal{E}_p\right)\phi_i = \tilde{E}_i\phi_i, \tag{3.2}$$

   where $\mathcal{E}_p$ is the plateau field of the pulse and the $\tilde{E}_i$ represent the changed energy eigenvalues of the system.

2. During the plateau phase of the pulse the coherent superposition of these new eigenstates leads to the observed tunneling dynamics. If the field is chosen in such a way, that the two lowest diagonal elements of the perturbed Hamiltonian are exactly degenerate, the population transfer between reactant and product wells are completed within the tunneling time $\tau = h/(4\mathcal{E}_p\mu_{12})$.

3. When the field is switched off after the tunneling time τ the system stabilizes in the – now again stationary – state Ψ_2.

The plateau field, $\mathcal{E}_p$, needed for this process can be calculated from the matrix elements of the Hamiltonian from Eq. (3.2) in the basis $\{\Psi_1, \Psi_2\}$. In this representation the Hamiltonian during the plateau phase is

$$H_{\mathrm{S}} = \left[\begin{pmatrix} E_1 & 0 \\ 0 & E_2 \end{pmatrix} - \mathcal{E}_p \begin{pmatrix} \mu_{11} & \mu_{12} \\ \mu_{21} & \mu_{22} \end{pmatrix}\right]. \tag{3.3}$$

The resonance condition which follows from this expression is

$$E_1 - \mathcal{E}_p\mu_{11} = E_2 - \mathcal{E}_p\mu_{22} \tag{3.4}$$

which can be used to obtain the plateau field $\mathcal{E}_p$. Note, that because of the asymmetry in the potential the two diagonal elements of $\hat{\mu}$ are not equal, which means that the plateau field is not exactly the one that would compensate the asymmetry of the potential of the system given by Eq. (3.1) [127].

Driven Quantum Tunneling with Dissipation

One of the most interesting aspects of the tunneling approach to isomerization is, that the reaction path transfers the population via the lowest possible eigenstates. So in contrast to the pump–dump approach, which has to include at least one higher lying, excited state, this process should allow better control, when the effects of energy dissipation are included into the calculations, as the relaxation rate increases with the energy of the populated levels. In this section the impact of including a generic coupling to an environment within the Redfield–model is examined.

For this the total Hamiltonian is written in the separated form given in Eq. (2.76), with the system part being calculated in the semi-classical dipole approximation, i.e.

$$\hat{\mathbf{H}}_{\mathrm{S}}(t) = \underbrace{-\frac{\hbar^2}{2m}\frac{\partial^2}{\partial q^2} + V(q)}_{\hat{\mathbf{H}}_0} - \hat{\mu}\cdot\mathcal{E}(t) \tag{3.5}$$

and the interaction between the system and the bath being represented by a factorized operator in the form given by Eq. (2.83). The form of the coupling is taken as a standard bilinear term [63, 127, 128]

$$\hat{\mathbf{H}}_{\mathrm{S-B}} = q\lambda^{-1/2}\sum_{\xi}\hbar k^{\xi} Q_{\xi} \tag{3.6}$$

where $\lambda^{1/2}$ is some system specific length scale parameter and k^{ξ} the coupling of the system coordinate to the (dimensionless) oscillator coordinate Q_{ξ} of mode ξ. This environment is completely characterized by the spectral density entering the calculation of the damping matrix given by Eq. (2.116). In the following an Ohmic spectral density of the form

$$\mathcal{J}(\omega) = \alpha\omega e^{-|\omega|/\omega_c} \tag{3.7}$$

is assumed, where ω_c is a system specific cutoff frequency. In order to model in particular the coupling to the low frequency modes of the molecular scaffold which have the most prominent effect on the proton transfer coordinate, $\omega_c/2\pi c$ was taken as $500\,\mathrm{cm}^{-1}$ in all calculations.

The dynamics in this system takes place almost entirely between the lowest two eigenstates, if the tunneling isomerization approach is applied. These two states are, in this low barrier system, sufficiently close to the top of the barrier to have a significant coupling and therefore allow tunneling to take place on a picosecond time scale. To highlight the effects of the laser field and without addressing the possibility of preparing such an initial molecular configuration, all initial population is placed in the lowest molecular eigenstate Ψ_1, which is located in the left hand well, corresponding to $T = 0\,\mathrm{K}$. Due to the fact that the lowest two eigenstates are nearly degenerate, the introduction of an environment with finite temperature then, of course, results in this initial condition being nonstationary. At room temperature the thermal distribution results in an almost 50:50 population distribution between Ψ_1 and Ψ_2 in equilibrium. The laser pulse generated by optimal control in [124], which drives the tunneling from the initially prepared state Ψ_1 into Ψ_2, is replaced by an analytical pulse consisting of $\sin^2$ switch-on and switch-off flanks with a constant plateau field between them. For the studied system the – arbitrarily chosen – length $t_{\mathrm{on}} = t_{\mathrm{off}} = 125\,\mathrm{fs}$ for the switching times, and a plateau field determined from Eq. (3.4) as $\mathcal{E}_p = 0.136\cdot 10^{-3}\,E_h/ea_B$, produced an almost 100% population transfer in the isolated system for a plateau time of $t_p = 1250\,\mathrm{fs}$. The field as well as the resulting dynamics are shown in Fig. 3.4 (solid lines). In Ref. [124] it was pointed out that there is quite some flexibility of this tunneling scheme concerning the pulse shape. Thus the

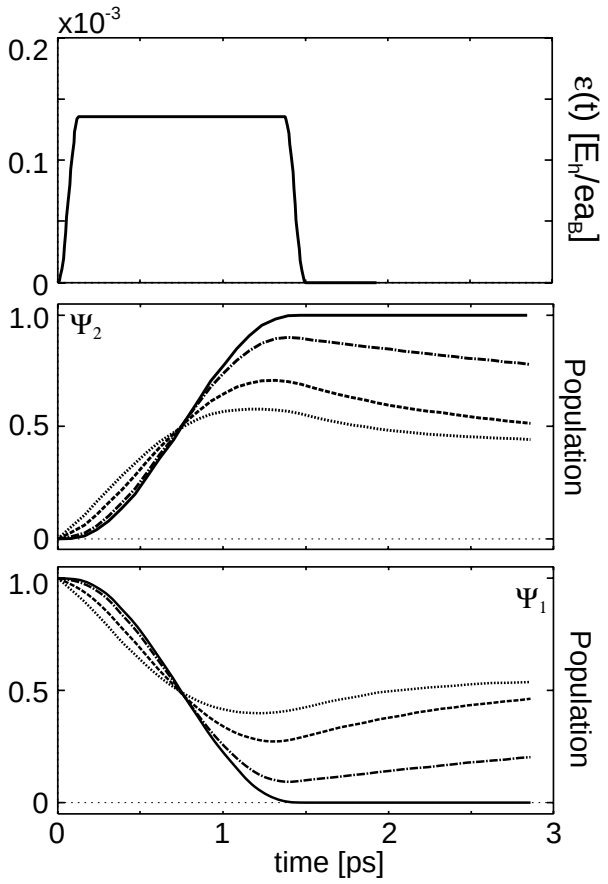

Figure 3.4: The laser pulse used for the isomerization in the system presented in Fig. 3.2. The pulse–parameters are $t_p = 1250\,\mathrm{fs}$, $t_{\mathrm{on}} = t_{\mathrm{off}} = 125\,\mathrm{fs}$ and $\mathcal{E}_p = 0.136 \cdot 10^{-3}\, E_h/ea_0$. In the lower panel the respective populations of the first two eigenstates are given for different strengths of the coupling to the environment: $\alpha = 0$ (solid line), $\alpha = 0.01\lambda$ (dot-dashed line), $\alpha = 0.04\lambda$ (dashed line) and $\alpha = 0.08\lambda$ (dotted line).

choice of the switch–on and switch–off times is rather arbitrary. In the extreme limit of a so–called half–cycled pulse the plateau time would be zero. Interestingly such half–cycled pulses can be generated in the sub-picosecond domain as was demonstrated in Ref. [129].

Upon inclusion of energy and phase relaxation due to the interaction with the dissipative environment, in the Redfield formalism presented in Section 2.4.2, the efficiency of isomerization decreases drastically. To show this, calculations have been performed for different coupling strengths leading to different transfer rates, k_{12}, of the two levels involved. At room temperature the coupling between the tunneling levels is $k_{12} = \alpha\lambda^{-1}/120\,\mathrm{fs}^{-1}$ and $k_{21} = \alpha\lambda^{-1}/93.9\,\mathrm{fs}^{-1}$. For the coupling strengths used here, $\alpha = 0.01\lambda$, 0.04λ, 0.08λ, the initially localized state would thermalize on a time scale greater than 1.4 ps. Thus using a pulse having the total duration of 1.5 ps the calculation are just at the edge where

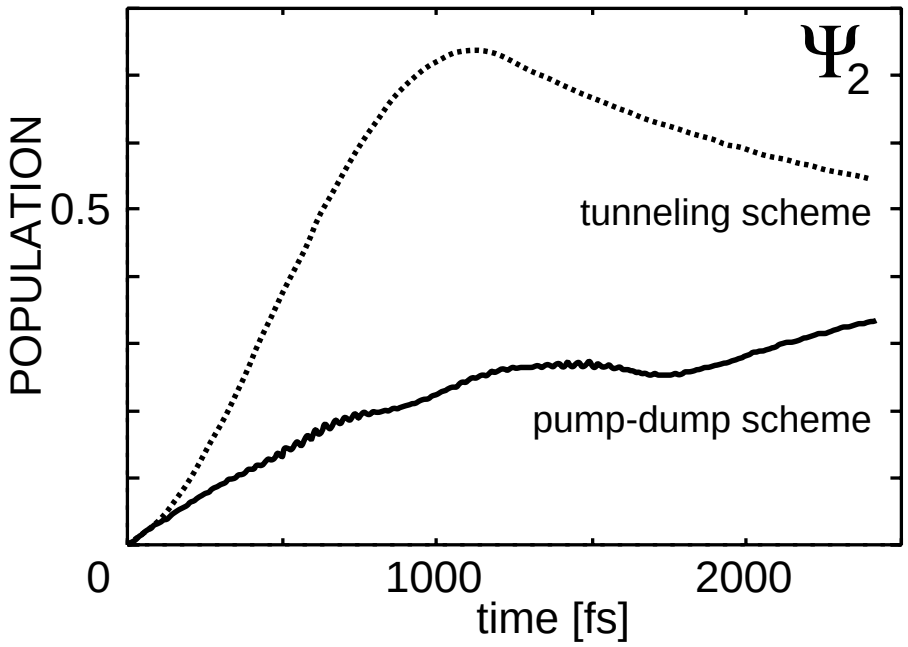

Figure 3.5: Comparison of the transferred population in the right potential well, transferred with the pump–dump scheme, compared to the tunneling method. The dissipation strength for both calculations is set to the medium coupling ($\alpha = 0.04\lambda$).

a non thermal population of Ψ_2, and therefore control can be achieved after the pulse is over. Note, that for finite α the initial depopulation of Ψ_1 is accelerated due to the dissipation, because in addition to the tunnel coupling the transfer now has a channel going via population relaxation. The results of these calculations are presented in Fig. 3.4 for the different coupling strengths used (differently dashed lines). It can be clearly seen, that for the strongest coupling ($\alpha = 0.08\lambda$) the tunneling process just barely manages to create a non-thermal distribution of the population, before the system moves back into equilibrium. The effect of the faster depopulation of the initial level can also be seen clearly.

The big advantage of the isomerization via tunneling in contrast to the pump–dump approach in the presence of dissipation can be seen in Fig. 3.5. This shows the population dynamics of the tunneling process in contrast to the one generated by a pump–dump pulse. In both cases the laser field has been optimized to generate almost complete population transfer from left to right in the isolated system. The resulting pulses were then applied to the same system, but with dissipation included. While the tunnel–field manages to produce a quite significant transfer to the right well, which then slowly decays into thermal equilibrium, the pump–dump–field does not increase the population of Ψ_2 beyond its equilibrium value. The reason for this is, that the population transferred by the pump–pulse into the delocalized above–barrier state, immediately starts to decay back into Ψ_1 and Ψ_2. Due to the high energy difference this happens on a faster time scale than the pulse length,

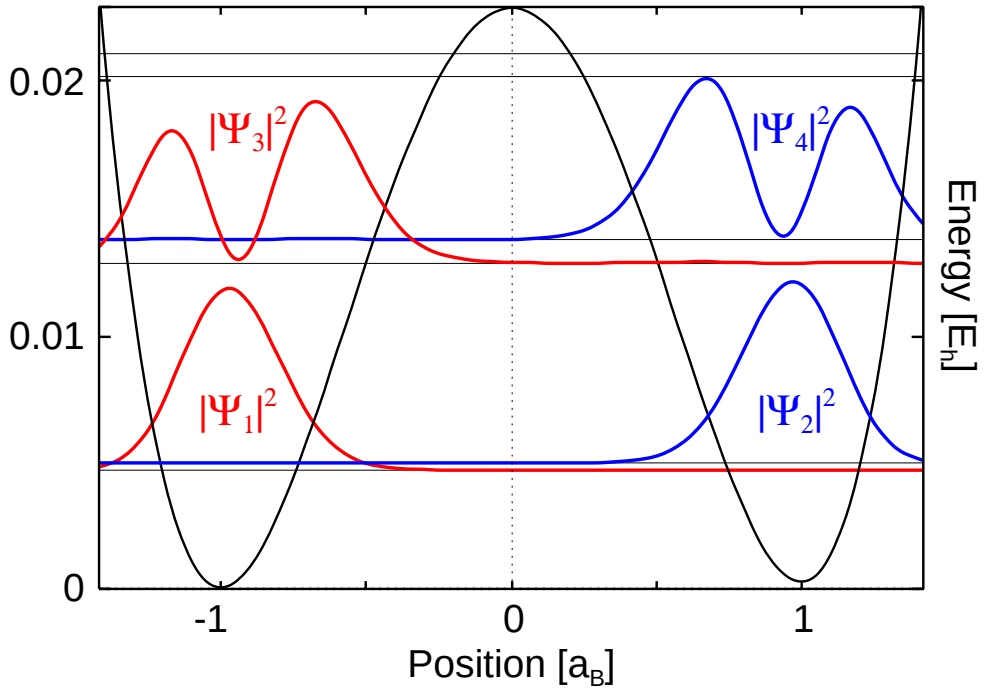

Figure 3.6: Potential, energy levels and the first four eigenfunctions of a system with a barrier 3.5 times as high as the one presented in Fig. 3.2

so that the dump pulse finds no population to dump. The only effect of the pulse is, that some of the excited population decays into the desired state Ψ_2, leading to an accelerated thermalization of the system.

Pump–Tunnel Approach

In order to model situations where the barrier separating reactants from products is higher, which is the case, e.g., for substituted pyrazoles [130], the same potential as given by Eq. (3.1) is used, but with the barrier height scaled by a factor of 3.5. This model potential is used to discuss general aspects of the dynamics without referring to any specific molecule. The potential together with the resulting solutions of the stationary Schrödinger equation are shown in Figure 3.6. Apparently, there are now two localized states on both the reactant and product side. Again, in the following, the molecule is assumed to be prepared in such a way, that the initial proton wavepacket is localized in the lowest eigenstate of the reactant well.

This increase in the potential barrier leads, of course, to a strong reduction in the tunneling probability between the lowest pair of eigenstates. In a scenario like the one discussed in the previous section, the tunneling time between the lowest pair of states brought into resonance by an external plateau field, would be around 130 ps.

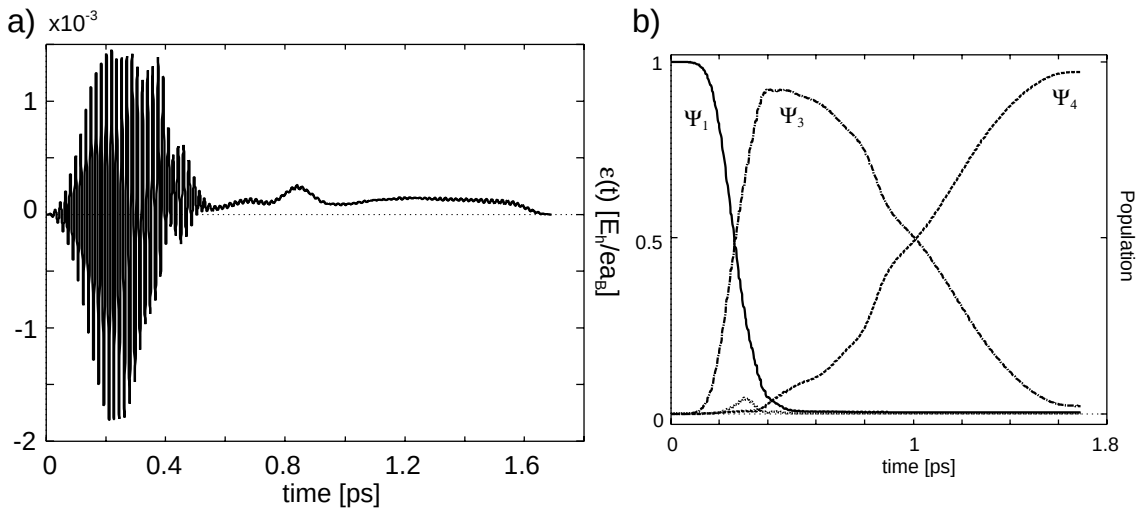

Figure 3.7: Panel **a)** shows the laser pulse obtained from optimal control theory for the isomerization in the system shown in Fig. 3.6, as presented in Ref. [126]. In panel **b)** the population dynamics induced in the high–barrier system is shown. The dotted line shows the population in all states above the first four.

In order to, to find a good reaction pathway, optimal control [66] was employed on the isolated system to find a laser pulse driving the isomerization from the initial state in the left well to the right. This approach resulted in a pulse, which is shown in Figure 3.7. During the first 500 fs the pulse is rather oscillatory with a dominating frequency of $1952\,\mathrm{cm}^{-1}$. In the remaining time interval the pulse changes rather smoothly in a way which reminds on the plateau type tunneling pulse presented in the previous section and in Ref. [126].

Inspecting the population dynamics plotted in Fig. 3.7 one finds that during the oscillatory stage of the pulse the system is excited from the ground state, Ψ_1, to the first vibrationally excited of the reactant well, Ψ_3. Subsequently, the pulse drives the tunneling to the state Ψ_4 localized in the product well. Above barrier states are populated only marginally during the excitation stage.

This behavior leads to the following general reaction path for ultrafast switching of the proton position in high barrier systems: First, a pump–pulse selectively populates a vibrationally excited state localized in the reactant potential well. This excited state should be chosen such, that there is a chance for considerable tunneling coupling to an excited state localized in the product well. This pump–pulse is then be followed by a plateau–type pulse which triggers the tunneling, as described in the previous section for the tunneling between the lowest doublet of states.

This isomerization scheme is examined further in the following, using simplified analytical pulses. For the pump–pulse which induces the population inversion between the states

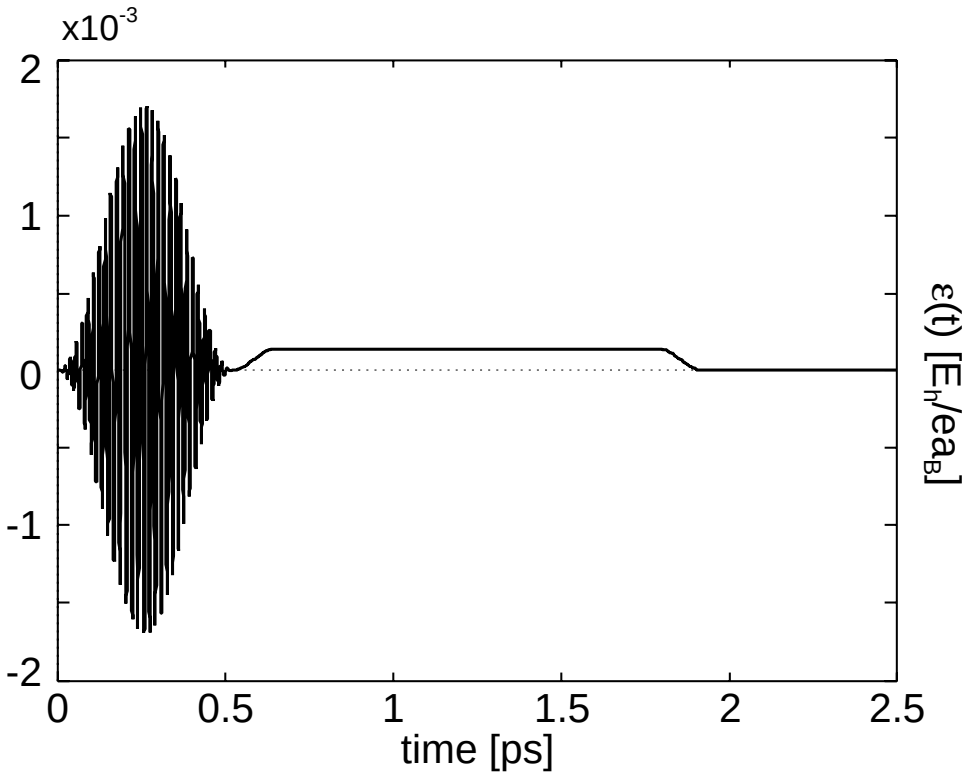

Figure 3.8: The analytical laser pulse used to drive the isomerization in the high barrier model system. It starts with an excitation pulse to populate the second state in the reactant well and only then the tunnel field is switched on. The pulse–parameters are $\mathcal{E}_0 = 1.7 \cdot 10^{-3}\, E_h/ea_0$, $t_0 = 520\,\mathrm{fs}$, $\omega_0/2\pi c = \omega_{13}/2\pi c = 1930\,\mathrm{cm}^{-1}$, $t_p = 1150\,\mathrm{fs}$, $t_{\mathrm{on}} = t_{\mathrm{off}} = 125\,\mathrm{fs}$ and $\mathcal{E}_p = 0.137 \cdot 10^{-3}\, E_h/ea_0$.

Ψ_1 and Ψ_3 a $\sin^2$ shaped pulse was chosen (see, for instance [62, 112]):

$$\mathcal{E}_{\mathrm{ex}}(t) = \mathcal{E}_0 \sin(\omega_0 t) \sin^2(\pi t/t_0) \qquad 0 \le t \le t_0. \tag{3.8}$$

The pulse length, t_0 and its maximum amplitude, $\mathcal{E}_0$, are determined so, that the desired transition is completed at time t_0. The search for the optimum set of parameters has been guided by the optimal control results. Using $t_0 = 520\,\mathrm{fs}$ the other parameters were found as $\mathcal{E}_0 = 1.7 \cdot 10^{-3}\, E_h/ea_0$ if the frequency was kept fixed at the transition frequency $\omega_0/2\pi c = \omega_{13}/2\pi c = 1930\,\mathrm{cm}^{-1}$. If the two processes of excitation and tunneling are kept completely sequential, the plateau pulse driving the tunneling begins at time t_0. Its parameters are chosen such that a transfer between Ψ_3 and Ψ_4 with close to 100% efficiency is achieved. To determine the neccessary plateau field, again the relation Eq. (3.4) can be employed, replacing levels one and two with three and four. The total time for isomerization then is given by $t_0 + t_{\mathrm{on}} + t_{\mathrm{off}} + t_{\mathrm{p}}$. The resulting "hand made"optimal pulse is shown in in Fig. 3.8 and the population dynamics of the four lowest states induced by it can be

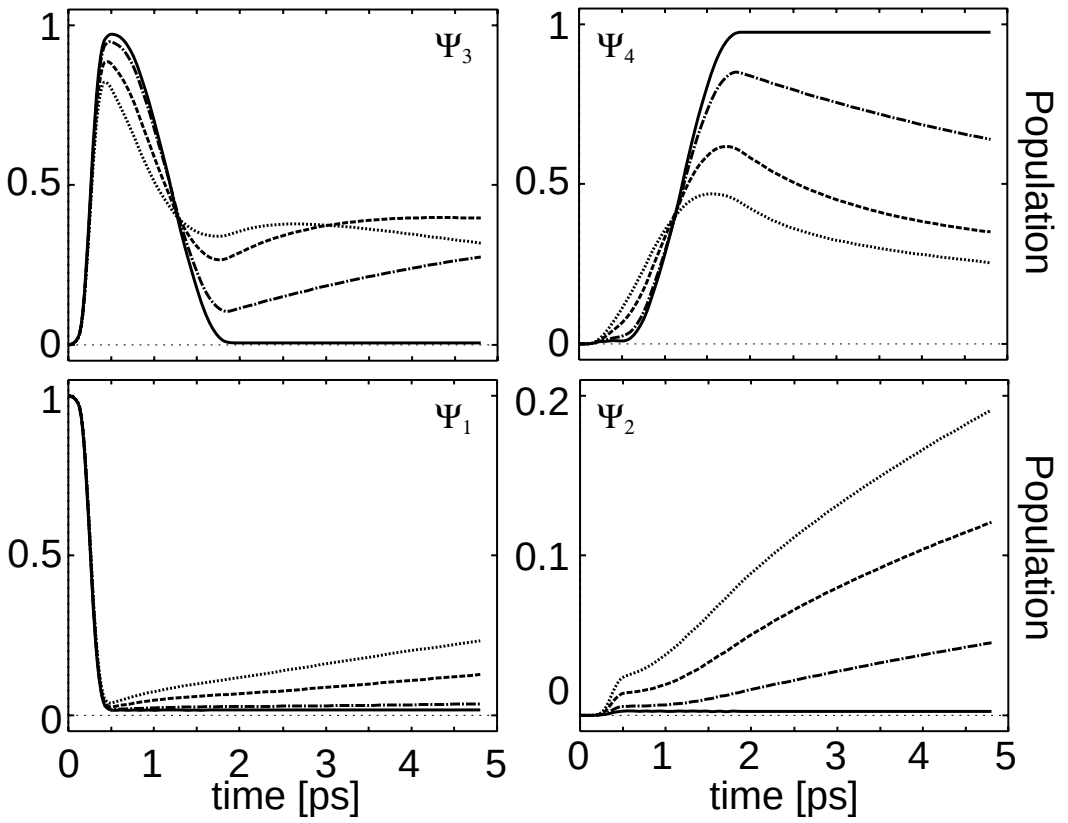

Figure 3.9: The populations of the lowest four levels in the double minimum potential under the influence of the field shown in Fig. 3.8. (Coupling strengths as in Fig. 3.4)

found in Fig. 3.9 (solid lines). In order to characterize the efficiency of control the reaction yield is defined as $|\Psi_2|^2 + |\Psi_4|^2$ with the populations taken at the time when both pulses are over. In the present case the yield is 0.98, a value which in principle could be improved by using refined searching techniques, e.g. employing genetic algorithms, for finding better parameters for the pulse, but as the main aim was to study the general impact of dissipation on this type of reaction, this was not considered necessary.

Switching on the interaction with the environment results in a reduction of this yield as is shown in Fig. 3.14. As a general trend this is, of course, not surprising, as the finite life times of the levels mostly counteract the desired steps on the reaction path for the laser driven isomerization. The population of the excited state from which the tunneling is supposed to start and which is prepared by the pump–pulse decays due to the included dissipation. This is especially evident if the tunneling pulse starts after the excitation pulse has finished. In this case, for fast relaxation ($\alpha = 0.08\lambda$), the population of Ψ_3 is only about 0.8 at the moment the tunnel–pulse starts (cf. Fig. 3.9). It should be noted, however, that this decay partially is going into the desired direction, i.e. Ψ_2 and Ψ_4 are populated

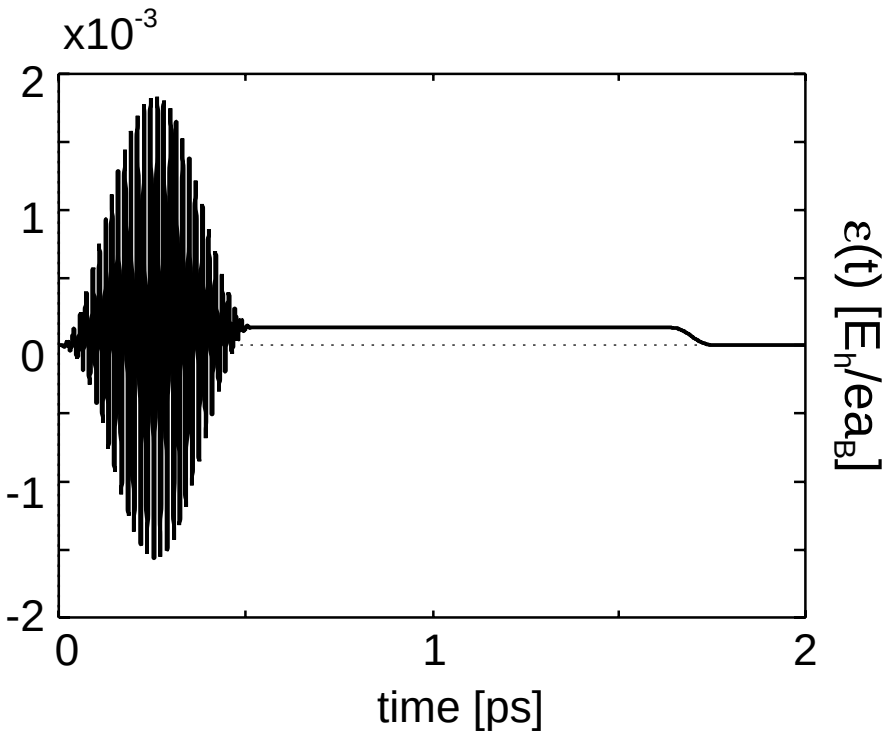

Figure 3.10: Another possibility to choose the laser pulse is to overlap the pulse exciting the system with the one driving the tunneling process, as shown here. (The tunneling starts at $t = 0\,\mathrm{fs}$, together with the excitation pulse.) The pulse–parameters are $\mathcal{E}_0 = 1.7 \cdot 10^{-3}\, E_h/ea_0$, $t_0 = 520\,\mathrm{fs}$, $\omega_0/2\pi c = \omega_{13}/2\pi c = 1930\,\mathrm{cm}^{-1}$, $t_p = 1510\,\mathrm{fs}$, $t_{\mathrm{on}} = t_{\mathrm{off}} = 125\,\mathrm{fs}$ and $\mathcal{E}_p = 0.137 \cdot 10^{-3}\, E_h/ea_0$.

also by the relaxation processes. The population relaxation rates for this model potential are: $k_{41} = \alpha\lambda^{-1}/48\,\mathrm{ps}^{-1}$, $k_{42} = \alpha\lambda^{-1}/702\,\mathrm{fs}^{-1}$, $k_{31} = \alpha\lambda^{-1}/709\,\mathrm{fs}^{-1}$, $k_{32} = \alpha\lambda^{-1}/41\,\mathrm{ps}^{-1}$, and $k_{21} = \alpha\lambda^{-1}/0.75\,\mathrm{ns}^{-1}$. Due to the small k_{21} the non-thermal distribution created by the laser field is maintained for some nanoseconds in this situation, in contrast to the low barrier model, where the system thermalized on the time scale of a few picoseconds.

Clearly, in a dissipative environment, one of the most important properties of an efficient control pulse is its length. In contrast to the situation in an isolated system, the field has to work against the competing effects of energy relaxation, which destroy the coherences between the states. Thus a more efficient control should be possible for shorter control pulses. The optimal field in Fig. 3.7 indicates that it should be possible to use overlapping pulses instead of the sequential scheme without deteriorating the yield for the isolated system. The resulting time–dependence of the field is plotted in Fig. 3.10 (for parameters see figure caption), and the respective population dynamics can be found in Fig. 3.11 for the same set of coupling strengths as in Fig. 3.4. In this case the population transfer pathway $\Psi_1 \rightarrow \Psi_3 \rightarrow \Psi_4$ is open from the very beginning. This possibility results in an

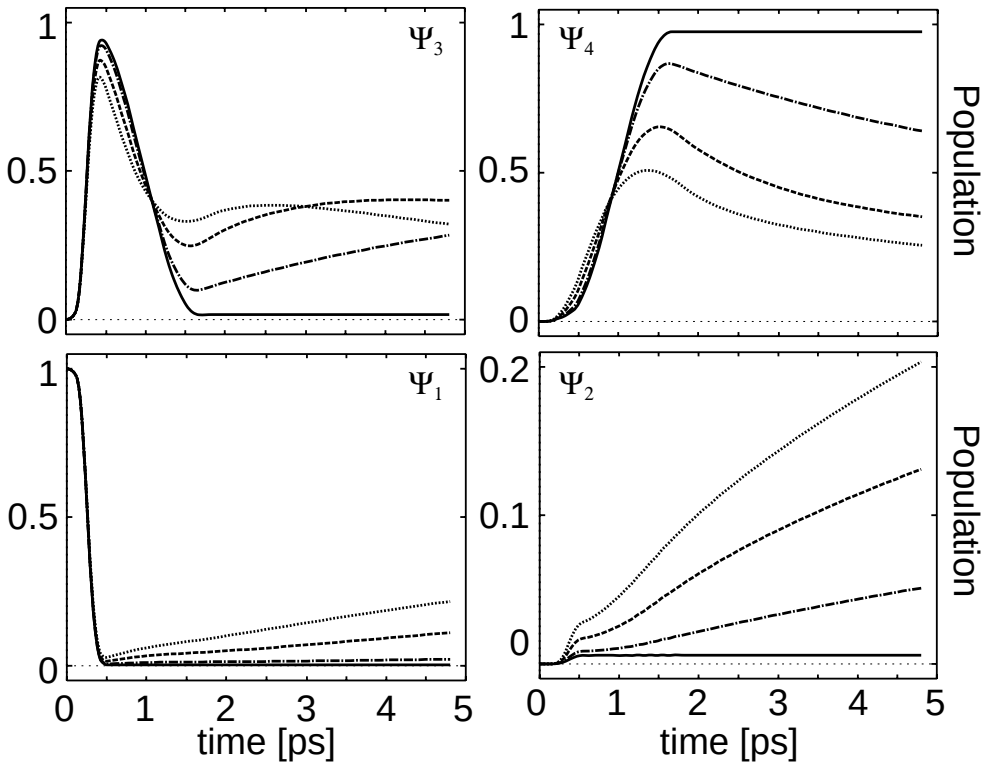

Figure 3.11: The population dynamics of the lowest four levels generated by the pulse shown in Fig. 3.10. (Coupling strengths as in Fig. 3.4)

increased yield as can be seen in Fig. 3.14. Closer inspection of $|\Psi_2|^2$ in Fig. 3.11 shows that there is some gain in population already during the second half of the pump–pulse. In fact the pump–pulse acts as a *dump*–pulse for the level pair Ψ_4/Ψ_2. The efficiency of this process which apparently is very favorable for obtaining high yields depends on the amount of population transferred from Ψ_3 to Ψ_4 during the interval t_0.

This effect is caused by the fact, that the plateau field has to create an almost symmetrical potential to open the tunneling–reaction path, which then of course also generates energetically degenerate pump- and dump–frequencies in the product and reactant wells. To investigate the scale of this effect further, the time t_0 was increased to 1090 fs, i.e. the period where both pulses overlap is extended. For effective population of Ψ_3 the value of $\mathcal{E}_0$ was reduced at the same time to $\mathcal{E}_0 = 0.82 \times 10^{-3}\, E_h/ea_0$. Furthermore, the plateau time for the tunnel–pulse had to be increased to $t_0 = 1780$ fs in order to allow for a transfer of the population which is pumped into Ψ_3 during the second half of the pump–pulse as well. Again these parameters are just a compromise made to accommodate high yield, low intensity, and short pulse duration. The pulse form is shown in Fig. 3.12 and the respective populations are plotted in Fig. 3.13 for the various coupling strengths. As can be seen from the evolution of $|\Psi_2|^2$, this pulse dumps substantial population into the state

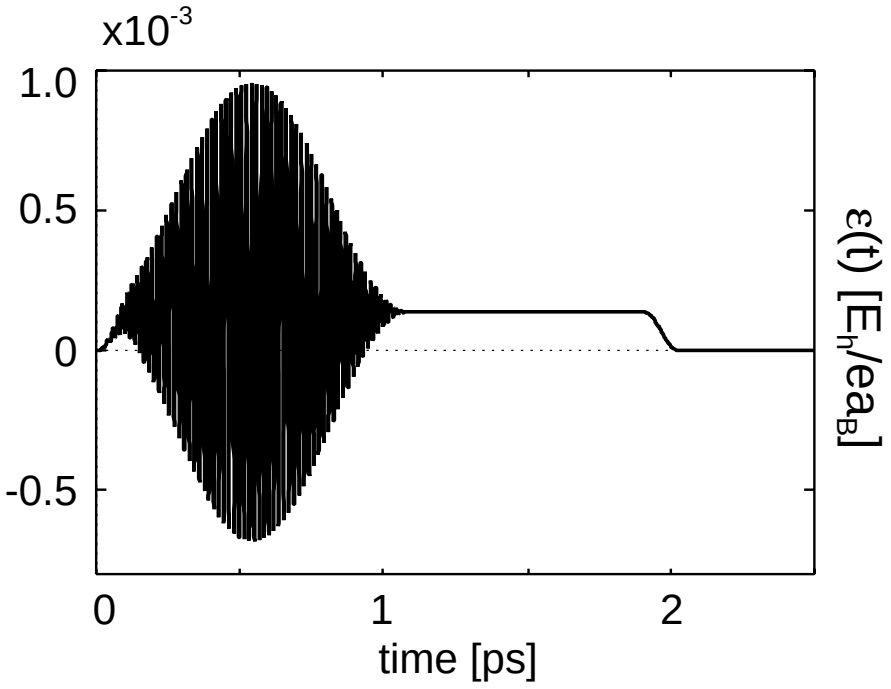

Figure 3.12: Same as in Fig. 3.10, but for longer pump- and tunnel–pulses with lower intensity of the pump pulse. The pulse–parameters are $\mathcal{E}_0 = 0.82 \times 10^{-3}\, E_h/ea_0$, $t_0 = 1090\,\mathrm{fs}$, $\omega_0/2\pi c = \omega_{13}/2\pi c = 1930\,\mathrm{cm}^{-1}$, $t_p = 1780\,\mathrm{fs}$, $t_{\mathrm{on}} = t_{\mathrm{off}} = 125\,\mathrm{fs}$ and $\mathcal{E}_p = 0.137 \times 10^{-3}\, E_h/ea_0$.

Ψ_2 from where it cannot escape in the monitored time interval. This is the main reason for the increased yield as compared with the two cases studied before despite the fact that this setup needs the longest time for isomerization (cf. Fig. 3.14).

Conclusion

These examinations show, that optimal control can find reaction pathways in molecular systems, which previously have not been examined. The proposed pathway drives the isomerization via tunneling through the reaction barrier, thereby avoiding the necessity to populate higher excited states. Additional studies about this type of driven tunneling are presented in some other publications as well [38, 85, 131]. This mechanism works for the low barrier tunnel scheme, already proposed in Ref. [125] for an isolated system, and for the newly proposed pump–tunnel pathway proposed in the framework of this work [127]. The calculations showed that this fact made both reactions more robust against the inclusion of dissipation. Nevertheless, with increasing coupling strength to the environment the chances for realizing the control schemes for both models decrease drastically. Even these relatively simple, one–dimensional models therefore show, that an effective control

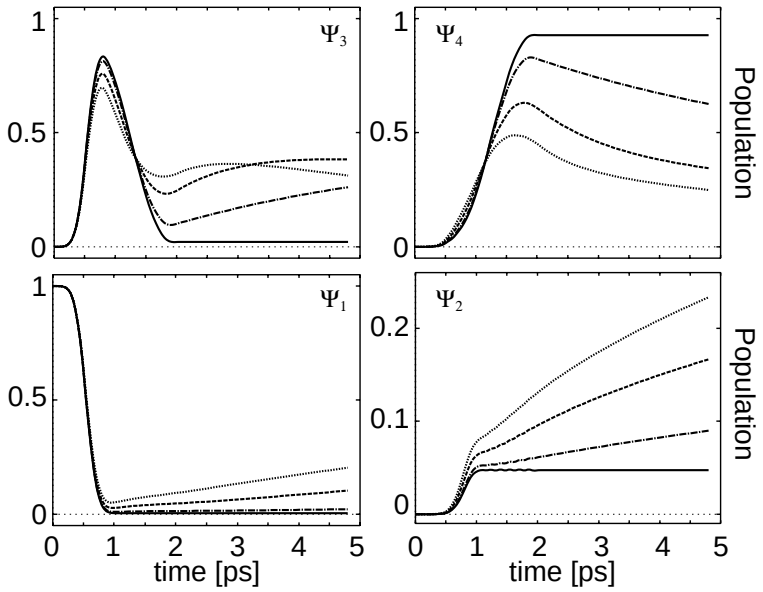

Figure 3.13: The population dynamics of the lowest four levels generated by the pulse shown in Fig. 3.12. (Coupling strengths as in Fig. 3.4)

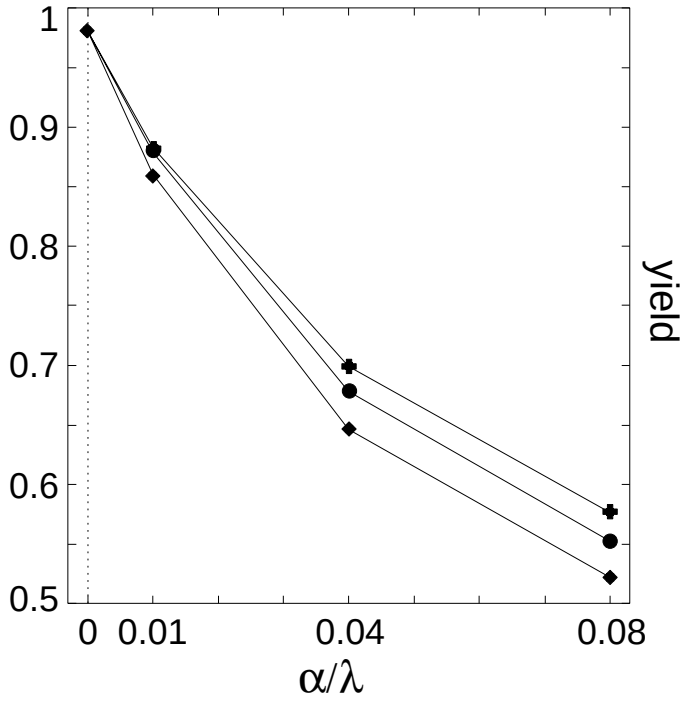

Figure 3.14: The isomerization yield, defined as the combined population of states Ψ_2 and Ψ_4 at the end of the pulses shown: in Fig. 3.8 (squares), in Fig. 3.10 (circles) and in Fig. 3.12 (crosses) for the different dissipation strengths.

of molecular reactions in condensed phase is quite difficult. While the models without any coupling to the environment often allow nearly perfect control of specific quantum states of the system, the picture changes completely in the presence of dissipation. In this case the scenario turns into a "race against time" to manage some sort of control, before the energy of the laser pulse, which should excite some localized bonds, dissipates into the bath and the total system moves into a thermalized, incoherent state. In more realistic molecular models, which include more than one degree of freedom, this problem can already turn up for strongly coupled modes in the form of IVR, even before an additional generic environment is included.

3.1.2 Tests for Control Schemes

After in the last section the control efficiency for a specific reaction path, with and without dissipative effects, was examined, this section deals with the application of various control schemes to different one- and two–dimensional models. The goal here is to see, if there are any algorithms available, which can aid the search for a good reaction path in a specific potential surface, and which are able to generate the electrical field necessary to follow this path.

Local tracking Control

In the following the method of local tracking control presented in Section 2.5.4 is applied to one dimensional model potentials. The first test calculations follow the model described in [117, 118] and test the algorithm on a Morse type oscillator. After this the method is expanded to include error control and a double minimum potential.

Morse Potential

The Morse potential used for the initial calculations was given in the form

$$V(x) = E_D \left[\exp\left\{-2 \cdot \alpha(x - x_0)\right\} - 2 \cdot \exp\left\{-\alpha(x - x_0)\right\}\right] + E_D \tag{3.9}$$

with the dissociation energy $E_D = 0.2101 \cdot E_h$, the minimum position $x_0 = 1.75 a_B$ and the Morse parameter $\alpha = 1.22 a_B^{-1}$. This potential was used in [117] as a model for the HF–molecule. Within this potential the position expectation value was controlled along a path defined by a classical particle obeying of the equation of motion for an anti-damped particle

$$m\ddot{y}_d = -\frac{d\,V(y_d)}{d\,y_d} + \gamma\dot{y}_d \tag{3.10}$$

where $m = 1745.4 m_e$ is the reduced mass in the HF–molecule and the anti-damping is set to $\gamma = 1.0$. The dipole function used for the model has an exponentially damped linear form $\mu(x) = \mu_0 x \exp\{-\zeta x^4\}$, with $\mu_0 = 1.154\,\mathrm{D}$ and $\zeta = 0.0064 a_B^{-4}$ [117].

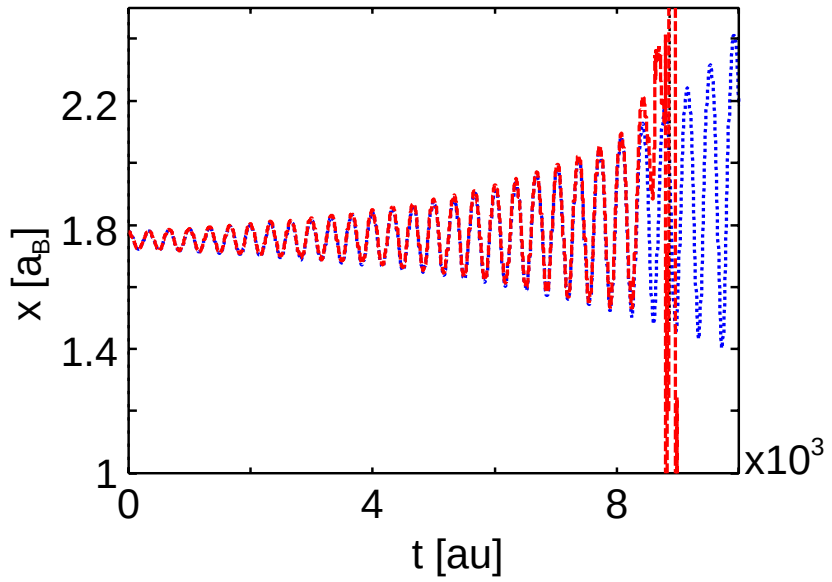

Figure 3.15: The prescribed path (dotted line) and the path actually generated (dashed line) in a Morse–potential with the simple inverse tracking control presented in Section 2.5.4. While the wavepacket remains close to the harmonic part near the minimum it remains localized and the control is nearly perfect. The control breaks down as soon as the wavepacket starts to spread, when it reaches the more anharmonic part of the potential.

Following the algorithm presented in Eq. (2.150), it can be seen, that the position operator commutates with the dipole operator, making it necessary to use the first derivative of the position, i.e. the momentum operator, to calculate the control field. This gives the following equation for the field:

$$\mathcal{E}(t) = \frac{m\ddot{y}_d + \left\langle \frac{d\,V(x)}{d\,x} \right\rangle}{\left\langle \frac{d\,\mu(x)}{d\,x} \right\rangle}. \tag{3.11}$$

The derivative of the dipole and the potential result from the application of the momentum operator $\hat{\mathbf{p}} \equiv \frac{d}{dx}$ in the commutators of Eq. (2.150).

The resulting position tracking and the electrical field used for it are presented in Figs. 3.15 and 3.16. It can be seen that the position tracking is almost perfect for the first $8000\,\hbar/E_h$ (≈ 200 fs) of the calculation. After this time the algorithm suddenly, and rather violently, breaks down. The electrical field calculated from the control equations up to this point was rather large, but otherwise behaved reasonable (i.e. it shows small, regular oscillations). The significant constant part of the field is caused by the fact, that the initial, stationary wavepacket already has a position expectation value, which is slightly offset from the classical minimum of the potential, caused by the anharmonicity of the

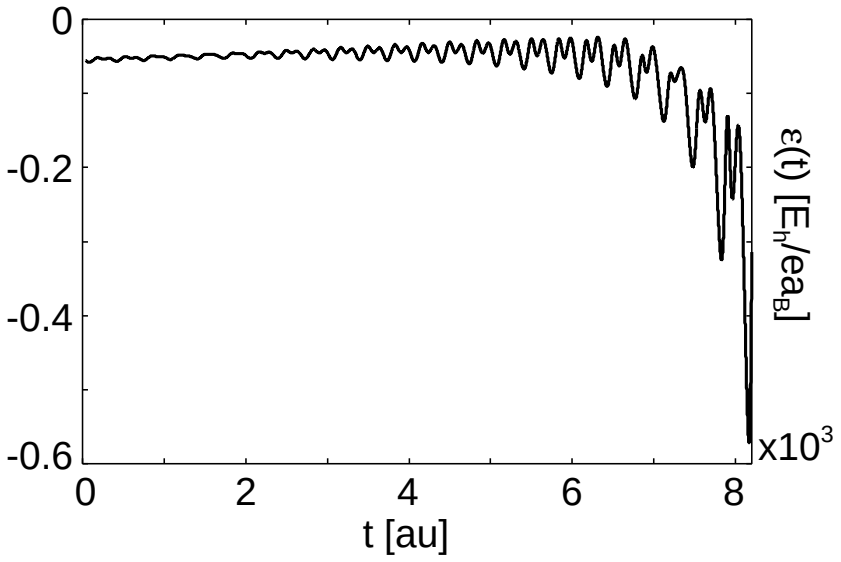

Figure 3.16: The control field for the simple position control presented in Fig. 3.15. The field has a rather strong constant component, and is much to intense for "real life" application.

Morse potential. As the initial values for the classical path and the expectation value to be controlled have to match, the classical trajectory sees a potential gradient, which the electrical field then has to introduce to the system in the form of the constant field. Approaching later times, it starts an exponential growth, which quickly reaches values where not only the numerical solution of the time dependent Schrödinger equation breaks down, but also any real molecule would be ionized immediately. After this, the field displays a more or less irregular behavior, in which the peaks reach values of up to 300 E_h/ea_B (not plotted). This breakdown of control happens, after the wavepacket starts to enter the more anharmonic parts of the Morse potential. This already shows the biggest limitation of the algorithm: It relies on expectation value of a wavepacket to calculate the required electrical field to control this state. If the wavepacket is tightly localized, the quantum system has expectation values, which more more less correspond with the function values taken at the position expectation value (i.e. $\langle f(x)\rangle \approx f(\langle x\rangle)$). This is the central, necessary condition for this algorithm to produce useful results. If the wavepacket enters an anharmonic part of the potential and starts to spread out this condition breaks down, as the different parts of the packet start to sample widely separated parts of the potential.

Another problem of this approach is, that the control equation (2.150) does not allow for any error in the tracking. As soon as there are deviations in the real path of the expectation value from the prescribed value, the algorithm has no way to correct for this. Therefore, the method was expanded by Rabitz *et al.* with the additional terms needed to keep any deviations, introduced by numerical errors or the effect of spreading wavepackets,

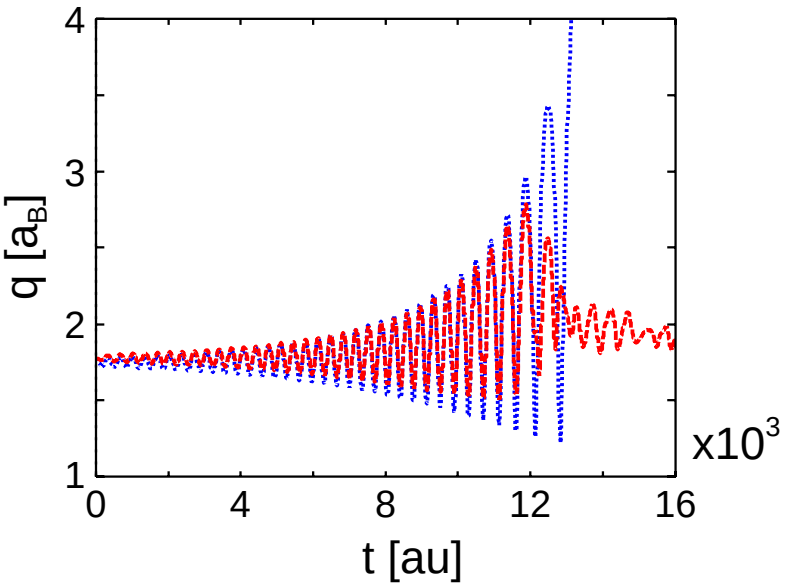

Figure 3.17: The prescribed path (dotted line) and the path actually generated (dashed line) in a Morse–potential for which the position and the error of the wavefunction were controlled at the same time. This method does not produce a perfect tracking, but manages to keep the wavepacket under control for a longer time than the simple approach of Fig. 3.15. Here the algorithm breaks down shortly before the dissociation limit is reached.

under control (Eq. (2.151))[118].

While the equations and parameters for the classical path and the potential remain the same, the control field is now calculated from

$$\mathcal{E}(t) = \frac{1}{\left\langle \frac{d\,\mu(x)}{d\,x} \right\rangle} \left[m\ddot{y}_d + \left\langle \frac{d\,V(x)}{d\,x} \right\rangle + \rho_1 (m\dot{y}_d - \langle \hat{\mathbf{p}} \rangle) + \rho_0 (y_d - \langle \hat{\mathbf{x}} \rangle) \right], \tag{3.12}$$

which includes terms damping the error in the generated path with the factor ρ_0 (for the original path) and ρ_1 (for the resulting momentum path).

The position tracking calculated with this approach and the electrical field used for it are presented in Figs. 3.17 and 3.18. This algorithm produces only an approximate tracking, but manages to keep the wavepacket under control for a significantly longer time. The effect of the error control at the beginning of the pulse is the loss of the perfect tracking achieved with the simpler method presented before. This is compensated by the fact that the control remains possible for a much longer time. As can be seen in Fig. 3.17, the position expectation value closely follows the classical path nearly to the dissociation limit. Shortly before this is reached, the wavepacket finally becomes so spread out, that even the error damping term in the control field cannot maintain the control any longer.

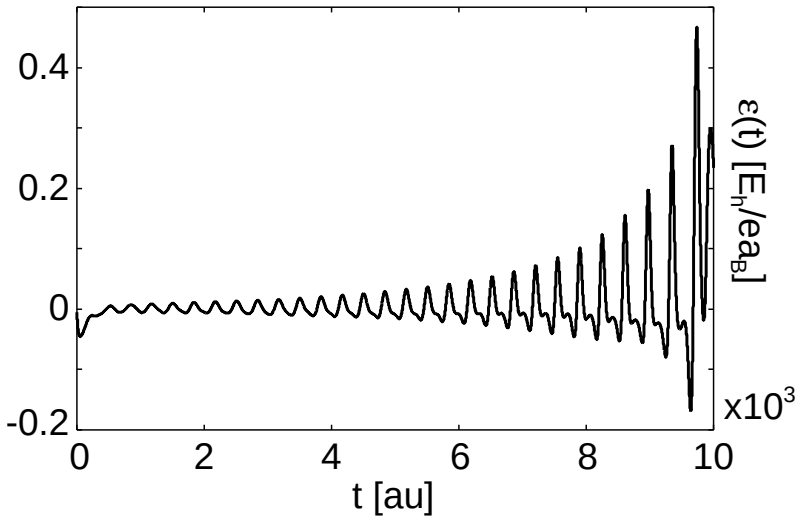

Figure 3.18: The control field for the position control with additional error control presented in Fig. 3.17. This field no longer has the strong constant component, which was found in Fig. 3.16, therefore in the beginning it is significantly weaker, but its intensity, especially at later times, is still much too high for useful applications.

The electrical field again exhibits irregular behavior after the control breaks down, but with a strongly reduced amplitude, when compared to the exact tracking. The maximum values reached are on the order of $3\,E_h/ea_B$.

The effect of the different algorithms on the shape of the wavepacket is shown in Fig. 3.19. There the shape of the wavefunction in position space is plotted for $t = 0\,\hbar/E_h$ (black), for $t = 8000\,\hbar/E_h$ (red), the time where the exact tracking algorithm looses control of the system, and for $t = 12000\,\hbar/E_h$ (blue, only for the method with error control). One can easily see, that the exact tracking method produces a quite spread out distribution with several sub-peaks, where the expectation value of $\hat{\mathbf{x}}$ does no longer coincide with the location of the maximum probability density in the wavepacket. In contrast to that, after the same control time the approximate tracking manages to keep the system in a relatively localized state, which allows the algorithm to continue with the control for a further $4000\,\hbar/E_h$, until the classical path nearly reaches the dissociation limit. In this anharmonic region the wavepacket finally becomes delocalized as well (depicted in the lower panel as the blue curve), leading to the breakdown of the control scheme.

Double Minimum (DM) Potential

After the test with the Morse potential, the inverse tracking method is applied to a DM potential. For this the model potential used for the driven tunneling in the last section (Eq. (3.1)), together with a linear dipole moment ($\mu(x) = \mu_0 x$, $\mu_0 = 0.75e$) is chosen. The barrier is set at the higher value, as used for the pump–tunnel model, resulting in a

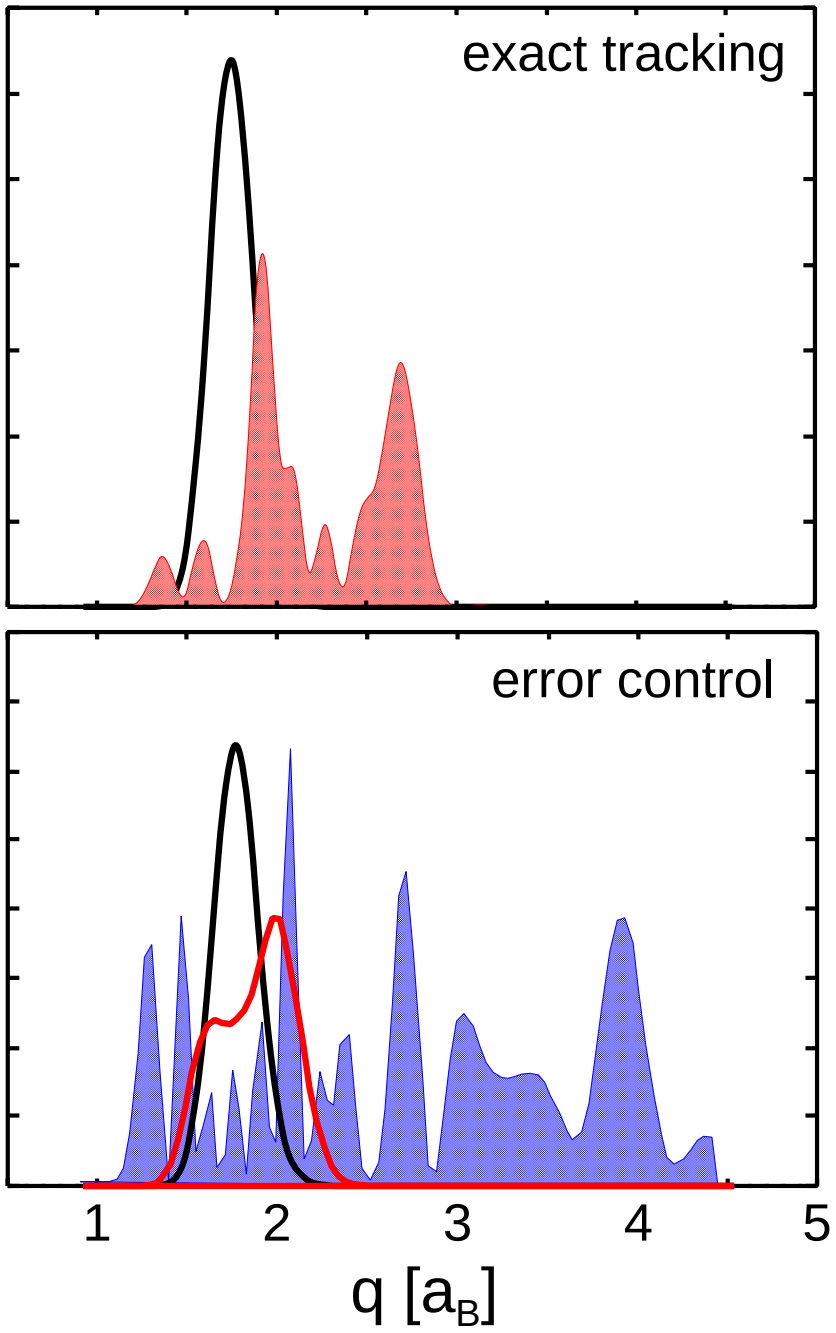

Figure 3.19: The wavepackets generated by the simple exact tracking method and the approach including error control (black: initial condition, red: $t = 8000\,\hbar/E_h$, blue: $t = 12000\,\hbar/E_h$) in the Morse potential. It can be clearly seen that the second method manages to keep the wavepacket better localized, leading to the longer possible control time.

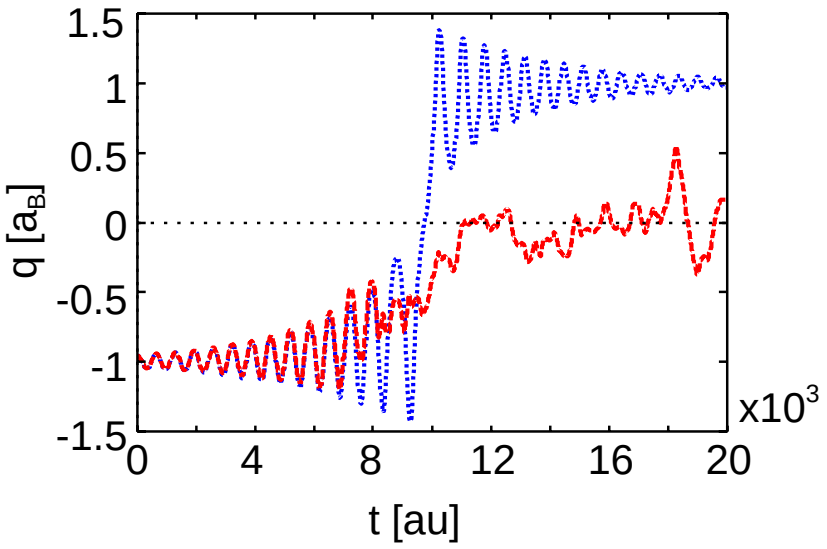

Figure 3.20: Exact tracking in a double minimum potential. Again the tracking is perfect while the WP stays near the harmonic minimum on one side of the potential. As soon as it starts to spread out while trying to move across the barrier, the control breaks down.

potential as shown in Fig. 3.6. The classical path for the control of the position expectation value is calculated from an anti-damped oscillator (Eq. (3.10)) in the starting well, and switched to a damped one ($\gamma = -1$) as soon as the trajectory passes over the barrier into the target well. The first calculations are again performed with the exact tracking control field given by Eq. (3.11).

The resulting position tracking and the electrical field used for it are presented in Figs. 3.20 and 3.21. As within the Morse potential, the control is perfect for the first part of the calculations, while the wavepacket stays near the nearly harmonic minimum of the product well. As soon as the system reaches the anharmonic part near the barrier, the control breaks down and only produces irregular fluctuations within a spread out wavepacket. This means that, while the excitation of the localized initial state to an energy above the barrier is no problem, the algorithm is not able to dump the resulting wavepacket into the reactant well. The electrical field resulting from the control equations again has a constant component, resulting from the slight anharmonicity already seen by the ground state wavefunction. The tracking is successful, and the field reasonable for approximately the first $7000\,\hbar/E_h$ of the dynamics. Then strong deviations from the prescribed track start to appear, and the field exhibits the spike like behavior already seen for the Morse potential. The main difference is, that the intensity remains below $0.5\,E_h/ea_B$ during the process.

To improve this result, the DM system was then treated with the tracking algorithm

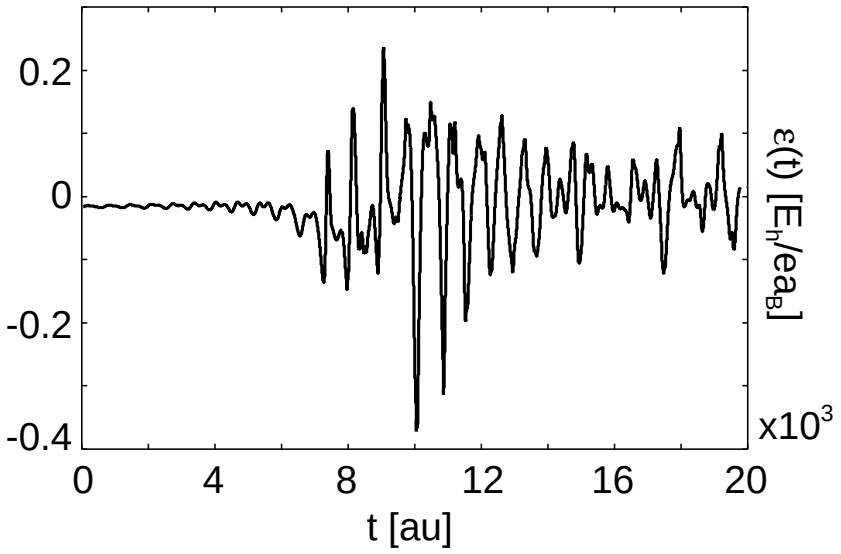

Figure 3.21: The control field for the simple position control in a double minimum potential, as presented in Fig. 3.20.

including the error control terms (Eq. (3.12)). All the other parameters are retained from the previous exact tracking method.

The results of these calculations are presented in Figs. 3.22 and 3.23. This time, the error control only leads to slightly improved controllability of the system. The classical path in the reactant well is tracked nearly perfectly for one more oscillation than for the exact method, but afterwards the deviations from the prescribed track are also significant. It looks, as if control is regained for a period, when the classical path crosses the barrier, but after this short interval the expectation value settles into a random fluctuation around zero, similar to the one calculated from the method without error control. The electric fields generated differ in the respect, that the algorithm including error control does not generate the constant component of the field found in the previous calculation, and in the slightly smaller maximum amplitude of field spikes generated, when the control breaks down. For this calculation the maximum amplitude does not rise above $0.3E_h/ea_B$.

Looking at the development of the wavepacket for the two methods in Fig. 3.24, this time no significant gains in localization for one of the two algorithms can be found, as the control breaks down at approximately the same time. The main difference is, that the exact tracking produces a wavepacket still mostly localized in the reactant well at the time the classical path crosses over to the product side (red curve). At the same time, the error control method already managed to transfer half of the population over the barrier, resulting in an evenly distributed wavepacket. This can be also seen from the track of the position expectation value, which is still on the product side for the exact tracking, and close to zero for the error control method. At later times (blue curve) both

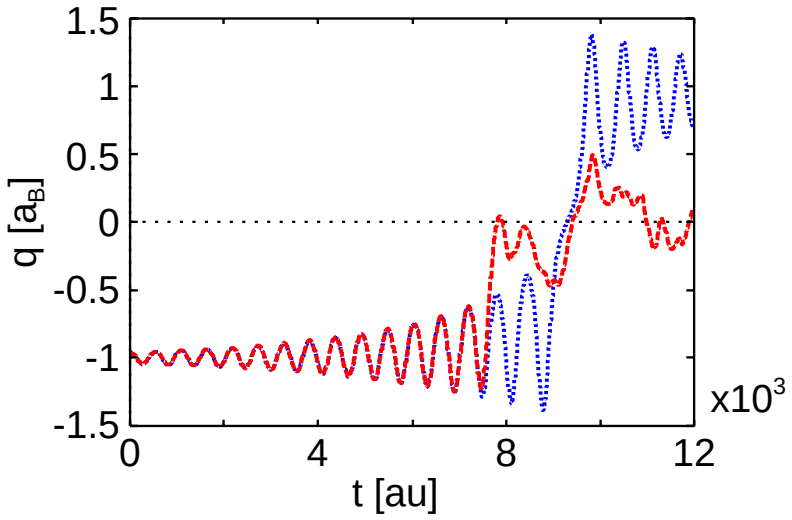

Figure 3.22: The system from Fig. 3.20 with error control. This only leads to a small improvement in the ability to track the position of the WP. The control again fails to drive the system completely over the barrier.

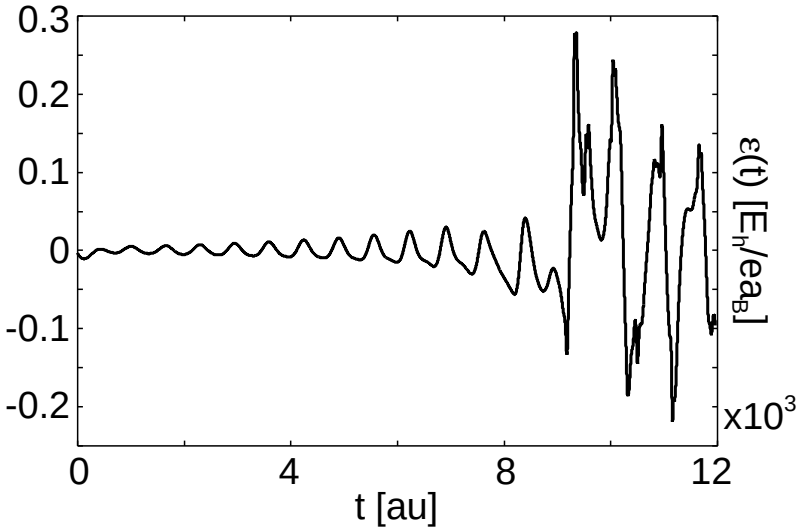

Figure 3.23: The control field for the position control with additional error control presented in Fig. 3.22.

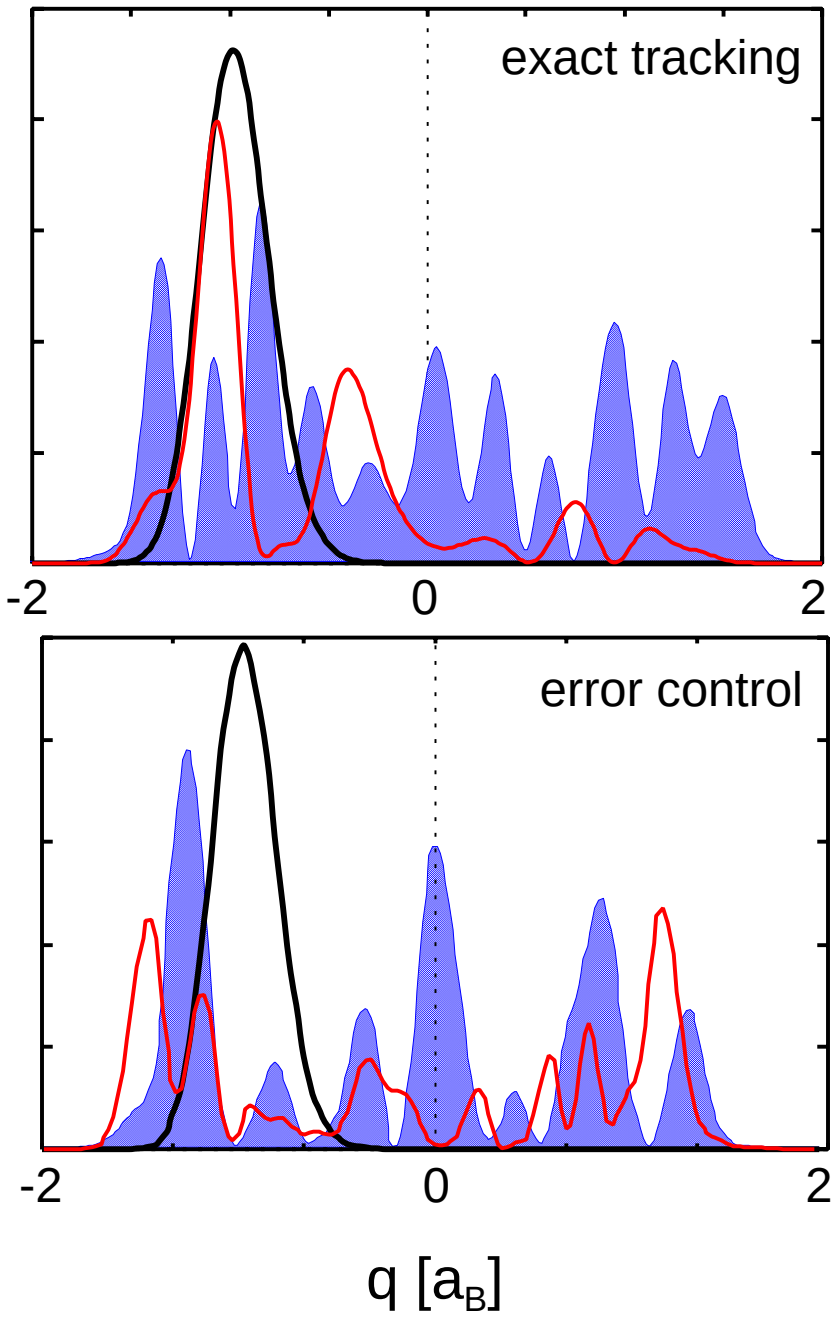

Figure 3.24: The form of the wavepackets for the two tracking methods (black: initial time, red: time at which the classical path crosses zero, blue: $t = 16000\,\hbar/E_h$) in the DM potential. The simple tracking produces a spread WP still mostly in the product well. The method including error control results in a WP distributed more more less evenly between the two wells.

algorithms have distributed the wavefunction over the whole accessible potential, resulting in an expectation value for the position oscillating around zero and an complete inability to apply the inverse tracking algorithm to the delocalized system.

These results show, that the inverse tracking control of a simple variable like the position, is not able to drive quantum system over a barrier or into an anharmonic region of a potential. As soon as the initially localized wavefunction starts to spread out due to anharmonicity, or even splits at a barrier, the algorithm breaks down and cannot regain control. The field is generated by the control equations always under the assumption, that the main part of the wavepacket is localized at the calculated expectation value of the system. If this is no longer true, the field only affects the part of the wavefunction, which really is located there, in the desired manner and has unpredictable results on all parts located at different points of the potential.

Variance Control

To get around the limitations of the position control presented above, the tracking control algorithm was used to control not only the position expectation value, but also the variance, defined by $\langle(\hat{\mathbf{x}} - \langle\hat{\mathbf{x}}\rangle)^2\rangle = \langle\hat{\mathbf{x}}^2\rangle - \langle\hat{\mathbf{x}}\rangle^2$, of the wavepacket. The reasoning behind this is, that if the algorithm is successful in controlling the variance, it can be set up to maintain a constant value for this during the control period. If this is possible, the resulting wavepacket should then be tightly localized and allow the application of the position tracking method even after entering an anharmonic part of the potential.

Obviously, this approach requires the simultaneous control of two different variables, the position and the square position, as from these two the variance can be calculated. This makes it necessary to employ the algorithm using a cost functional (Eq. (2.153)), resulting in the simultaneous, competitive tracking of all the desired variables. This cost functional is build from the sum of the tracking errors of the position expectation value $\langle\hat{\mathbf{x}}\rangle$ and its square $\langle\hat{\mathbf{x}}^2\rangle$. The resulting cost functional developed for this work has the form

$$\mathcal{I} = W_{\mathrm{x}}\left[\sum_{i=0}^{2}\rho_i^{\mathrm{x}}\left(\frac{d^i y_g^{\mathrm{x}}}{dt^i} - \left\langle\hat{\mathbf{O}}_i^{\mathrm{x}}\right\rangle\right)\right]^2 + W_{\mathrm{x}^2}\left[\sum_{i=0}^{2}\rho_i^{\mathrm{x}^2}\left(\frac{d^i y_g^{\mathrm{x}^2}}{dt^i} - \left\langle\hat{\mathbf{O}}_i^{\mathrm{x}^2}\right\rangle\right)\right]^2 + W_{\mathcal{E}}\mathcal{E}^2, \qquad (3.13)$$

where $\left\langle\hat{\mathbf{O}}_0^{\mathrm{x}}\right\rangle = \langle\hat{\mathbf{x}}\rangle$ is the position expectation value and $\left\langle\hat{\mathbf{O}}_0^{\mathrm{x}^2}\right\rangle = \langle\hat{\mathbf{x}}^2\rangle$ is the expectation value of the squared position operator. The $\hat{\mathbf{O}}_i$ with higher indices are the higher order operators, as calculated from Eq. (2.149) and the y_g^{x} and $y_g^{\mathrm{x}^2}$ are the prescribed classical trajectories for the position and its square. The two terms for these properties are supplemented by the third term, which penalizes a high amplitude of the electrical field. All terms are weighted relative to their importance in the control with a set of arbitrary coefficients W_i. To generate the optimal tracking field, the derivative of this functional with respect to $\mathcal{E}$ has to be calculated, set to zero and solved for $\mathcal{E}$.

Performing the derivation and calculating all the commutators for the higher order operators results in

$$\begin{aligned}\mathcal{E}(t) = & \\ & \left\{ W_{\mathrm{x}} \left\langle \frac{d\,\mu}{d\,x} \right\rangle^2 - W_{\mathrm{x}^2} \left\langle \hat{\mathbf{x}} \frac{d\,\mu}{d\,x} \right\rangle^2 + W_{\mathcal{E}} \right\}^{-1} \times \\ & \left\{ W_{\mathrm{x}} \left\langle \frac{d\,\mu}{d\,x} \right\rangle \left[\left(m\ddot{y}_d^{\mathrm{x}} + \left\langle \frac{d\,V}{d\,x} \right\rangle \right) + \rho_1^{\mathrm{x}} \left(m\dot{y}_d^{\mathrm{x}} - \langle \hat{\mathbf{p}} \rangle \right) + \rho_0^{\mathrm{x}} \left(y_d^{\mathrm{x}} - \langle \hat{\mathbf{x}} \rangle \right) \right] + \right. \\ & \quad W_{\mathrm{x}^2} \left\langle \hat{\mathbf{x}} \frac{d\,\mu}{d\,x} \right\rangle \left[\left(-\frac{1}{2} m\ddot{y}_d^{\mathrm{x}^2} - \frac{1}{m} \left\langle \hat{\mathbf{p}}^2 \right\rangle + \left\langle \hat{\mathbf{x}} \frac{d\,V}{d\,x} \right\rangle \right) + \right. \\ & \qquad \left. \left. \rho_1^{\mathrm{x}^2} \left(\dot{y}_d^{\mathrm{x}^2} + \frac{1}{m} \left[\langle \hat{\mathbf{x}}\hat{\mathbf{p}} \rangle + \langle \hat{\mathbf{p}}\hat{\mathbf{x}} \rangle \right] \right) + \rho_0^{\mathrm{x}^2} \left(y_d^{\mathrm{x}^2} - \left\langle \hat{\mathbf{x}}^2 \right\rangle \right) \right] \right\}. \end{aligned} \tag{3.14}$$

This formula reduces to the already known equation for the position control with error damping (Eq. (3.12)), if the weights W_{x^2} and $W_{\mathcal{E}}$ are set to zero. It can also be seen, that the weighting of the term for the electrical field only results in a reduction of the total amplitude, as this factor only occurs in the denominator of the expression. The addition of this term also prevents the occurrence of singular points in the calculated field, which would occur if the expectation values in the other terms are zero.

This expression is then used to calculate $\mathcal{E}(t)$ in the same DM potential used in the last section. The classical path for the squared position operator is set so, that the resulting variance $\langle \hat{\mathbf{x}}^2 \rangle - \langle \hat{\mathbf{x}} \rangle^2$ stays constant at its initial value. The relative weights W_{x^2} and W_{x} in the control equation can be set arbitrarily.

The position tracking and the electrical field generated by the algorithm for an equal weighting of the two classical control pathways ($W_{\mathrm{x}^2} = W_{\mathrm{x}} = 0.5$) and a small penalty for a high electric field ($W_{\mathcal{E}} = 0.5$) are presented in Figs. 3.25 and 3.26. Choosing different weighting factors (i.e. weighting either the position or the variance tracking stronger) destroys all the effects differing from the pure position control reported in the following.

Surprisingly, the field generated is nearly identical to the one resulting from the calculations for the position expectation value only, as presented in Fig. 3.23. This small difference, generated by the additional control of $\langle \hat{\mathbf{x}}^2 \rangle$, results in a significant difference in the generated position tracking. Both the simple exact tracking and the algorithm including error control result in a control path, which is nearly identical to the prescribed track in the reactant well, they loose control when the wavepacket approaches the barrier and finally result in a completely spread out system, whose position expectation value oscillates around zero. In the first part, the competitive tracking of the two expectation values appears to be worse: While the control of the system is again lost at approximately the same point of the prescribed path, the resulting track on the reactant side of the DM potential is not reproducing the classical path exactly. This is caused by the fact, that one electrical field cannot be used to track two different variables simultaneously and exactly. The minimizing of the error functional only results in a compromise field, which minimizes

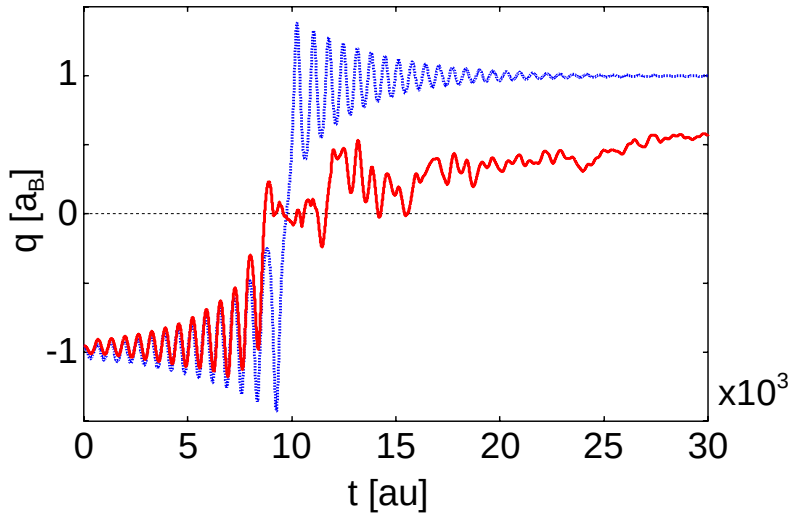

Figure 3.25: The prescribed path (dotted line) and the path actually generated (dashed line) in a DM potential, employing a simultaneous control of the position and the variance of the wavefunction. As the control of the variance keeps the system more compact when crossing the barrier, the algorithm manages to produce a wavepacket, which is clearly localized more on the product side of the potential.

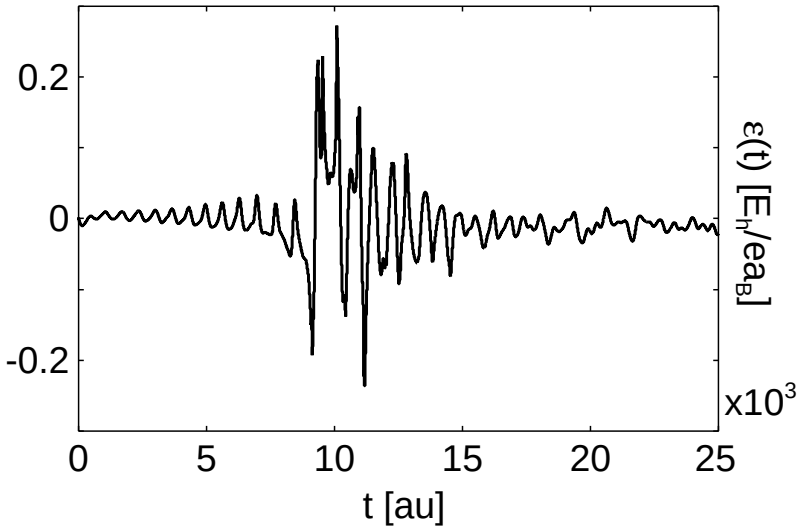

Figure 3.26: The control field for the position control with additional error control presented in Fig. 3.25.

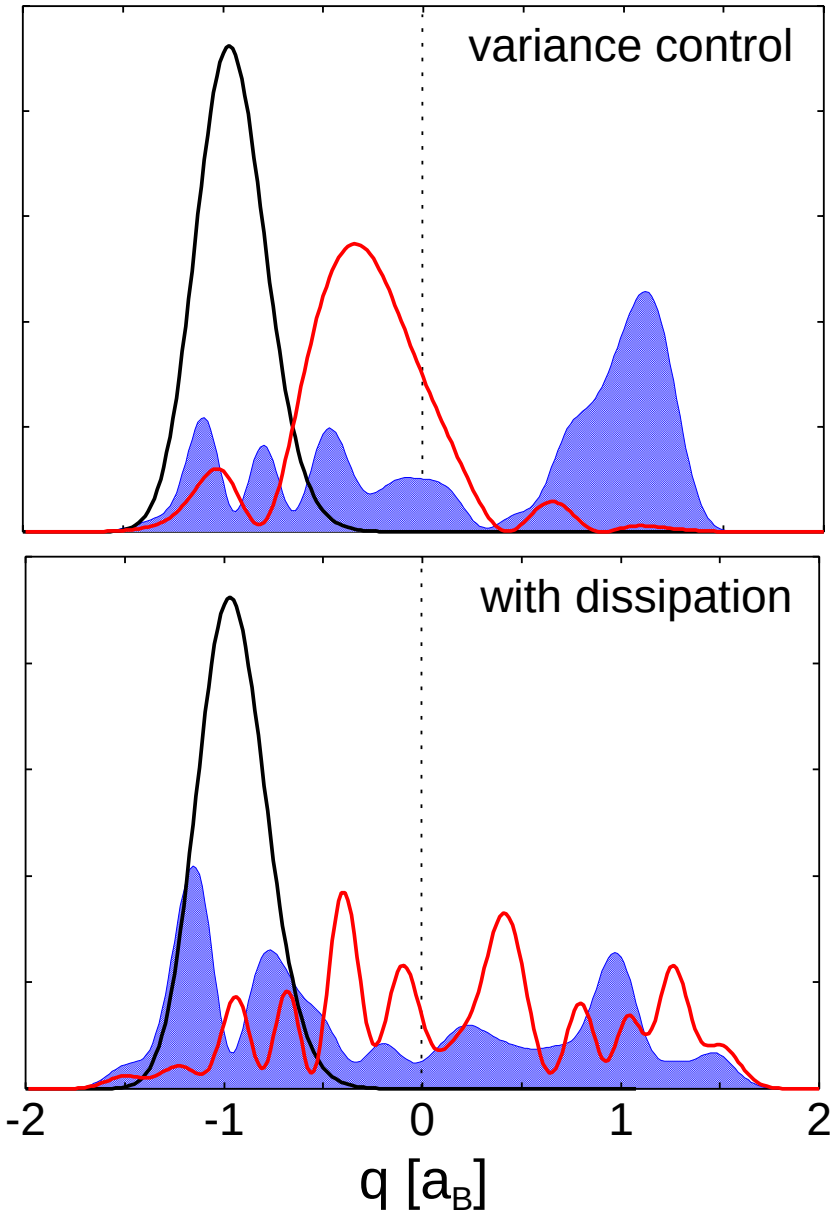

Figure 3.27: The wavepackets generated by the simultaneous control of position and variance, in the upper panel without and in the lower with dissipation. (black: initial condition, red: $t = 10000\,\hbar/E_h$, blue: $t = 20000\,\hbar/E_h$).

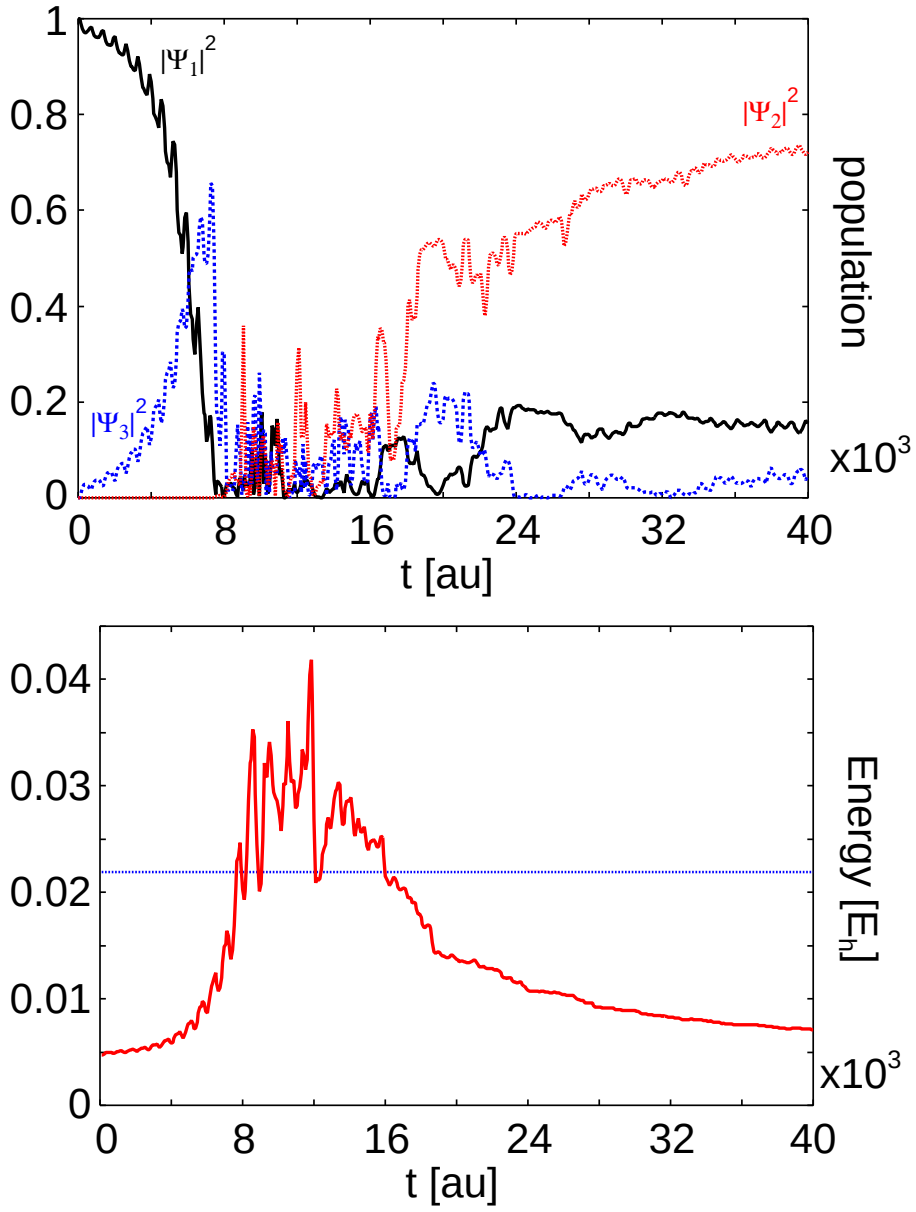

Figure 3.28: The level populations of the lowest three eigenstates and the total energy of the propagation with variance control, as presented in Fig. 3.25. The horizontal line in the lower panel indicates the height of the barrier.

the weighted error for each track at each point of the path. The important gain this implementation of the algorithm managed to make can be seen for longer times: The position expectation value also settles down to a oscillatory behavior, which this time is not moving around zero, but is located significantly on the target side of the DM potential. Looking at the distribution of the wavepacket for the different times, presented in the upper panel of Fig. 3.27, one can see clearly, that this form of the algorithm manages to drive the system over the potential barrier while still retaining a relatively localized shape. At the time the classical path crosses the barrier, only a small part of the wavepacket has split off from the main peak. Further propagation then causes the wavefunction to split, the main part moving into the target well and a small rest dropping back to the reactant side. So even though the generated position expectation value is far from the desired target value, the algorithm manages to control the system in the sense, that the population of the reactant state is larger than the one of the inital one after the end of the control time is reached. In Fig. 3.28 this population dynamics of the lowest three eigenstates, and the total energy of the system is plotted. This shows, that the algorithm really manages to guide the wavepacket into a stable state, which is located mostly on the product side, and not to some high energy, above barrier wavepacket, which is only there for a short time before oscillating back. The population dynamics in the upper panel shows, that in the beginning of the control, while the prescribed path is still closely followed, the oscillations of the wavepacket are generated by a superposition of the first and third eigenstate. Then, at approximately $t = 8000\,\hbar/E_h$, the oscillations of the classical path get too large, to be represented by only these two eigenfunctions, and move into the more anharmonic region of the barrier. At this time the control starts to deviate from the prescribed path and the electrical field resulting from the control algorithm exhibits the strong spiking behavior. These field spikes manage to depopulate Φ_1 and Φ_3 almost completely, and transfer most of the population to higher excited states. This behavior of the field slowly stops at around $t = 15000\,\hbar/E_h$ and the excited population is dumped mostly into Φ_2, located in the target well. The total energy of the system, plotted in the lower panel of Fig. 3.28, shows, that the laser pulse increases the energy of the wavepacket significantly above the barrier, and then manages to dump the system back to a total energy far below it. This means, that in the absence of dissipation, the system stays localized in the target well indefinitely.

This control is possible with just using the potential, the dipole moment and some classical trajectories generated within this potential. No further assumptions are made for the electrical field, which finally acts on the quantum system. The drawback of the approach is, that the calculated field exhibits spikes of unreasonable high amplitude when the control starts to break down. Applying these field strengths to a real molecule would lead to the immediate ionization of the system. An additional problem is, that the results depend significantly on the choice of the weighting factors W_{x^2} and W_{x} and on the error control terms ρ_i. While some combination of parameters results in the presented results, even slight changes can lead to completely different results for the wavepacket dynamics.

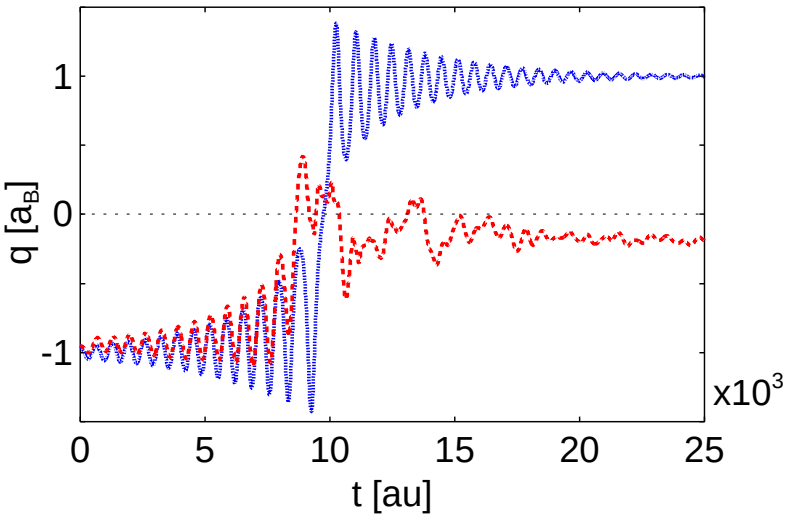

Figure 3.29: The same system as the one presented in Fig. 3.25. Here the dissipation destroys the slight localization generated by the control algorithm, as the population decays back into the lower lying product well.

potential form	Morse	double minimum	
control type	error control	error control	error + variance control
W_{x}	1.0	1.0	0.5
W_{x^2}	0.0	0.0	0.5
$W_{\mathcal{E}}$	0.0	0.0	0.5
ρ_1^{x}	0.5	0.5	0.5
ρ_0^{x}	0.1	0.1	0.1
$\rho_1^{\mathrm{x}^2}$	–	–	0.5
$\rho_0^{\mathrm{x}^2}$	–	–	0.1

Table 3.1: The various damping and weighting coefficients used in the inverse tracking control calculations.

In a final calculation for the inverse tracking algorithm, it was tested, if the method is stable versus the introduction of dissipation to the system. For this, the Redfield approach to the dissipation already used for the driven tunneling in Section 3.1.1 is included into the calculations. In contrast to the approaches presented in [6, 117, 118, 119], for this a density matrix has to used to describe the system. Therefore it is necessary to replace the expectation value with a thermal average (i.e. going from $\langle x \rangle$ to $\mathrm{tr}(\hat{\rho})$).

As the generic coupling strength to the environment the weak coupling ($\alpha = 0.01\lambda$; cf. Fig. 3.4) is chosen. The position trace for a calculation using the same parameters as the one shown in Fig. 3.25 is presented in Fig. 3.29. It can be seen, that even the weak

dissipation introduced destroys the efficiency of the control algorithm completely. The coupling to the bath causes the system to relax back to the energetically lower reactant well, resulting in a final localization of the position expectation value slightly on the reactant side. This effect is caused by the fact, that the high intensity field, generated at the time the algorithm tries to move the wavepacket over the barrier, populates high–energy states above the barrier. This can be seen in the level population plotted in Fig. 3.28, where in the time interval between $8000\,\hbar/E_h$ and $16000\,\hbar/E_h$ most of the population is in levels above the third. These have a relatively short lifetime, resulting in a fast dissipation back into the ground state. As the initial wavefunction was located on the reactant side, the exited states populated are those with a high dipole coupling to the initial state on the reactant side. The decay therefore results mainly in a repopulation of the initial state, while only a small fraction decays to the product side.

Conclusion

The applications of the local tracking control showed, that the algorithm is able to keep a localized wavepacket under excellent control. Unfortunately, this control needs unrealistically high field–strength, which in real life experiments would cause the immediate ionization of the molecule. Additionally, the method is not very stable for spread out wavepackets, which deviate from the prescribed classical trajectory. The simplest approach used, the exact tracking method, breaks down immediately, if the expectation value generated from the calculated field deviates from the prescribed track. This effect can be slightly reduced by introducing an error control mechanism into the control equations (Eq. (3.12)). This enables a slightly longer control time, but the algorithm still fails, as soon as the wavepacket starts to enter an anharmonic part of the potential and spreads out. As noted above, this limitation of the algorithm results from its reliance on the expectation value to calculate an electric field, which is then applied to the total wavepacket, and not only to the part of it, which is close to this expectation value. In a further step, it was tried to delay the spreading of the wavepacket, and therefore the loss of control, by keeping the system tightly localized. To do this, the local tracking algorithm was used for the simultaneous, competitive tracking of both the position expectation value and the expectation value of $\hat{\mathbf{x}}^2$. From these two values, it is possible, to construct the variance of the wavepacket, which should be kept minimal during the control, to ensure a localized system. While this approach also did not manage to keep $\langle\hat{\mathbf{x}}\rangle$ on the desired target track, after crossing the barrier in the DM potential studied, the field now indeed kept the wavepacket localized for a longer time. This stronger localization allowed the algorithm, to guide part of the wavepacket into the desired product well, while leaving a smaller component split off on the reactant side. Due to this split, the total expectation value of the system does not reproduce the classical target track at all, after the wavefunction has divided at the barrier. This causes the error control terms in the algorithm, which rely on the deviation of the expectation value from the track, to produce corrections, which are unnecessary for the

main part of the wavefunction, und wrong for the small part, which has split off from it. Unfortunately, these error terms are needed, to allow the competitive tracking algorithm to work at all, so only some combination of weights for the constants ρ_i controlling the error damping produces useful results. (The values used in the calculations presented are listed in Table 3.1.) As very small changes in these coefficients produce completely different results, and no direct causal connection between the change in them and the quality of the tracking could be identified, the algorithm in principle replaces the search for good pulse parameters with the search for good error damping parameters. Here the difference is, that one can make good guesses at reasonable values for laser pulse parameters, which is not true for the error control terms. At the same time, the tracking algorithm produces an unreasonably strong field and is not stable against the inclusion of dissipation, as shown in Fig. 3.29.

With these facts in mind, the method of inverse tracking control as presented here, cannot be recommended for the calculation of control fields for a proton transfer reaction, as these always have to deal with double minimum potentials. Therefore all the problems with splitting wavepackets discussed above cannot be avoided in these systems, making the method of position tracking unsuitable for reaction control. In a recent work by Fujimura [116] an approach using not the position expectation value, but the kinetic energy as an control parameter produced promising results for control even in double minimum systems.

Genetic Algorithms

To allow the control of a quantum system with a genetic algorithm (GA), as presented in Section 2.5.3 and Appendix B, two main conditions have to be fulfilled:

1. The quantity, which one wants to control has to be encoded into a form usable for a GA. In the application to the control of a quantum system, this means, that the parameters of the laser pulse, which is supposed to control the wavepacket, have to be coded into genetic strings, as described in Appendix B.

2. A quality function has to be defined for the parameters to be controlled. This function defines the fitness of an individual in the parameter space searched. This fitness should be given as a single number between zero (completely unfit) and one (perfect specimen). The definition of this function depends on the desired results.

In the scenario of the laser control of a quantum system, one normally has a defined initial state $|\phi_i\rangle$, which one wants to drive into a known target state $|\phi_f\rangle$. The laser pulses acting on the initial state are encoded into genetic strings, resulting in the population, which has to be optimized with the GA. The quality of each individual can then be defined by the amount of population transferred by each pulse into the target state, i.e. if the field of the n^{th} individual results in a time evolution operator $\hat{\mathbf{U}}_n(t)$, acting on the initial state, the overlap $|\left\langle \hat{\mathbf{U}}_n\phi_i \right| \phi_f\rangle|$ defines the quality function for the laser pulse.

After the definition of the quality function for an individual laser pulse, a suitable parametrization of the pulse has to be chosen. If one wants to model the experimental pulse shaper used by Gerber [37], it would be necessary to split the pulse into the 128 Fourier components, which can be addressed by the model used there. As this number of parameters results in an enormous parameter space to be searched, this type of parametrization was not chosen for the following calculations. Instead, the laser is parametrized as a sequence of $\sin^2$–pulses, as defined by Eq. (2.144), which require only four parameters per pulse: initial time t, length τ, amplitude E_0 and frequency ω. For the models in the following sections, a sequence of either two or three of these pulses is used, to allow for processes like the pump–dump scheme sketched in Fig. 2.3.

1D Models

As a model potential in the one dimensional case, again the DM potential defined for the driven tunneling in Section 3.1.1, both with the low and the high barrier, is used. To allow the pump–dump type of reaction path, a sequence of two or three $\sin^2$–pulses is used in this scenario, resulting in a total number of eight or twelve parameters, which have to be searched. Within the GA used, each of these parameters is encoded into a 20 digit binary string, resulting in $2^{20} - 1$ possible values for each of them. In this approach, a suitable range has to be chosen for each of the parameters, to fix the grid spacing of the discrete encoding. This shows the limitation of this approach: One can either choose a very large interval, scanning a wide range of the parameter, but resulting on a rather coarse grid, or narrow the range, giving a fine grid but limiting the flexibility of the pulse. In the first case, one can generate unexpected types of pulses, but due to the large grid spacing normally cannot reach very good control, as the optimal parameters normally lie between two grid points. In the second case one has to do a preselection of the available parameter space, which already prescribes a certain type of reaction path.

The first calculations are done for the low barrier system, without coupling to the environment. The laser pulse is restricted to two $\sin^2$–pulses, while the eight parameters of these pulses are allowed to vary in a wide range. The initial and final times of both pulses is only restricted to fall within the total simulation length of $40000\,\hbar/E_h (\approx 1\,\mathrm{ps})$. The amplitude can vary between zero and $0.003 E_h/ea_B$, and the frequency between zero and $4.5 \cdot 10^{-3} E_h/\hbar$. This upper limit has been selected, as the energy difference between Ψ_1 and Ψ_3 is only $4.2 \cdot 10^{-3} E_h/\hbar$, so any higher frequency pulse would pump into higher, undesired states. So while the parameters can vary relative freely, here already a restriction based on the previous knowledge of the eigenstates of the system is included into the calculations. In the further calculations, an "unrestricted" parameter space is a set of parameter as above for each pulse, with the upper limit of the allowed frequencies set to a value above the barrier. For all GA calculations using two pulses, the number of generations was limited to $N_{\mathrm{gen}} = 500$ and the population size of each of these generations was just $N_{\mathrm{pop}} = 5$.

The target of the GA control is set to the population of the lowest vibrational level in

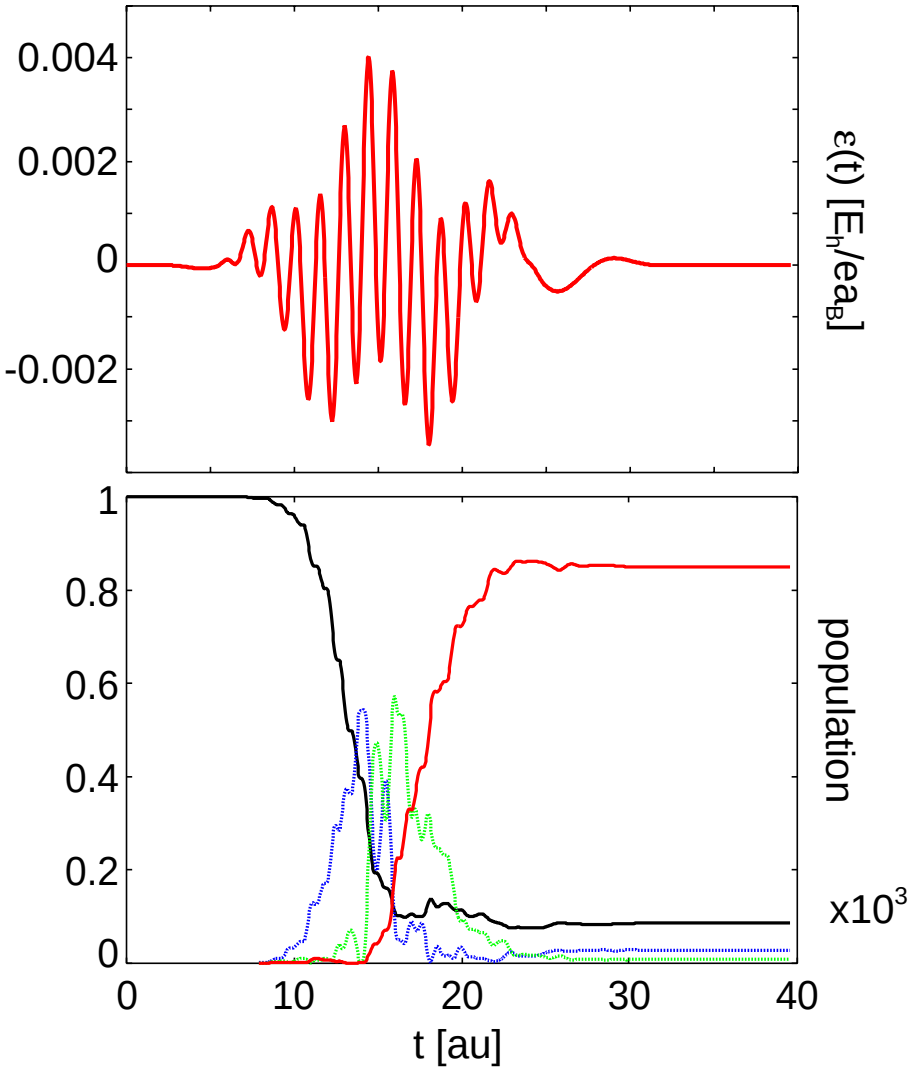

Figure 3.30: The electrical field generated by the GA for the low barrier malonaldehyde model. In the lower panel the population dynamics induced by the field is plotted (Ψ_1: solid black; Ψ_3: dotted blue; Ψ_4: dotted green; Ψ_2: solid red). The pulse parameters are given in Table 3.2 on page 115.

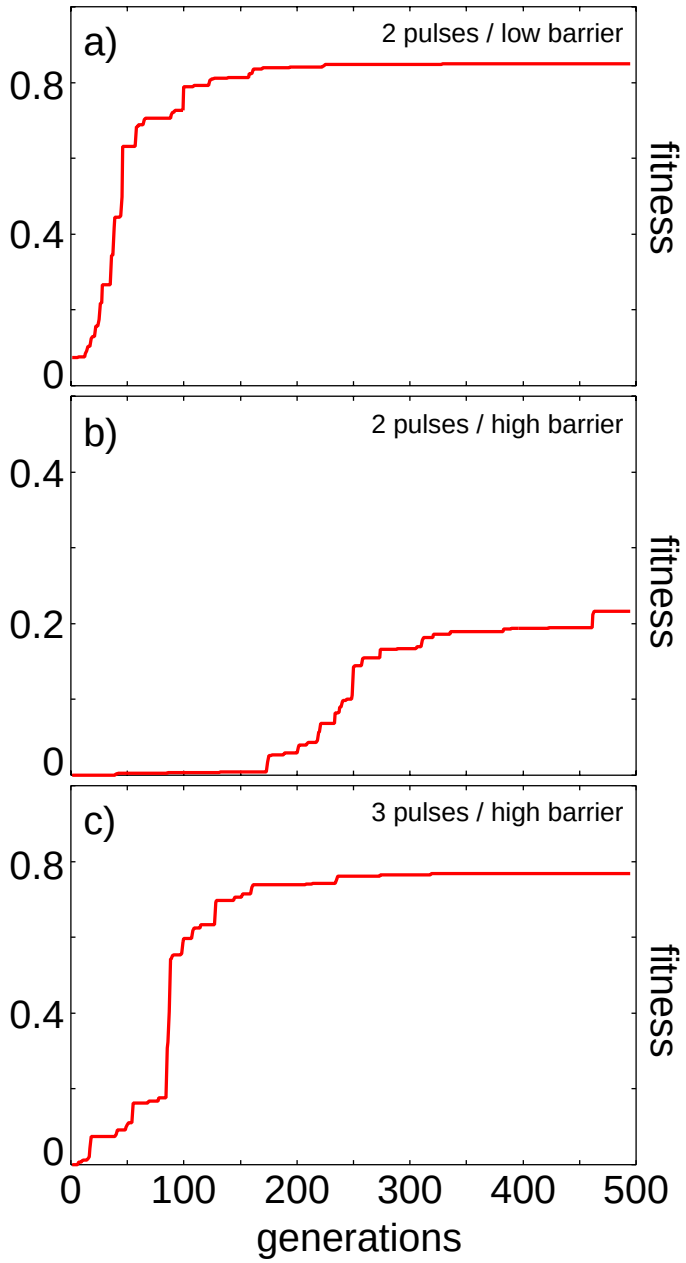

Figure 3.31: The typical efficiencies of the laser control, generated by a GA, for the transfer from the reactant to the product well. Panel **a)** show the efficiency of the algorithm for an optimization of a two pulse laser in the low barrier case, as presented in Fig. 3.30. In panel **b)** the optimization for the same pulse is tried for the high barrier (Fig. 3.34). Here the pulse does not have enough parameters to reach good efficiency. In panel **c)** nearly the same quality as in a) is regained by adding a third pulse to the field (Fig. 3.36).

the target well, i.e. to $|\Psi_2|^2$. The resulting efficiency of the control is plotted in panel **a)** of Fig. 3.31. One sees clearly, that the random starting population of pulses has a fitness of close to zero. This could be expected, as the chance of starting with a good control pulse in the large parameter space possible is highly unlikely. The GA then starts with its random mutations and recombinations to improve the total fitness of the population. As the laser control is very sensitive to small changes, i.e. a very small detuning from an optimal pulse leads already to small efficiencies, the first improvements happen in relatively big jumps. These occur, when one of the random mutations or recombinations by chance created an individual close to the optimum. This pulse then either gets replaced by a completely different specimen, which in turn was generated via random mutations, or slowly takes over the population and slowly refines itself via recombinations. This happens mostly, when the pulse is already close to optimal, and all big parameter variations would only lead to a worse fitness. When this point is reached, only very small and infrequent increases in the efficiency can be seen. The total population transfer reached with a two pulse scheme, optimizing 8 parameters in a mostly unrestricted parameter space is 0.86. As the algorithm has spend quite a long time on a flat efficiency plateau, it is unlikely, that a much better pulse can be found. To reach 100% transfer, the values allowed by the grid in parameter space, which is quite coarse, due to the large ranges defined, would have to hit the true optimal values. This again is unlikely, so to increase the population transfer further, the parameter space has to restricted to get a finer mesh size.

Even though the results are not perfect, one already sees, that an unrestricted GA can generate good control pulses. Looking at the population dynamics in Fig. 3.30, one also sees, that the field generated drives the wavepacket along a reaction path not found before. (The pulse parameters for this and all following pulses are given in Table 3.2 on page 115.) The driven quantum tunneling presented in Section 3.1.1 requires a form of the field, which cannot be reproduced with the two $\sin^2$–pulses, so it is not surprising, that this is not found. The GA manages to find a pulse, which does not follow the classic pump–dump scheme $\Psi_1 \rightarrow \Psi_3 \rightarrow \Psi_2$ one would choose when designing analytical pulses. Instead, it tunes the frequencies in such a way, that the transfer follows the path $\Psi_1 \rightarrow \Psi_3 \rightarrow \Psi_4 \rightarrow \Psi_2$, using one high frequency pulse for the pump $\Psi_1 \rightarrow \Psi_3$ and for the dump $\Psi_4 \rightarrow \Psi_2$ and one low frequency component for the transfer $\Psi_3 \rightarrow \Psi_4$.

In contrast to this, it is possible to restrict the frequencies of the two pulses to a parameter range around the values required for the process $\Psi_1 \rightarrow \Psi_3 \rightarrow \Psi_2$. This is shown in Fig. 3.32. Even though the allowed parameter range for the frequency now is much smaller, the control efficiency increases only marginally. To reach perfect transfer, even more restrictive ranges are necessary. What can be seen in the plot of the population dynamics is, that now really only Ψ_3 is significantly populated, and the laser pulse consists of two overlapping components with slightly different frequency.

In the next calculation, dissipation in the Redfield approach is added to the calculation. The coupling is set to the value for weak system–bath interaction ($\alpha = 0.01\lambda$; cf. Fig. 3.4)

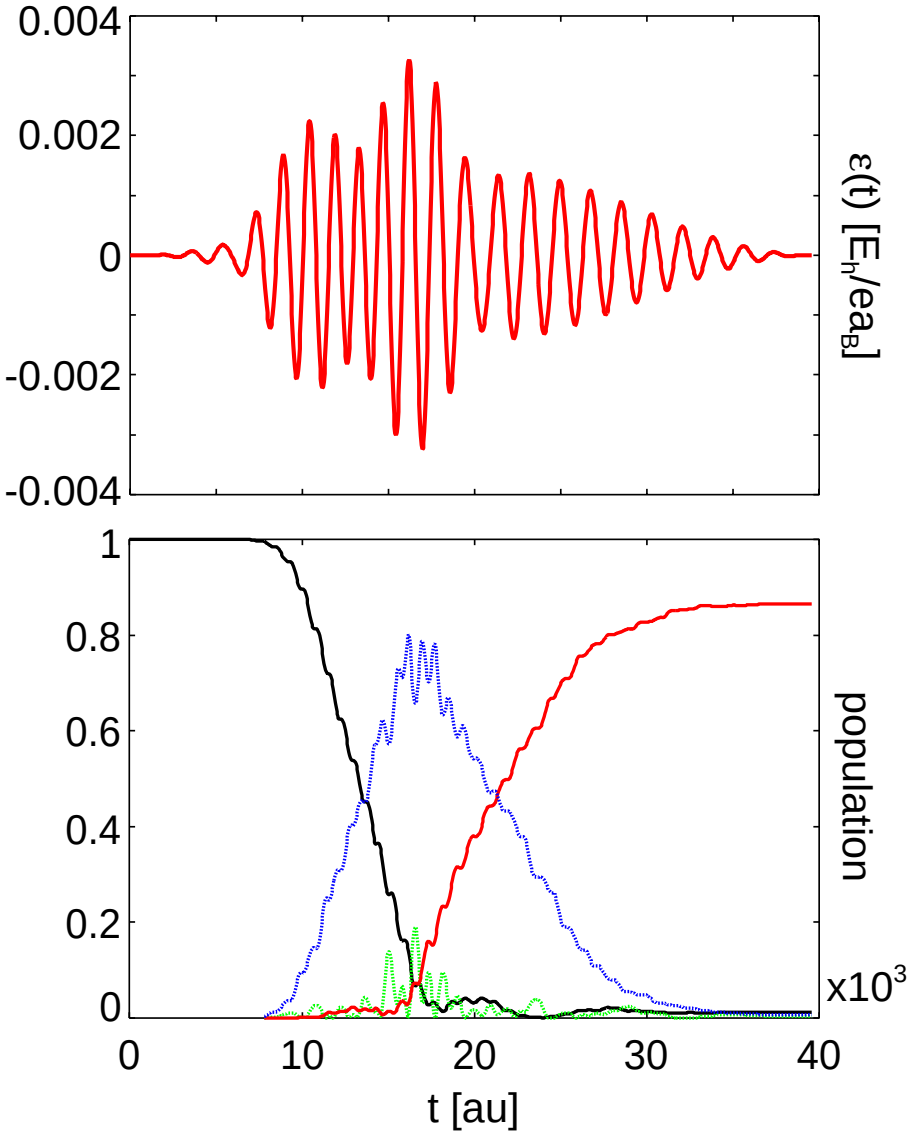

Figure 3.32: Same as in Fig. 3.30, only with a smaller allowed parameter range for the GA. Instead of the full frequency range, the pulses are now limited to a narrow region fitted to the pump–dump process $\Psi_1 \rightarrow \Psi_3 \rightarrow \Psi_2$. Color coding in this (and all following pictures of this type) as in Fig. 3.30. The pulse parameters are given in Table 3.2 on page 115.

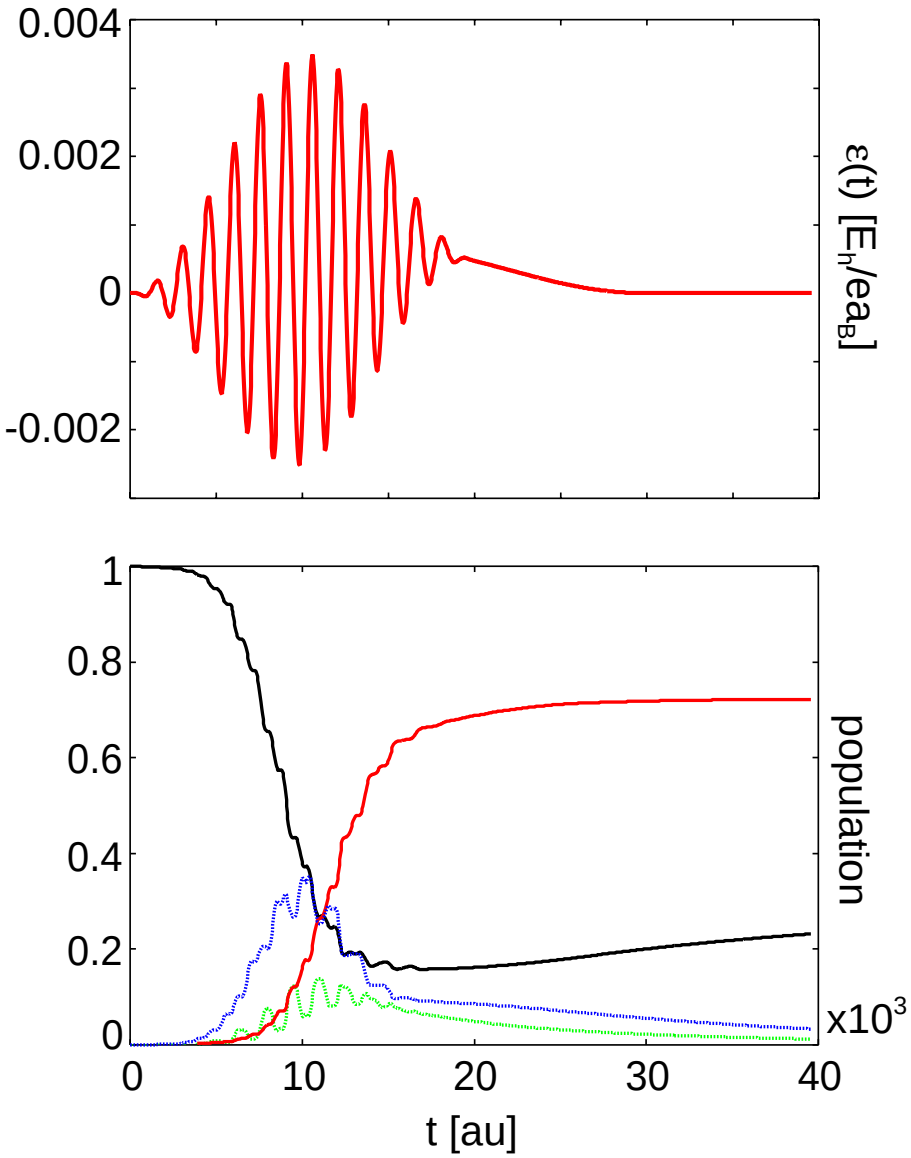

Figure 3.33: Same as in Fig. 3.30, only with added dissipation. The pulse parameters are given in Table 3.2 on page 115.

and the parameters are again allowed to vary freely, as for the calculations for Fig. 3.30. The simulations for the driven quantum tunneling with dissipation showed, that population transfer via higher excited states is not very efficient in the presence of system–bath interactions. The same result is found by the GA. Even though the initial conditions are exactly the same as for the first calculation, the algorithm now does not generate the reaction path including Ψ_4. Instead, one pulse has an almost zero frequency, resulting in a field very close to the plateau type field found for the driven quantum tunneling in Section 3.1.1. The second pulse drives an excitation into Ψ_3, from where the population decays into both the reactant and the product ground state. This pulse corresponds to the first part of the pump–dump scheme, where the dumping is left to the dissipation. Most of the population transfer is driven by the "zero frequency" pulse, which avoids the higher excited states. This pulse sequence generates a population of more than 0.72 in the target state Ψ_2 at the end of the total time. The field already stops halfway through the calculation, to allow the population pumped into Ψ_3 to decay back into the ground state.

Moving to the model potential with the higher barrier used in Section 3.1.1, one sees the first limits of the GA approach. After increasing the height of the barrier, and still only allowing a sequence of two pulses with large, unrestricted parameter intervals, the algorithm is not able to find a good control pulse to reach the ground state of the target well efficiently. The limited flexibility of the 8 parameters does not allow a good reaction path for this type of transfer. This can also be seen in panel **b)** of Fig. 3.31, which shows that the calculation already has difficulties starting, spending several hundred iterations finding the first pulse producing any kind of transfer. The final efficiency is only slightly above 0.2, even though the initial state has been nearly completely depopulated. Most of the population is pumped to higher levels, and not dumped into the desired state. For this process, a much longer time would be required, as the states above the barrier are only weakly coupled to the initial and target levels. To give the algorithm additional flexibility in the available time, a third laser pulse is added to the system.

The initial calculation with the third pulse, using again an unrestricted parameter space, produced no improvement of the transfer rate, but results in an efficiency of just 0.15. Looking at the laser field generated, and the population dynamics induced by it shows, that the first pulse does not affect the system at all, i.e. the actual effect is that of a two pulse control, with a third pulse just increasing the complexity of the GA. In fact, if the algorithm is left some more time, the first, ineffective pulse is bound to mutate to something useful, but the large parameter space available makes this very unlikely. As the GA calculated for the same number of generations ($N_{\mathrm{gen}} = 500$) as the previous runs, and the size of each generation was already doubled to $N_{\mathrm{pop}} = 10$, this can take quite some time to happen.

Instead of continuing the search in the unrestricted parameter space, the ranges were narrowed down to represent a pump–transfer–dump process along the eigenstates $\Psi_1 \rightarrow \Psi_3 \rightarrow \Psi_4 \rightarrow \Psi_2$. The efficiency of this calculation is plotted in panel **c)** of Fig. 3.31. One

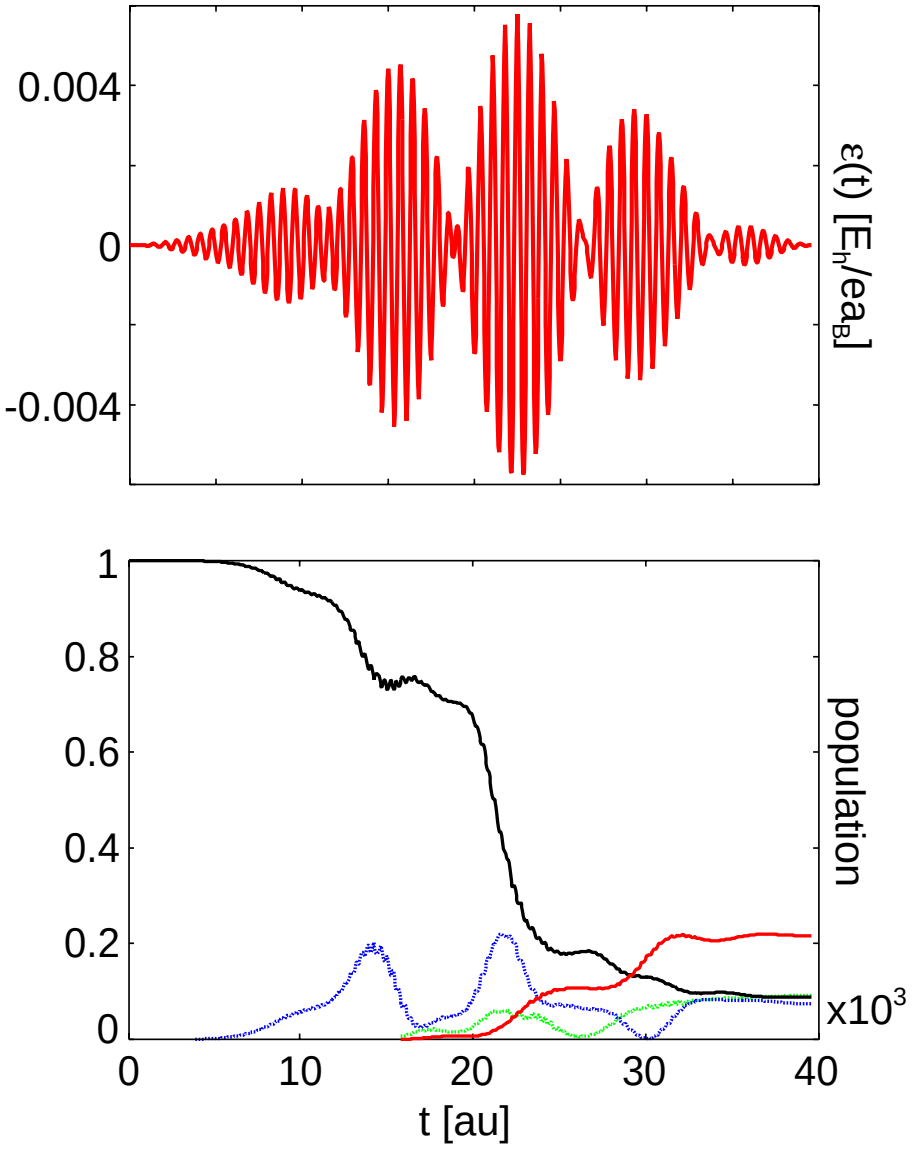

Figure 3.34: The GA with only two laser pulses is not very efficient for the high barrier model (cf. the efficiency plot in panel **b)** of Fig. 3.31). Even though the ground state gets depopulated, the two pulses have not enough flexibility to reach the ground state in the target well. The pulse parameters are given in Table 3.2 on page 115.

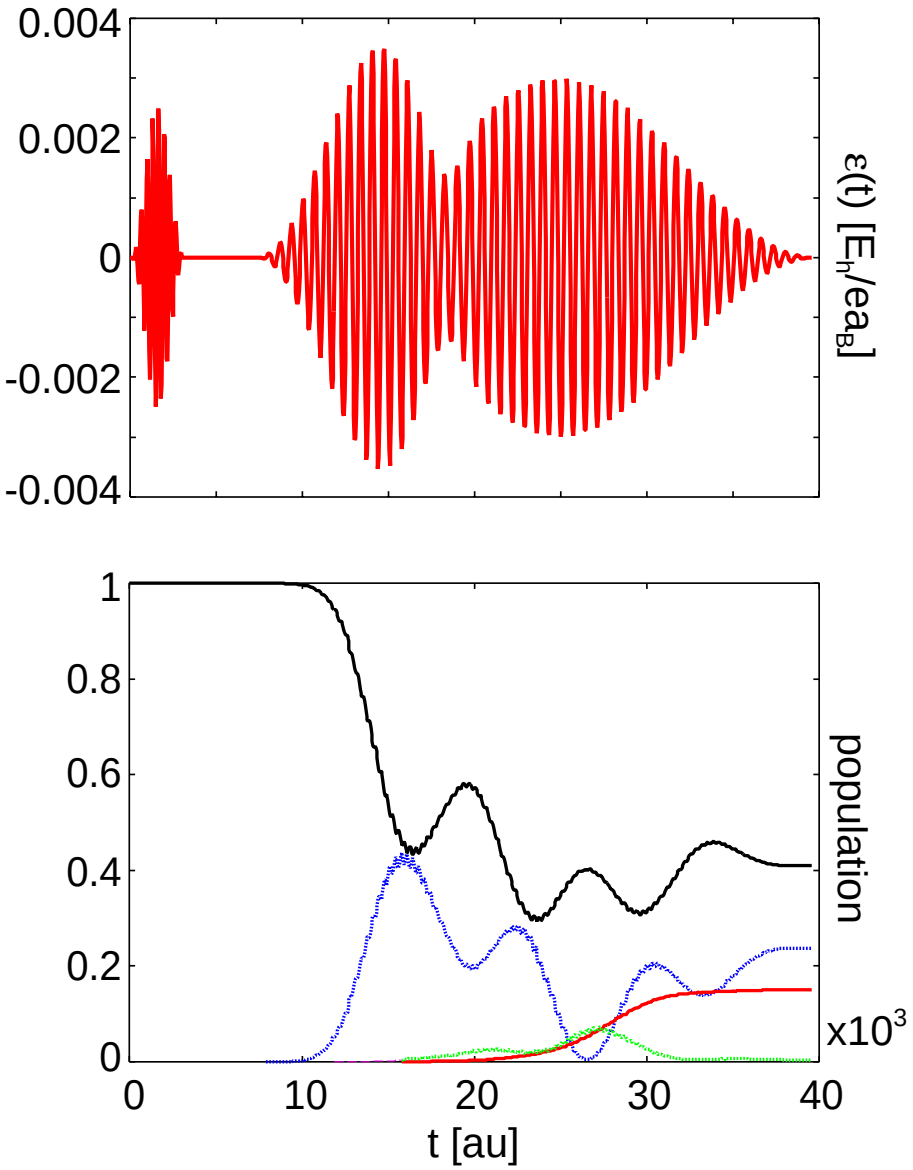

Figure 3.35: A third laser pulse has been added to the GA, increasing the flexibility. This in principle would allow for a better efficiency of the control found by the GA. Still the result is worse than before, as four parameter are added to the search space, resulting in a very slow convergence of the genetic search. The pulse parameters are given in Table 3.2 on page 115.

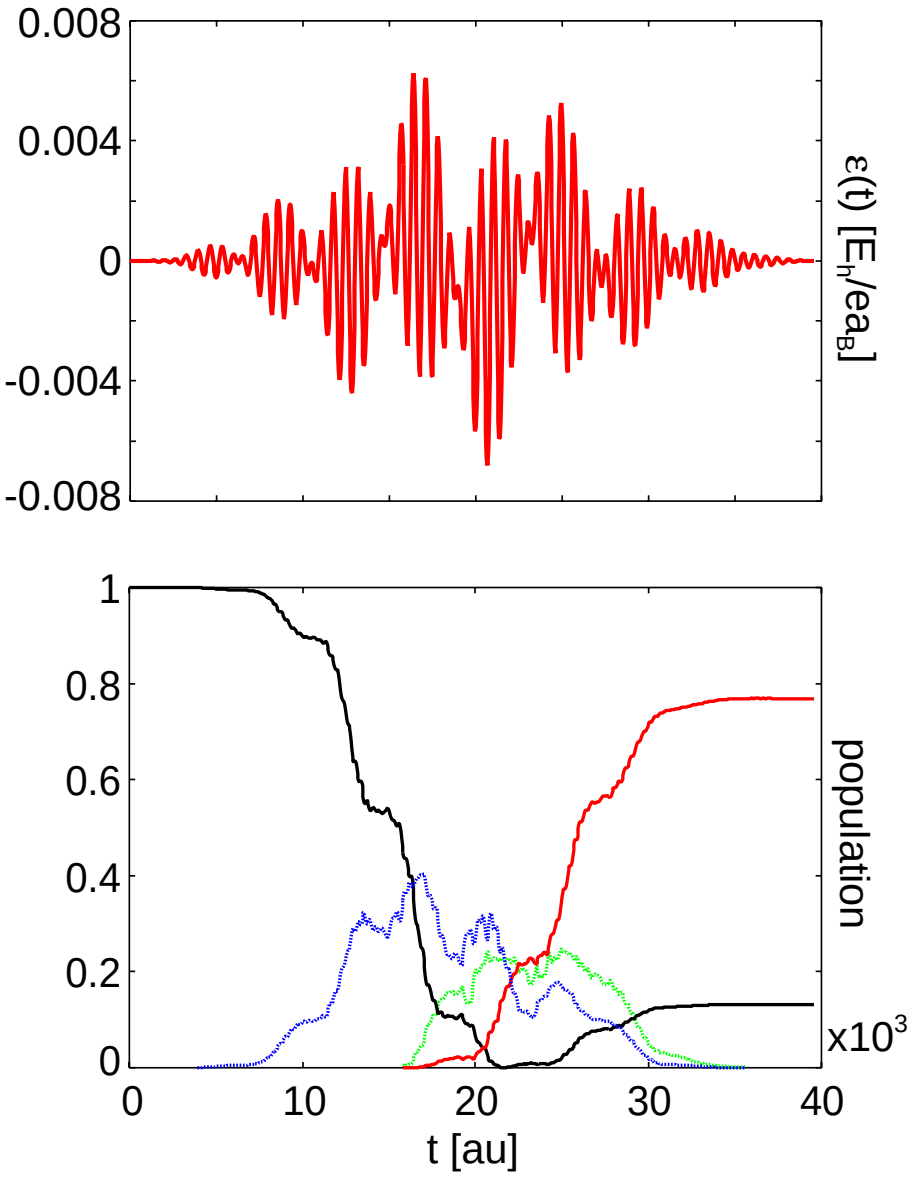

Figure 3.36: Limiting the parameter search to a region close to the reaction path representing an excitation scheme in the form $\Psi_1 \rightarrow \Psi_3 \rightarrow \Psi_4 \rightarrow \Psi_2$ finally regains good control pulses. The pulse parameters are given in Table 3.2 on page 115.

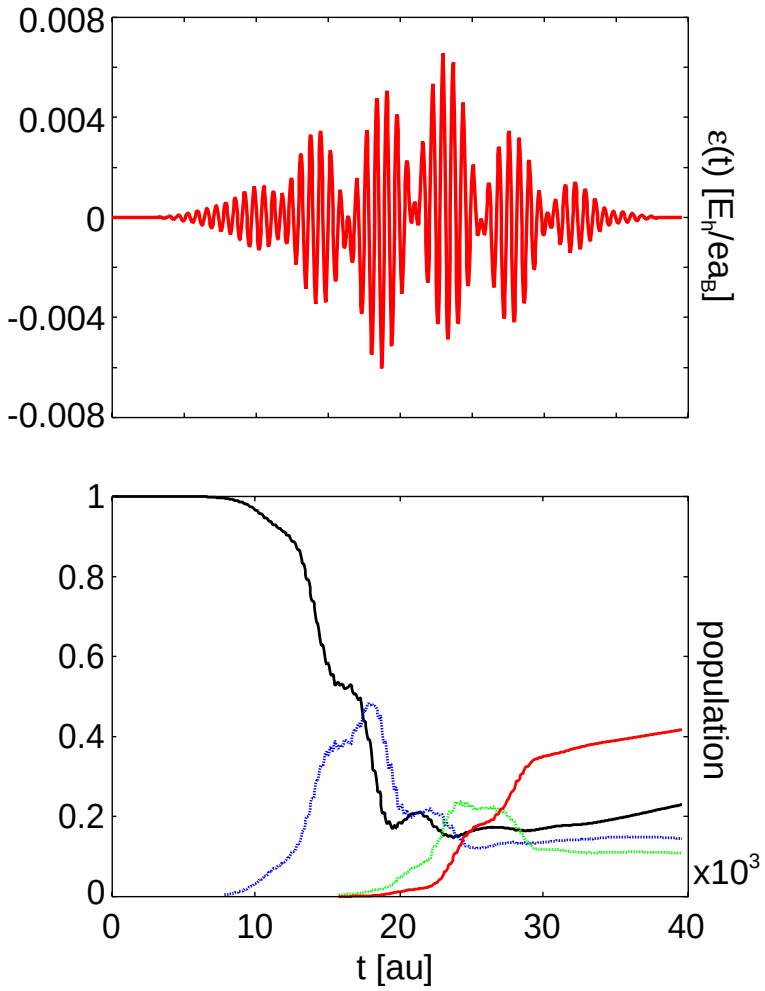

Figure 3.37: The same, parameter restricted search as in Fig. 3.36 only with dissipation added to the propagation. The pulse parameters are given in Table 3.2 on page 115.

can see, that with these restrictions on the parameter space the GA converges nearly as fast as the two pulse scheme for the low barrier. The field finally generated consists of two high frequency pulses, inducing the pump from Ψ_1 and the dump into Ψ_2 and a low frequency one, coupling the tunneling doublet Ψ_3 and Ψ_4. The resulting efficiency is nearly 0.8. The lower yield compared to the system with the smaller barrier height is caused by the fact that the high frequency pump/dump–pulses transfer some of the population to levels above the third/fourth.

As for the low barrier system, the GA in the high barrier one is checked for its behavior versus the inclusion of dissipation. Again, only a low coupling strength to the environment is calculated ($\alpha = 0.01\lambda$) and the parameters are kept restricted to the values of the

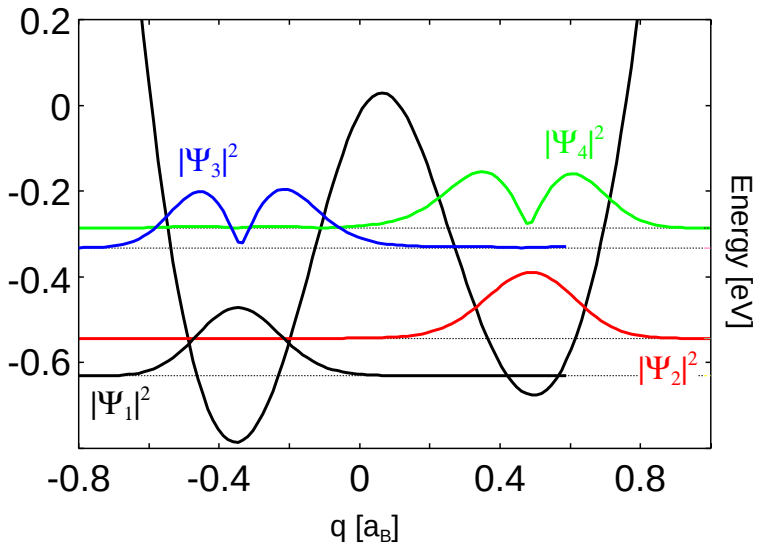

Figure 3.38: A slightly different one dimensional model potential, was also used for the GA calculations. This has a higher asymmetry than the one for malonaldehyde and two different frequencies for the reactant and target well. Shown are the two lowest doublets of eigenfunctions. The parameters used are: $k_1 = 37.14 E_h/a_B^2$, $x_1^0 = -0.45 a_B$, $\Delta_1 = 0 E_h$, $k_2 = 26.9 E_h/a_B^2$, $x_2^0 = 0.6 a_B$, $\Delta_2 = -0.05 E_h$, $k_c = 4.3 E_h$, $C = 1 a_B^{-1}$ and $x_c = 0.092 a_B$.

previous calculation. This time, the resulting laser pulse does not change its character, compared to the calculation without dissipation, as the restrictions in the parameter space do not allow too big deviations. (A calculation with an unrestricted parameter space again led to extremely small efficiencies.) As in the case of the pump–tunnel calculations for the driven quantum tunneling in Section 3.1.1 the fact, that one has to go to an excited state, before the transfer can start, reduces the efficiency significantly. Otherwise the dynamics still mainly follows the same reaction path as in the calculation without dissipation ($\Psi_1 \rightarrow \Psi_3 \rightarrow \Psi_4 \rightarrow \Psi_2$), with some excitation to higher levels. For the dissipative case, this higher excitation actually helps the transfer somewhat, as the decay of the population goes partly into the correct well. One can also see, that at the end of the calculation the population of Ψ_2 is still increasing, as there is still some occupation left in Ψ_4, which mostly decays into the ground state of the target well.

In addition to the already well studied model potential for malonaldehyde and its high–barrier derivative, a different model potential was examined. While for the malonaldehyde model, both sides of the DM potential have the same frequency, now a potential in the form

$$V(x) = \frac{1}{2}\left(V_1(x) + V_2(x) - \sqrt{(V_1(x) - V_2(x))^2 + 4k(x)^2}\right), \tag{3.15}$$

is used, describing the adiabatic coupling of the two potentials $V_1(x)$ and $V_2(x)$ with the

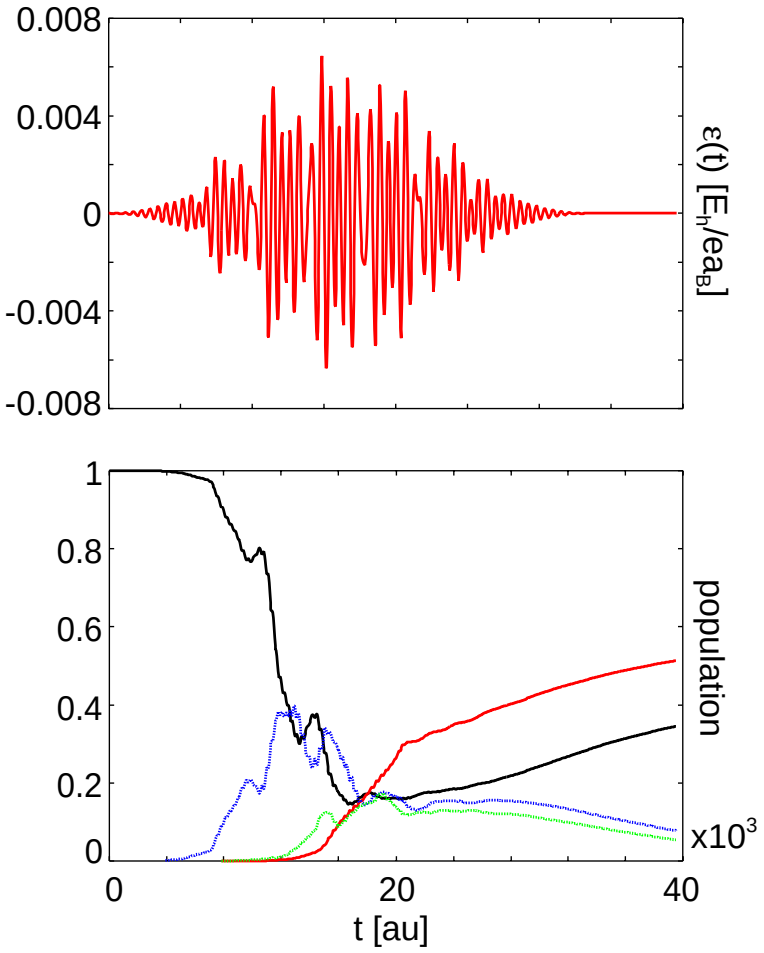

Figure 3.39: The GA calculations for the model potential, using the same conditions as for the calculation shown in Fig. 3.37, find a quite good control pulse, transferring more than 50% of the population to the target state. The pulse parameters are given in Table 3.2 on page 115.

coupling function $k(x)$. By choosing harmonic oscillators with different frequencies for the functions, one gets a DM potential with different local frequencies in reactant and product states. This models a typical $\mathbf{X} - \mathbf{H} \cdots \mathbf{Y}$ hydrogen bond system. The functions used here are $V_n(x) = \frac{1}{2}k_n(x - x_n^0)^2 + \Delta_n$, $n = 1, 2$ and $k(x) = k_c \exp\{-C(x - x_c)^2\}$. The resulting potential has a higher asymmetry than the one used for the driven quantum tunneling and, for a particle of proton mass, changes from an effective frequency of $\approx 2400\,\mathrm{cm}^{-1}$ on the reactant side to $\approx 2000\,\mathrm{cm}^{-1}$ in the product well. In Fig. 3.38 this potential, together with the four lowest eigenstates is plotted. For the following calculations, the dipole is set to be linear $\mu(x) = \mu_0 x$ with $\mu_0 = 0.75e$.

Applying the GA approach to this potential produced results comparable to the ones

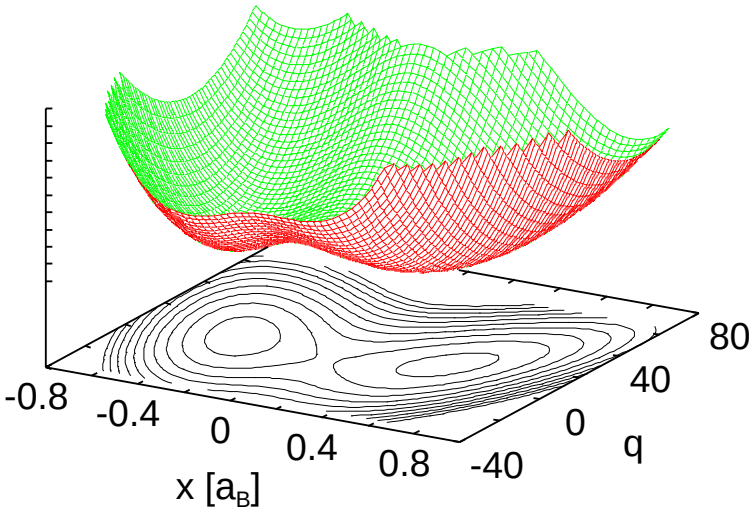

Figure 3.40: Two dimensional model potential, used for the GA calculations. The model potential from Fig. 3.38 is extended by a mode with an quadratic coupling to the DM potential. The frequency of the added mode is $1200\,\mathrm{cm}^{-1}$ for a mass of $1m_e$, the parameters used are $k_q = 2.9 \cdot 10^{-3}\ E_h/a_B^2$, $c_q = 50$.

found for the high barrier driven quantum tunneling potential. Again a control with two pulses has not enough flexibility to control a transfer reaction. The calculation with three pulses only converges extremely slowly for unrestricted parameters, so that no good control pulse has been generated from them. The calculations made with restricted parameters, targeting the same type of reaction path as in Fig. 3.36, also produced similar results. The main difference is a lower efficiency of this type of path, as the higher asymmetry lowers the coupling between the wavefunction doublets in the two wells.

For a calculation including dissipation, this lower coupling also helps reaching a better control efficiency. Using three pulses with restricted parameters, more than 50% of the population could be transferred to the target state, as shown in Fig. 3.39. While the laser pulse generated by the GA behaves like the one seen in Fig. 3.36, the population decaying from higher excited states into the target well is trapped more efficiently, due to the smaller coupling between the wells. On the time scale of $\approx 1\,\mathrm{ps}$ studied, this results in a more efficient control scenario for the adiabatic model potential.

2D Models

As a final application of the GA, a look is taken at an extension of the 1d potentials of the last section to two dimensions. For this, to the potential defined by Eq. (3.15) a harmonic normal mode is added:

$$V_{2d}(x,q) = V(x) + V_q(x,q) \tag{3.16}$$

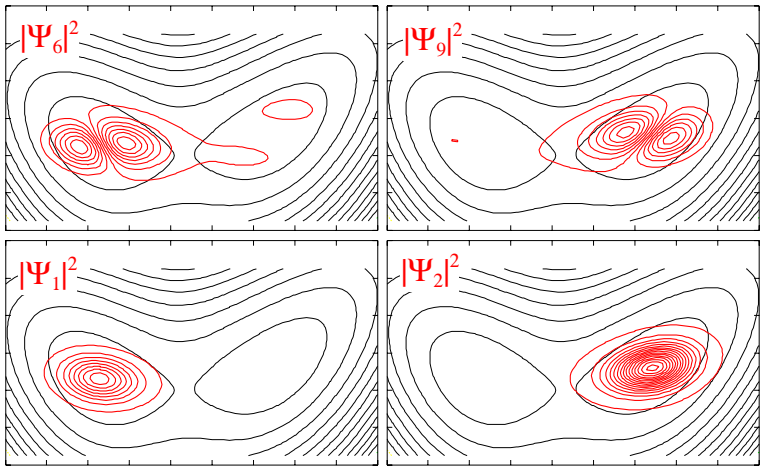

Figure 3.41: Eigenfunctions in the 2d model potential. The eigenfunctions shown represent the two lowest tunneling doublets from the 1d potential in Fig. 3.38, for which the added mode is in its ground state.

with $V_q(x,q) = \frac{1}{2}k_q(q - c_q x^2)^2$. Here the coupling of the normal mode to the x coordinate is of quadratic form. The resulting potential is plotted in Fig. 3.40.

If one stays in the stationary eigenstate picture to analyse the possible transfer from one well to the other, one finds that the functions corresponding to the four lowest states in the one dimensional model, with the added normal mode in its ground state, are still good candidates for population transfer. These four levels again have the necessary properties to try the pump–tunnel approach introduced in Section 3.1.1. In addition to this, one can study, whether the added dimension allows the GA to find other suitable control strategies not possible in 1d. What immediately comes to mind would be a reaction path exploiting the fact, that the direct, i.e. straight line, transfer from reactant to product now sees a higher barrier than a curved path, which requires moving also along the normal mode. To follow this curved path, it is necessary to excite a wavepacket which also moves along q.

The GA calculations show, that the algorithm is not able to generate good control pulses for the 2d system. The best control found after extensive searching, using both unrestricted and restricted parameter spaces, is presented in Fig. 3.43, which shows an calculation restricted to a parameter set close to allowing transfer via the levels shown in Fig. 3.41. The population dynamics shows, that most of the transfer does not move via the levels suitable for tunneling, but via a higher excited state (Ψ_{16}), which also contains no excitation of the normal mode coordinate. In Fig. 3.42, the IR spectrum shows this normal mode only weakly, and due to its high frequency no vibrational progression can be observed. If dissipation is included into the system, the efficiency reached depends mainly on the maximum value of the allowed electrical field. The higher density of states, as compared to the 1d system, decreases the lifetime of population in an excited state. The

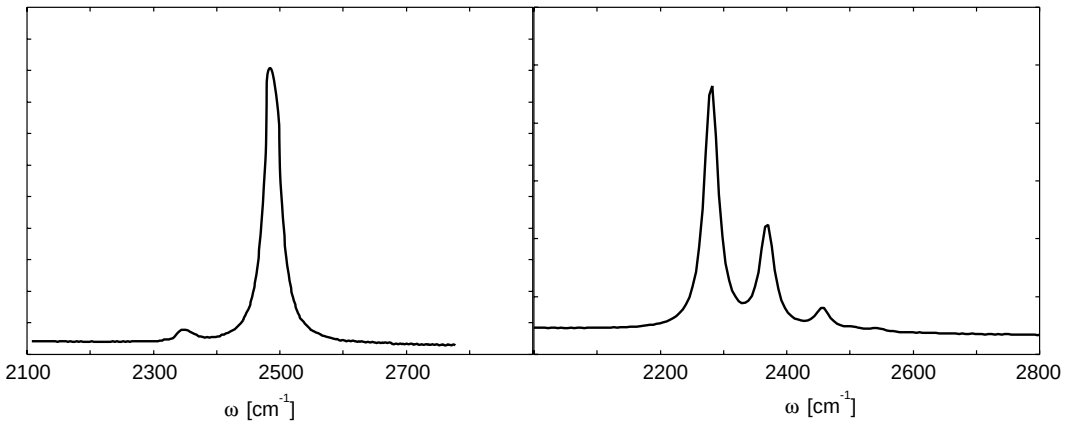

Figure 3.42: The stationary IR spectra for the two 2d models (IR spectra and lineshapes are discussed in more detail in Section 3.3.1). In the case of the high frequency normal mode (left panel), one can only observe this frequency in its first overtone directly. For the low frequency mode (right panel), one can observe a vibrational progression added to the system frequency.

only efficient way to control the 2d dissipative system, which has been found by the GA in this case, is to pump the population as far up as possible with the available field strength, and then to rely on the dissipation into the target well to populate the desired target state.

The situation is even worse for the final 2d potential checked. This also starts with the model potential Eq. (3.15), but with an additional low frequency normal mode, instead of a high frequency one. In this potential, the lower normal mode frequency should increase the chance of wavepacket excitation along it. The parameters used for $V_q(x,q)$ are $k_q = 2.9 \cdot 10^{-5}\, E_h/a_B^2$ and $c_q = 500$, resulting in a frequency of $120\,\mathrm{cm}^{-1}$. The IR spectrum of this model shows a small, but distinct vibrational progression, as seen in Fig. 3.42. This system has such a high level density, that the targeting of a single state cannot be done with the GA applied. The efficiency reached for such a control is plotted in panel **a)** of Fig. 3.44. To get a more useful definition of the fitness of the laser, the efficiency is redefined as the sum of the populations of all levels located below the barrier in the target well. The resulting efficiency is plotted in panel **b)** of Fig. 3.44. While this shows, that control is still possible, one looses any state selectivity, as each level summed into the efficiency is weighted equally. The GA again moves the population mostly via states excited along the model potential, with no component, and therefore no dynamics in the normal mode direction. This shows, that the picture of exciting a scaffold mode to aid the proton transfer is not valid for the models presented. The random search of the genetic algorithm only selects population transfers via the much stronger coupled system mode, while the weakly coupled (as seen from the IR spectrum) normal mode is ignored. For this method to work, it would be necessary to have a strong dipole coupling along the scaffold mode to

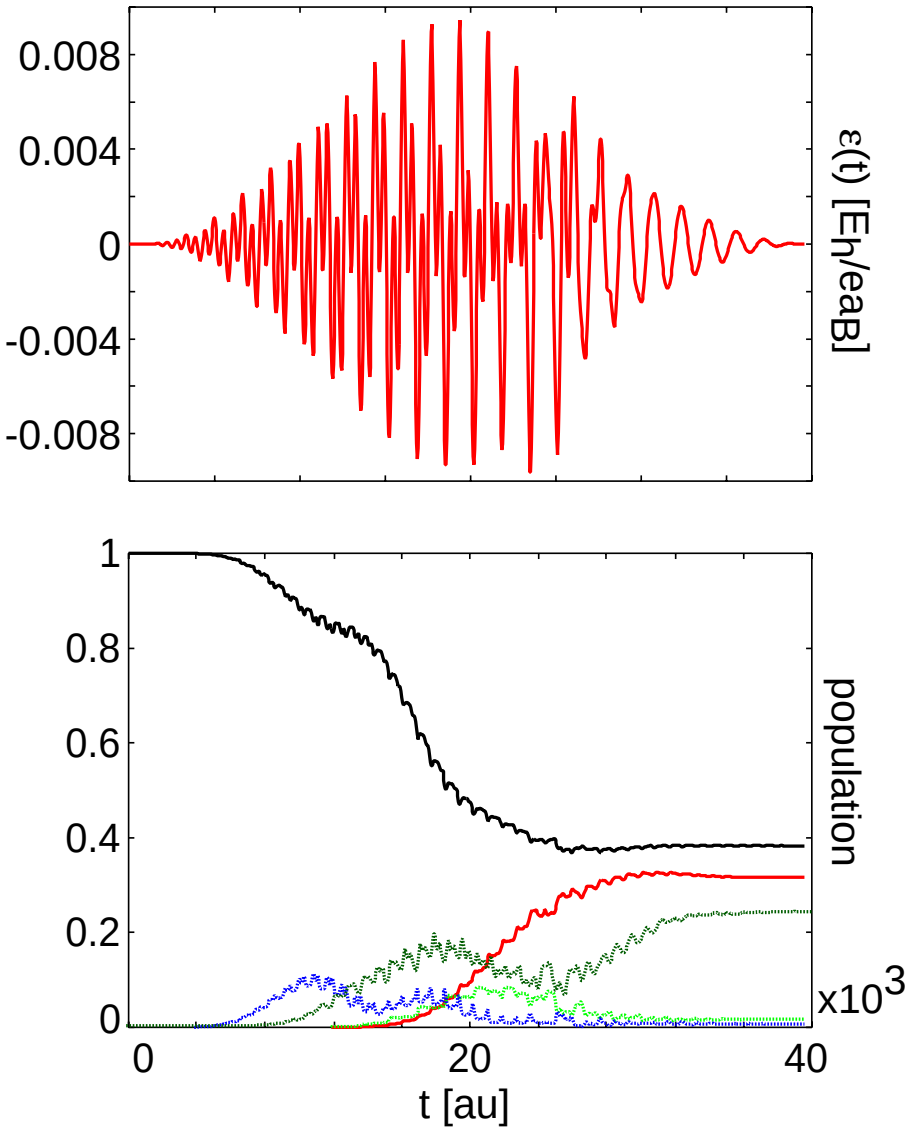

Figure 3.43: The electrical field generated by the GA for the two dimensional model with high frequency coupling mode and no dissipation. In the lower panel the population dynamics of the levels presented in Fig. 3.41 and the one higher excited state, which is significantly populated are plotted (Ψ_1: solid black; Ψ_6: dotted blue; Ψ_9: dotted light green; Ψ_{16}: dotted dark green; Ψ_2: solid red). The pulse parameters are given in Table 3.2 on page 115.

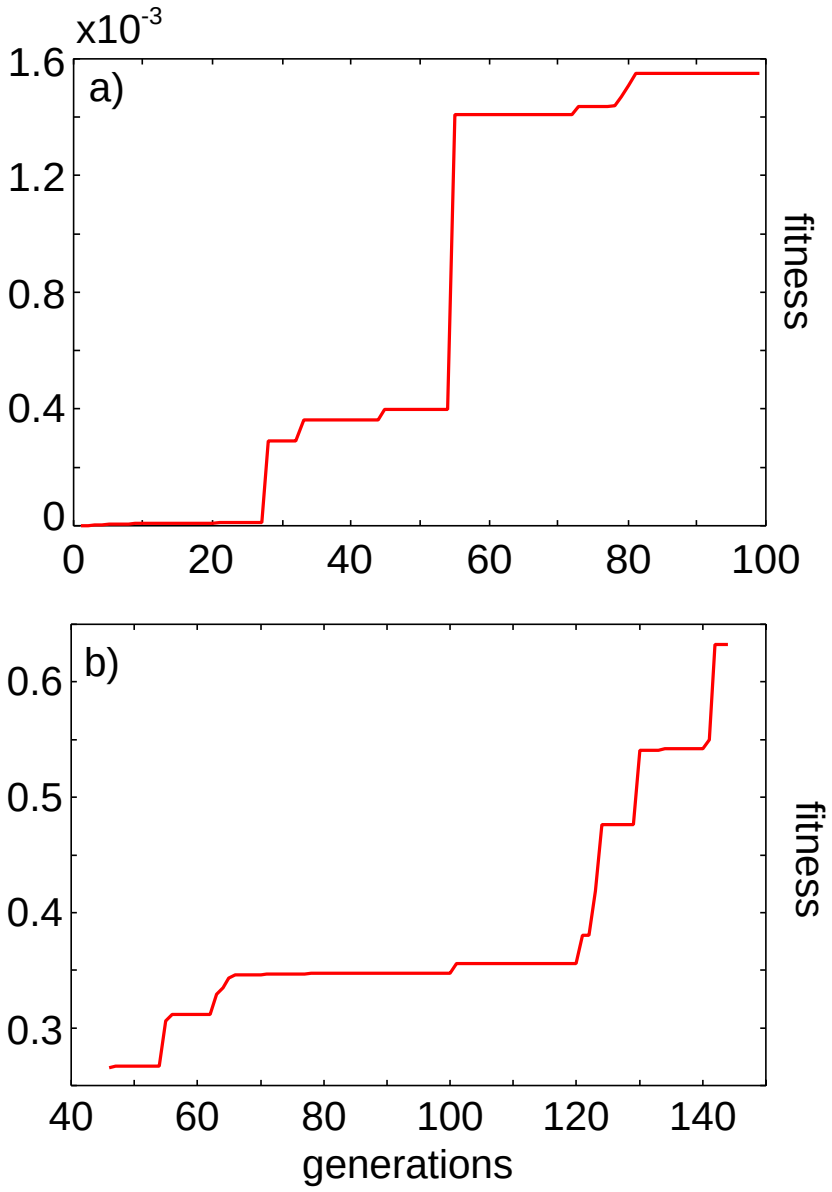

Figure 3.44: Trying the GA for a 2d potential with a low frequency mode ($120\,\mathrm{cm}^{-1}$) results in a potential, in which the algorithm cannot target a single level efficiently, as the density of states gets too high. This can be seen in panel **a)**, where the efficiency is the population of the ground state in the target well. For this one can set the efficiency to a sum of level populations. In panel **b)**, the total efficiency, resulting from the sum over all levels in the target well below the barrier is plotted.

get a good coupling to the laser field. For a proton transfer reaction, the main change of the dipole happens for the movement of the hydrogen along the reaction coordinate. The small movements of the scaffold do not induce a strong change in the dipole. Nevertheless, there is still the possibility to transfer oscillator strength to the normal modes via a direct mode coupling.

Conclusion

Extensive studies of the efficiency of the application of GA to laser control in one and two dimensional models have been made in this section. The conclusions one can draw from this show a limited range of applications for the usage of GA to search for optimal laser pulses. For the calculations made for the 1d model system, the algorithms manage to create good control fields, which could reproduce, and sometimes improve, the reaction pathway used by the analytical pulses. These results can be generated without any previous assumptions for the pulse parameters, as long as the target state is "easily" reached, i.e. the quality value of an individual is significantly different from zero, even if the optimal set of parameters has not be reached. This allows the recombination part of the GA to slowly increase the efficiency of such individuals. If the potential gets more complicated and the reaction path necessary is more complex, this is no longer given. In this case the quality surface is mostly a plane at zero efficiency, with very narrow spikes of better values at some parameters. Before the random mutations of the GA do not generate at least one individual on one of these peaks, the search is more or less completely random. With increasing size of the parameter space one needs bigger population sizes or a much larger number of generations to reliably find a good set of parameters for an individual. This is already apparent for the model systems with higher barrier and becomes obvious for the two dimensional potentials. In these systems, more and more iterations produce an ever smaller increase in efficiency of the final pulse. This is probably partly due to the rather limiting parametrization of the laser field into three simple $\sin^2$–pulses, reducing the flexibility of the laser, as only three distinct frequency components are available. This can be overcome by using a more variable parametrization of the pulse, e.g. using an approach simulating the effect of a pulse shaper [37], as mentioned at the beginning of this section. On the other hand, one has to see, that already the 12 available parameters represent an extremely large parameter space, which can be searched for long time without hitting the "correct" peak on the quality surface to climb (cf. Fig. 3.35).

The other main difficulty starting to appear with the 2d calculations, is again the limited power of the computers. The main requirements of a GA is large number of generations, to reach a good overall fitness of the population, and a population large enough to sample enough of the available parameter-space at once. To evaluate the fitness of an individual, a complete quantum mechanical propagation of the system is necessary. While this takes only several seconds for the 1d systems, it takes in the worst case up to half an hour to do this for the 2d system. The GA method applied requires around 10 individuals per

	1. pulse				2. pulse				3. pulse			
	t_i [au]	t_f [au]	$\mathcal{E}_0$ $[E_h/ea_B]$	ω_0 $[E_h/\hbar]$	t_i [au]	t_f [au]	$\mathcal{E}_0$ $[E_h/ea_B]$	ω_0 $[E_h/\hbar]$	t_i [au]	t_f [au]	$\mathcal{E}_0$ $[E_h/ea_B]$	ω_0 $[E_h/\hbar]$
Fig. 3.30	1914	32640	$0.12 \cdot 10^{-02}$	$0.85 \cdot 10^{-03}$	5040	25000	$0.30 \cdot 10^{-02}$	$0.44 \cdot 10^{-02}$	–	–	–	–
Fig. 3.32	4993	22390	$0.28 \cdot 10^{-02}$	$0.43 \cdot 10^{-02}$	851	39750	$0.14 \cdot 10^{-02}$	$0.35 \cdot 10^{-02}$	–	–	–	–
Fig. 3.33	442	29990	$0.69 \cdot 10^{-03}$	$0.24 \cdot 10^{-04}$	3	19970	$0.30 \cdot 10^{-02}$	$0.42 \cdot 10^{-02}$	–	–	–	–
Fig. 3.34	4807	39980	$0.30 \cdot 10^{-02}$	$0.84 \cdot 10^{-02}$	41	39850	$0.30 \cdot 10^{-02}$	$0.92 \cdot 10^{-02}$	–	–	–	–
Fig. 3.35	78	3134	$0.25 \cdot 10^{-02}$	$0.19 \cdot 10^{-01}$	10040	39810	$0.30 \cdot 10^{-02}$	$0.89 \cdot 10^{-02}$	7411	20930	$0.30 \cdot 10^{-02}$	$0.94 \cdot 10^{-02}$
Fig. 3.36	263	39920	$0.28 \cdot 10^{-02}$	$0.96 \cdot 10^{-02}$	7224	32340	$0.18 \cdot 10^{-02}$	$0.78 \cdot 10^{-03}$	1083	37480	$0.27 \cdot 10^{-02}$	$0.81 \cdot 10^{-02}$
Fig. 3.37	108	36200	$0.30 \cdot 10^{-02}$	$0.96 \cdot 10^{-02}$	4724	28240	$0.27 \cdot 10^{-02}$	$0.88 \cdot 10^{-02}$	1999	37780	$0.27 \cdot 10^{-02}$	$0.81 \cdot 10^{-02}$
Fig. 3.39	3702	27270	$0.30 \cdot 10^{-02}$	$0.94 \cdot 10^{-02}$	3254	30160	$0.24 \cdot 10^{-02}$	$0.76 \cdot 10^{-02}$	85	33310	$0.30 \cdot 10^{-02}$	$0.11 \cdot 10^{-01}$
Fig. 3.43	21690	28370	$0.37 \cdot 10^{-02}$	$0.82 \cdot 10^{-02}$	1661	39630	$0.50 \cdot 10^{-02}$	$0.39 \cdot 10^{-02}$	829	32420	$0.50 \cdot 10^{-02}$	$0.11 \cdot 10^{-01}$

Table 3.2: The pules parameters of the laser fields generated by the gentic algorithm for the different model systems. All values are given in atomic units.

generation and takes at least 100 generations to produce a relatively stable result. Both the population and the number of generations are better larger than smaller. So a single run requires at least 1000 evaluation of the quantum system, i.e. approximately 500 CPU hours on an Origin3000 computer (R14000 CPUs) for the largest 2d model studied. Additionally, with a large parameter space, it is quite likely, that 100 generations are far from enough to find a satisfying result.

One of the smaller drawbacks is, that as long as one has not found an individual with a perfect fitness, one can never be sure if the GA is finally converged to the best individual available in the parameter space. Even after several generations producing no change, it is possible to have a random mutation move to a better spot on the quality surface.

Even with these limitations, the application of GAs can be useful. The first criteria is the time it takes to evaluate the quality of the system. If this is fast enough (always depending on the computer resources available), it should be no problem to use a GA to find an optimal control pulse. An other application would be the optimization of a parameter set, which is only known approximately. This situation would allow to narrow down the available parameter space sufficiently, so that only few generations of a small population are necessary to produce an optimized result.

One should also note, that the structure of the GA allows the very efficient application of parallel computers, as the quality of each individual of a generation is completely independent of each other. Therefore the time consuming quantum propagations necessary for this evaluation can be spread to several processors, without needing complicated data transfer.

As points for future work, the introduction of a more flexible laser pulse (e.g. one where a large number of Fourier components is used as parameters, as it would be produced by a pulse shaper) is probably the most interesting. Another area would be a more elaborate definition of the quality function, beyond the simple population of eigenstates, as already shown in Fig. 3.44. For instance, one could try to define the quality of a control pulse via a functional similar to the one used in the inverse tracking algorithm (Eq. (2.153) in Section 2.5.4), which would allow to evaluate the total dynamics of the wavepacket with reference to some reaction path, in contrast to the simple evaluation at the end of the control time now.

3.2 Potential energy surface for the proton transfer in 8–hydroxyimidazo[1,2–α]pyridine

For the study of proton transfer (PT) reactions, it is desirable to move away from analytical model potentials, and use a surface generated only from quantum chemical *ab initio* data points. In this section the potential energy surface for the PT in 8–hydroxyimidazo[1,2–α]pyridine (HIP) is calculated using different quantum chemical methods. The molecule was first studied in the group of Douhal [132], where the energies of the stationary points

on a fully relaxed Hartree–Fock potential energy surface were calculated. The proton tranfer reaction in this system is of special interest due to the fact that it involves a charge separation, i.e. the two forms have a very different charge distribution and dipole moment. In addition, the molecular system has the advantage of having a planar, very rigid molecular scaffold, caused by the double ring structure, in contrast to other PT systems, like malonaldehyde, where the whole molecule is very floppy. These properties make the system interesting to study the effects of polar solvents on the PT process. In [132], calculations for both the S_0 and S_1 state show the presence of two tautomers (enol form and zwitterionic form). In S_0, the enol form is the most stable one, while in S_1 the zwitterionic one moves to the lowest energy. In both cases, the energy barrier is quite high. Adding water as a polar solvent then greatly reduces this barrier and stabilizes the zwitterionic structure.

The goal of the following *ab initio* calculations is to generate all the relevant parameters needed to build a dynamical model, enabling a dynamical simulation for the PT reaction in this molecule. In this section, the model is based on the calculation of an unrelaxed, two dimensional potential energy surface (as described in Section 2.2) for the in–plane motion of the proton within the HIP molecule. To this surface the harmonic normal modes of the molecule are added, to generate a Cartesian reaction surface (CRS), as given by Eq. (2.35).

The starting point for the generation of this 2d potential surface is the calculation of the most stable ground state geometries and the stationary points of the molecule. To identify the relevant coordinates for the PT reaction, the reactant and product configuration of the molecule, together with the transition state between the two, have to be calculated. To determine the level of quantum chemical theory and the size of the basis set necessary, in an initial step the fully relaxed geometries of HIP are compared for different methods. the tautomers (**E1**, **Z**) and the transition state (**TS1**), as discussed in [132], are calculated using the HF method, second–order Møller–Plesset perturbation theory (MP2), as well as density functional theory (DFT). For the latter method Becke's three parameter hybrid functional in combination with the Lee, Yang, and Parr correlation functional is used [78, 79]. Three basis sets have been considered to study the effect of polarization and diffuse functions on the hydrogen atoms, i.e. 6-31+G(d), 6-31+G(d,p), and 6-31++G(d,p). All calculations have been performed using the GAUSSIAN94 set of programs [133].

The 6-31G basis set is a so called split–valence set, using a single contracted Gaussian build from six primitive Gaussians for the inner shell atomic orbitals (see Section 2.1, page 14), and a linear combination of a CGTF from three primitive Gaussians and one with a single one (thus the notation 6-31G). The (d) denotes the addition of six d–type Cartesian Gaussian functions on all heavy atoms (Li – Ca), and the (p) of further three p–type polarization function on H and He atoms. The single + denotes a further addition of four diffuse functions (s, p_x, p_y, p_z) to all non–hydrogen atom. These diffuse terms have a very small orbital exponent, and are needed for accurate representation of long range interactions. The two plus signs (++) add a single diffuse s–type function to all hydrogens

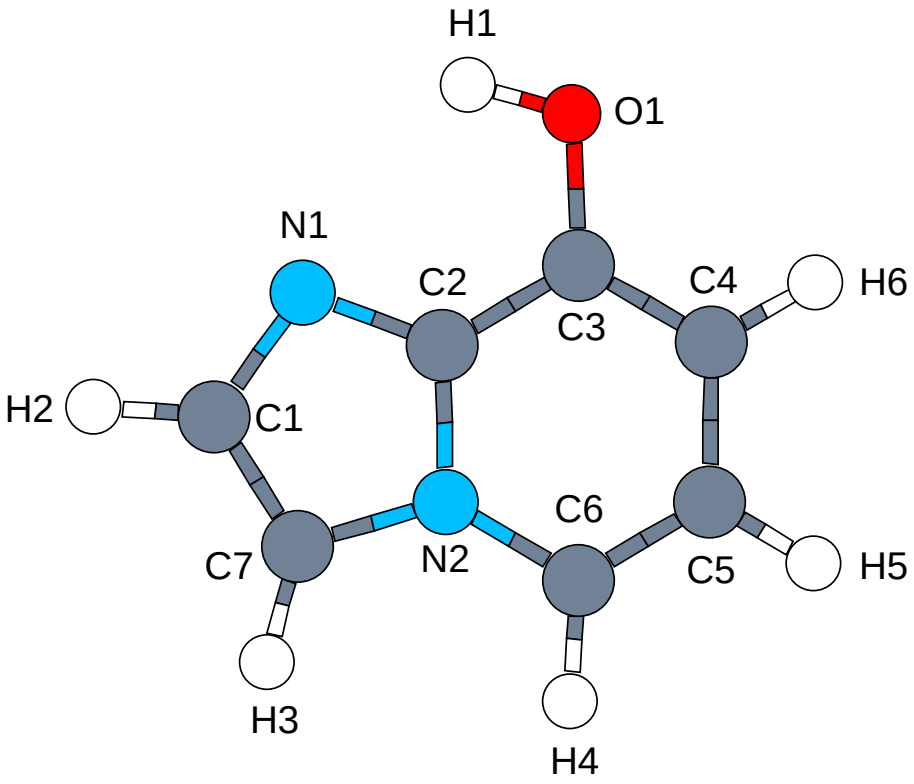

Figure 3.45: The most stable isomer (enol **E1**) of HIP ($C_7H_6N_2O$) as obtained from DFT/6-31+G(d,p) geometry optimization.

as well [134].

The results are compiled in Table 3.3. It is known that the inclusion of electronic correlation effects in the description of PT reactions can have a dramatic influence on the energies, in particular for the reaction barrier. This can be seen in Table 3.3 where the MP2 and DFT energies are compared with those obtained from HF theory [132]. Apparently, correlation effects decrease the HF energies by about 30%. One further notes, that in both the MP2 and DFT calculations the inclusion of diffuse functions on the hydrogen atom does not change the energies as much as for polarization functions. Finally, MP2 and DFT methods give for the same basis set comparable energies, in particular for the reaction barrier.

The optimized DFT geometry for the most stable tautomer (enol **E1**) is shown in Fig. 3.45. The DFT obtained here and the HF results found in Ref. [132] differ by at most 5% in the predicted bond lengths. In addition to the configurations **E1**, **TS1** (transition state), and **Z** (zwitterionic state) reported in Ref. [132], a further tautomer **E2** (enol) was found, corresponding to an in–plane rotation of the hydrogen atom around the oxygen (C3–O1–H1 bending). The distances between those atoms which are most affected by the PT

Method	Basis set	**TS1**	**Z**
HF	6-31+G(d)	0.06716	0.02306
	6-31+G(d,p)	0.06674	0.02545
	6-31++G(d,p)	0.06674	0.02545
B3LYP	6-31+G(d)	0.04576	0.01431
	6-31+G(d,p)	0.04537	0.01629
	6-31++G(d,p)	0.04537	0.01628
MP2	6-31+G(d)	0.04723	0.01717
	6-31+G(d,p)	0.04782	0.01946
	6-31++G(d,p)	0.04783	0.01947

Table 3.3: Comparison of energies using different methods and basis sets. Given are the energy differences (in Hartree) of the configurations with respect to the enol **E1** structure.

atoms	**E2**	**TS2**	**E1**	**TS1**	**Z**
C1-N1	1.36 [1.37]	1.36	1.37	1.37	1.37
N1-C2	1.33 [1.34]	1.33	1.33	1.33	1.36
C2-C3	1.43 [1.41]	1.43	1.42	1.42	1.45
C3-C4	1.38 [1.36]	1.38	1.38	1.40	1.43
N1-H1	3.85	3.51	2.37	1.23	1.01
N1-O1	2.89	2.91	2.89	2.42	2.88
C3-O1	1.36 [1.35]	1.32	1.35	1.30	1.26
O1-H1	0.97	0.94	0.97	1.43	2.66

Table 3.4: Distances (in Å) between atoms at the different stationary points and transitions states. The available experimental values for the **E2** structure are given in square bracket [135]. For labeling see Fig. 3.45.

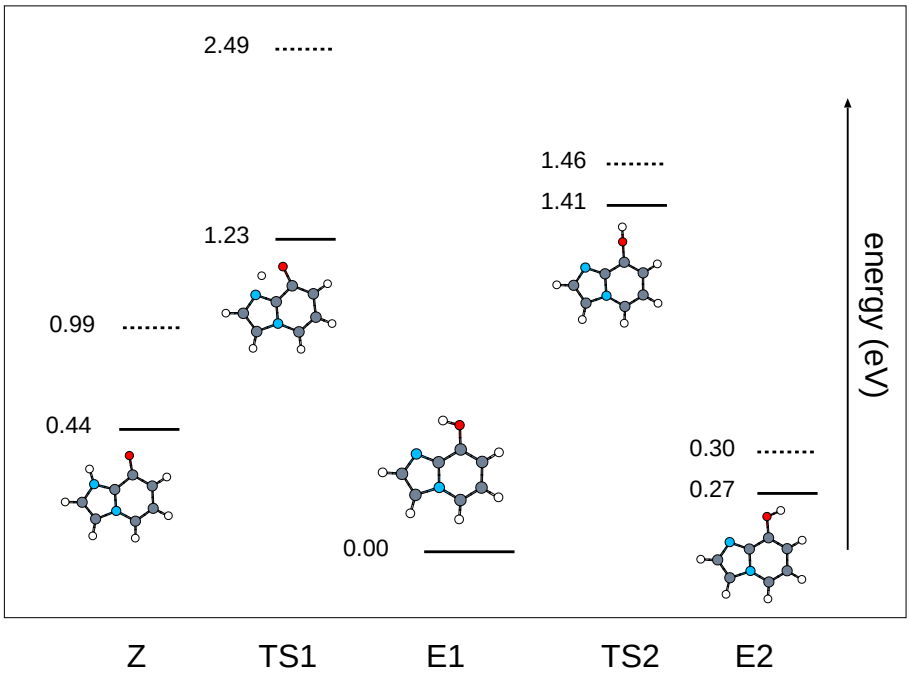

Figure 3.46: Energies (in eV) for the stationary points as well as the transition states obtained for the fully relaxed geometry optimization (solid) and the fixed substrate calculation (dotted).

are given in Table 3.4 for all tautomers. The only available experimental data are for the **E2** structure [135]. Even though the latter have been obtained for crystallized HIP, where the H1 atom forms an intermolecular hydrogen bond with the N1 atom of some other molecule, the bond lengths for the heavy atoms are in good agreement. The transition state, **TS2**, is found for a C3–O1–H1 bending angle of about 180°. The energetics of these five configurations is shown in Fig. 3.46 (solid lines).

One can see, that the barrier separating **E1** from **Z** is lower than that for the rotation to **E2**. However, **E2** appears to be more stable than **Z**. Nevertheless, at room temperature there should be only a negligible probability for finding any other tautomer than **E1**. Notice, that this situation might change in solution. For example, under neutral aqueous conditions the zwitterionic structure appears to be favored [135].

In order to characterize the stationary points and the transition states a normal mode analysis was performed. It has frequently been pointed out [124], that the low frequency vibrations of the scaffold can have a strong influence on the PT. For instance, in the simplest picture a O1–C3–C2 bending type of motion which reduces the PT distance might promote PT. Table 3.5 gives all normal modes frequencies below $1000\,\mathrm{cm}^{-1}$ for **E1** and **Z**. Those modes which effectively modify the PT distance are characterized with respect to being of stretch or bend type. One can see that, upon moving from **E1** to **Z**, the changes of the

mode	ω (**E1**)		ω (**Z**)	
1	187	[O1-C3-C2-b]	168	[O1-C3-C2-b]
2	208		190	
3	272	[O1-C3-s + O1-C3-C2-b]	273	[O1-C3-s + H1-N1-s]
4	280		284	
5	494		496	
6	503	[H1-O1-s]	521	
7	527		525	[H1-N1-C2-b]
8	556	[H1-O1-s]	547	[H1-N1-C2-b]
9	590		597	[H1-N1-C2-b + O1-C3-C2-b]
10	621		609	[O1-C3-s]
11	641		641	
12	698		658	[H1-N1-C2-b]
13	702		702	
14	731		713	
15	759		738	
16	860		831	
17	885		839	
18	885		883	
19	926		938	
20	938		955	
26	1250		1240	
42	3730		3750	

Table 3.5: Normal mode frequencies (in cm^{-1}) on the fully relaxed potential surface (below 1000 cm^{-1}) calculated with the DFT/B3LYP method. For those modes which are likely to influence the PT a tentative assignment is given, based on the type of motion of the O1 or H1: X-Y-s denotes a stretching vibration of the bond X-Y and X-Y-Z-b a bending motion with respect to the angle enclosed by X-Y-Z. In these modes, there are always other bonds moving as well. The last two lines give the modes closest to the "pure" O1–H1 (or N1–H1) bending and stretching modes.

scaffold related normal mode frequencies are rather small. This indicates that in terms of the reactant and product configurations the scaffold is only weakly affected by the PT. In this respect HIP is rather different from more flexible molecules.

3.2.1 A Cartesian Reaction Surface for HIP

To develop the potential in the CRS formalism, one has to select suitable Cartesian reaction coordinates, which describe the dynamics of the molecular system during the PT process.

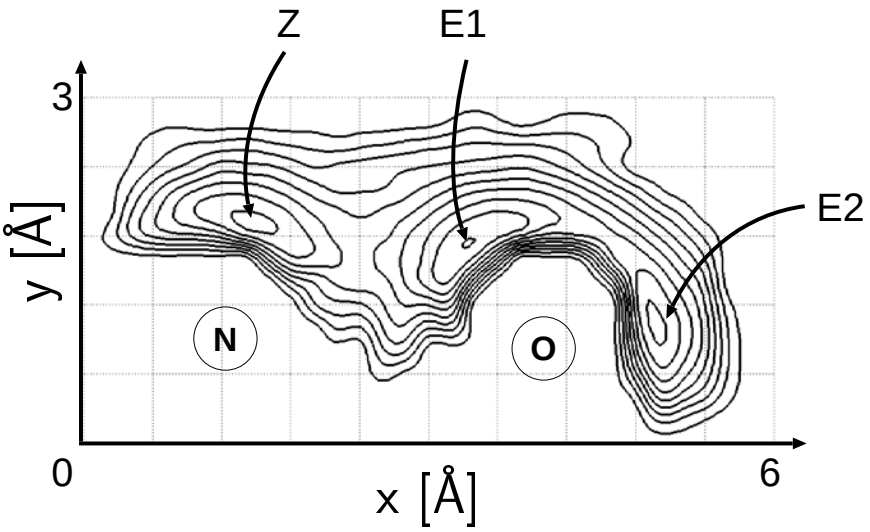

Figure 3.47: Two dimensional PES for the PT reaction in HIP. Each contour line equals 0.015 E_h, starting from zero energy at the **E1** geometry.

As can be seen from the calculations of the reactant and product geometries, the only large amplitude motion during the transfer is the in–plane movement of the hydrogen, the molecular scaffold stays nearly unchanged for both configurations. In the following, the in–plane coordinates of the proton is called x and y and the coordinate system is chosen such that the x–axis points along the vector connecting the nitrogen (N1) with the oxygen (O1) atom as labeled in Fig. 3.45. The z–coordinate of the hydrogen atom is neglected. The substrate therefore includes $3N_{\mathrm{nuc}} - 3$ degrees of freedom denoted $\mathbf{R}$, following the notation from Section 2.2, Eq. (2.35). The reference geometry, $\mathbf{R}^{(0)}$, for expansion of the substrate potential energy is set to correspond to the most stable configuration, **E1**, shown in Fig. 3.45.

The next step is the calculation of the reference potential surface, $V(x, y, \mathbf{R}^{(0)})$, for this fixed molecular geometry. For this, only the hydrogen is moved with respect to the frozen molecular scaffold, and for the resulting configurations single point DFT calculations with GAUSSIAN94 are performed, to find the corresponding potential energy. The potential, resulting from a 2d–spline fit to the calculated points, is presented in Fig. 3.47. To reach a good fit, without artificial secondary minima, which can be generated from fits to a set of too sparse points, 193 grid points had to be calculated in the region of interest. As expected from the topology of the fully relaxed PES, $V(x, y, \mathbf{R}^{(0)})$ has three minima corresponding to the **E1**, **E2**, and **Z** configuration. The energies at these points as well as at the transition states are given in Fig. 3.46 (dotted lines). Since the substrate is frozen all energies are higher than for the fully relaxed PES. However, in contrast to the latter the barrier at **TS1** is now higher than that at **TS2**. Also the energy of the **Z** tautomer has increased much stronger than that for the **E2** tautomer. Already at this point one can

mode	ω(**E1**)	ω(**TS1**)	Δ_n (**TS1**)	ω(**Z**)	Δ_n (**Z**)
1	208	189	0.00	121	0.00
2	257	244	0.00	204	0.00
3	322	310	0.00	308	0.00
4	469	326	**41.50**	392	0.49
5	496	465	0.00	496	0.18
6	540	504	0.33	543	0.00
7	554	537	0.05	551	0.09
8	572	550	0.00	572	0.00
9	646	611	1.54	633	0.00
10	674	630	0.00	655	0.54
11	830	664	0.06	675	0.00
12	868	835	0.13	710	0.08
13	898	855	0.00	711	0.00
14	916	912	0.02	743	0.00
15	959	956	0.00	838	0.00
17	1111	1104	0.05	882	1.24
19	1174	1172	0.00	1051	4.62
22	1311	1311	0.00	1134	**5.76**
23	1319	1319	0.20	1185	1.70
24	1357	1357	0.00	1231	1.49
31	1834	1832	0.03	1547	2.42
$\sum_n \Delta_n$			43.91		18.61

Table 3.6: Normal mode frequencies (in cm^{-1}) and reorganization energies (in mHartree) on the CRS. Besides the low frequency ($< 1000\,\mathrm{cm}^{-1}$) part of the spectrum those high frequency modes are listed, which have highest reorganization energy in the **Z** configuration. In the **E1** configuration the reorganization energies are identical to zero.

therefore conclude that the force exerted on the substrate normal modes is much stronger when going from **E1** to **Z** on the CRS.

In the next step, the normal modes of the molecular scaffold, without the moving proton, are calculated. In this section, only the normal modes at the stationary points are examined, to get an idea about the dynamics of the scaffold at these points. Table 3.6 lists the frequencies as well as the reorganization energies for those modes which are appreciably coupled to the PT at **TS1** and **Z** together with the $< 1000\,\mathrm{cm}^{-1}$ modes at the equilibrium configuration, **E1**. The reorganization energies are calculated from Eq. (2.40). One first notes, that the CRS normal mode frequencies differ from those of the fully relaxed surface. This was to be expected, since the Hessian matrix has been diagonalized for the substrate

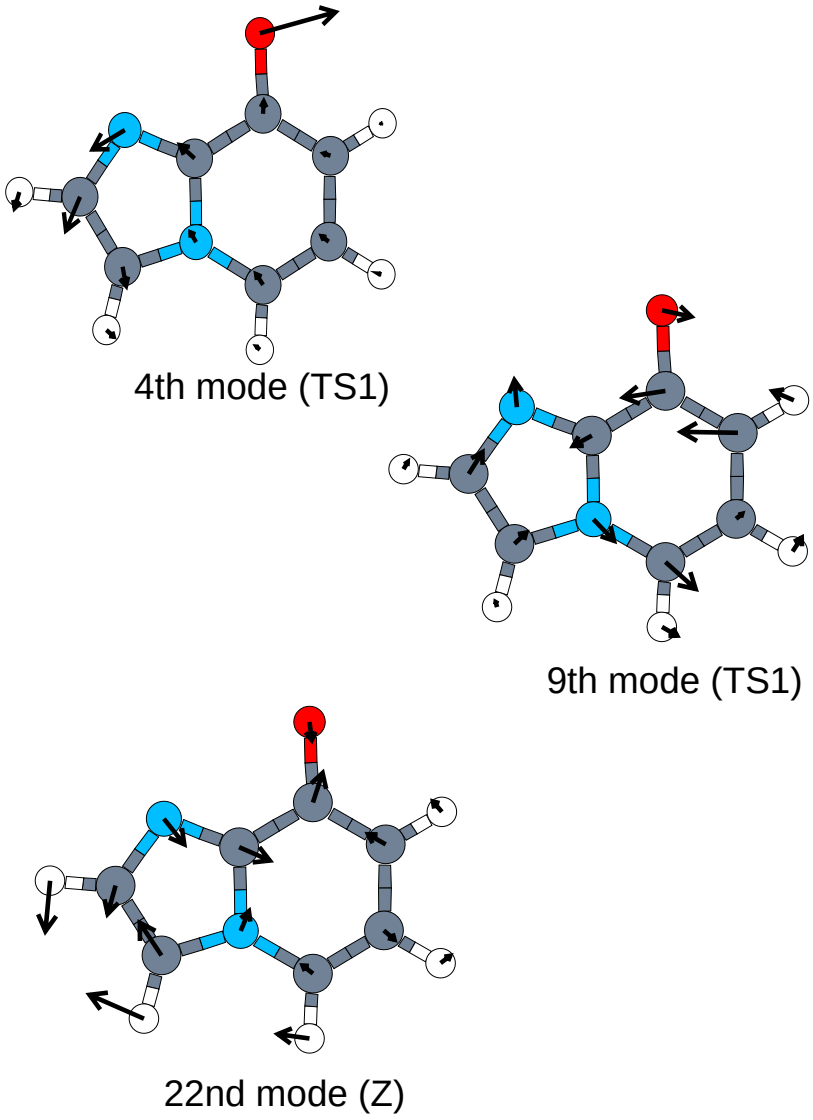

Figure 3.48: The substrate normal modes coupled most strongly to the proton motion at the transition state (**TS1**) and in the zwitterionic (**Z**) configuration.

atoms only. Therefore, the character of the normal modes is likely to be different as well. However, in particular high frequency modes involving the C–H stretching vibrations of the scaffold are almost not affected by this reduction. At the **TS1** state, the reorganization energy for the $n = 4$ mode is by far the largest, i.e. it is most strongly coupled to the PT. In Fig. 3.48 the displacement vectors along this normal coordinate are plotted. As expected this mode is of C2–C3–O1 bending type. This is in accord with the **TS1** relaxed geometry where the O1–N1 distance is 2.42 Å as compared to 2.89 Å at **E1**. There is a second mode at $611\,\mathrm{cm}^{-1}$ which also couples appreciably to the PT. It involves the motion of the pyridine and imidazole rings in a way that the PT distance is modified in agreement with the findings reported in [132]. The sum of all the displacement energies gives a hint for the validity of the harmonic approximation. The energy of the completely relaxed surface plus this total reorganization energy should result in the energy of the unrelaxed surface. Looking at the values, this is in good agreement with the calculated values. At the transition state **TS1** the difference between the two potentials is 1.26 eV, the sum of the reorganization energies is $\sum_n \Delta_n = 1.2\,\mathrm{eV}$. In the zwitterionic configuration **Z**, the potential difference is 0.55 eV, the reorganization energies are $\sum_n \Delta_n = 0.51\,\mathrm{eV}$. So even for the transition state, where the O1 atom is significantly displaced from its equilibrium position the harmonic approximation is still valid. Therefore one can safely use only a single reference geometry for the potential, a flexible reference it not necessary.

In the **Z** configuration the coupling to the two modes mentioned above is drastically reduced. With the O1–N1 distance returning to 2.88 Å on the relaxed surface this is not surprising. In other words, with the proton moving away from its **E1** binding site its influence on the local vibrations there decreases. However, the relaxed geometry of the whole scaffold is different in **E1** and **Z**. This is reflected in the appearance of couplings to modes involving mostly motions of the ring atoms. In Fig. 3.48 the $n = 22$ mode is shown as an example. One can also see, that the vibrational frequencies are depending on the reaction coordinates. This is most clearly shown for the $n = 4$ mode, whose frequency decreases when moving to the **Z** structure.

For the reaction path moving to the **E2** configuration, the picture is not so clear. In this direction, no dominant normal mode was found. Instead, a multitude of modes was distorted with comparable reorganization energy. This also is not very surprising, as, in contrast to the PT from **E1** to **Z**, this movement is a simple rotation of the hydrogen and does not require the breaking and forming of bonds. One can also see in Fig. 3.46, that the total reorganization energy of the **E2** configuration is rather small, compared to the other stationary points.

3.2.2 Laser Control Scenarios

After the calculation of the basic requirements of a CRS Hamiltonian for the PT reaction in HIP, now a closer look is taken at the applicability of different control schemes to this reaction. In Ref. [125] rather general requirements on controllable PT systems have

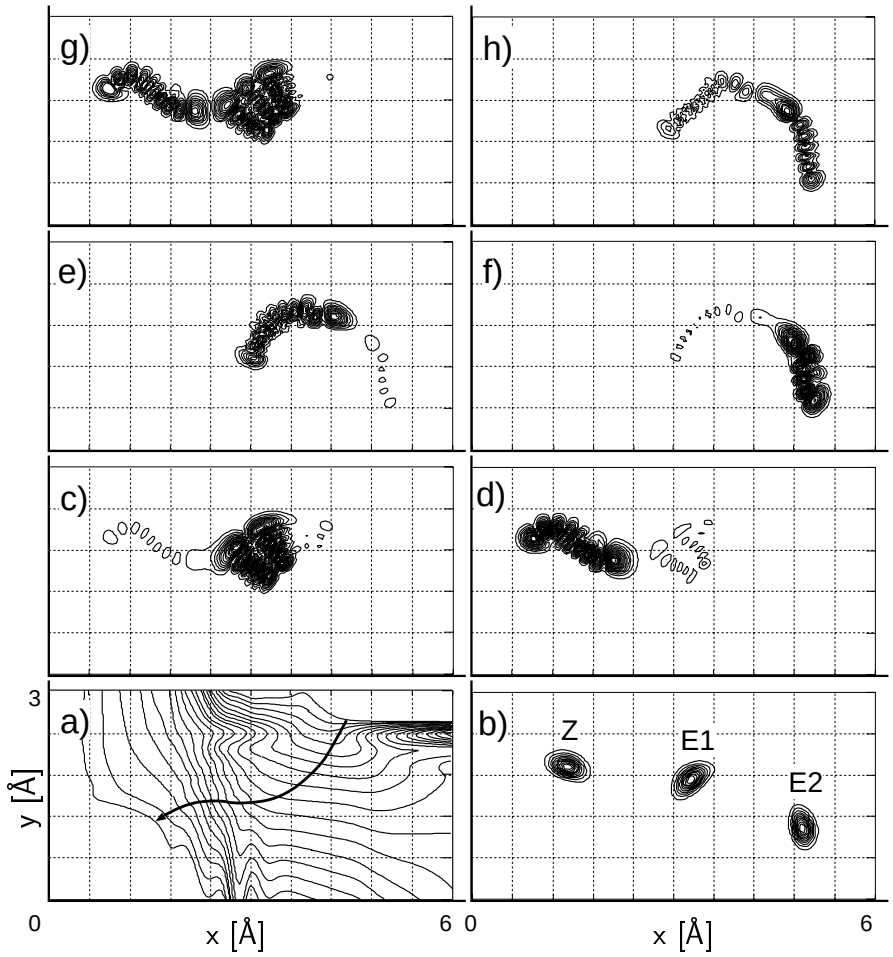

Figure 3.49: In a) the dipole surface of the system calculated in the HF approximation is shown. Each contour line equals 0.5 D, starting at zero and increasing in the direction of the arrow. In b)–h) the eigenfunctions of the bare PT Hamiltonian which are suitable for reaction control are plotted (cf. 3.2.1). In b) the three lowest energy states in the respective geometries are shown. Pictures c) and d) give the tunneling pair φ_{91} and φ_{92} suitable for the tunneling transfer from **E1** to **Z**. In e) and f) an equivalent pair (φ_{33} and φ_{34}) for the tunneling from **E1** to **E2** can be seen. Finally g) gives a delocalized state (φ_{106}) for a pump–dump type of transfer from **E1** to **Z** and h) a similar state (φ_{40}) for this type of transfer from **E1** to **E2**.

been formulated. These are first checked for the fixed substrate, to see if the modeling of the system can be handled by the proposed methods. One of the most important points, namely the clear distinction between reactant and product states, is certainly fulfilled. To demonstrate this, in Fig. 3.49 the wavefunctions for the energetically lowest vibrational states in **E1**, **E2**, and **Z** are shown. The diagonalization of the two–dimensional system Hamiltonian has been performed by the Fourier grid method, discussed in [99] and Appendix A.2. In the following the eigenenergies and eigenfunctions are denoted E_n and φ_n ($n = 0, 1, 2, \ldots$), respectively. Starting from the **E1** vibrational ground state, φ_0, the ultimate target states for isomerization control are the lowest vibrational states in **E2** (φ_5) and **Z** (φ_{17}). In practice, however, most of the vibrationally excited states in the **E2** and **Z** configurations, which have energies well below the barrier are rather localized, i.e. they can be considered as good target states as well. The approach using the eigenfunctions in the potential for the frozen substrate is used here, as the process one is interested in is supposed to happen very fast. Therefore one can keep the scaffold of the molecule fixed and use a "sudden switching approximation" to analyze the possible laser control scenarios.

The success of laser control depends on how efficient the external field can interact with the molecule. Within the semi-classical dipole approximation the value of the system's dipole moment is the decisive quantity in this respect. The dipole moment surface along the reaction coordinates, $\mu(x, y)$, has been determined within the DFT *ab initio* calculations on the level of Hartree–Fock theory. The result is shown in Fig. 3.49. As expected the variation of the dipole moment between the **E1** and the **Z** configuration is rather large (5.3 D in the fixed geometry; for relaxed geometry values, see [132]). The change of the dipole moment between the **E1** and **E2** structures is only 1.3 D. In the vicinity of the initial **E1** configuration the gradient of the total dipole moment is $\partial\mu/\partial x = 0.91\,\mathrm{D/\AA}$ and $\partial\mu/\partial y = 1.93\,\mathrm{D/\AA}$.

The tunneling approach to PT control, proposed in Ref. [126] and examined closer for the low barrier model case in Section 3.1.1 of this work, seems to be no good choice for this potential. For this model, one has to apply a constant external field to the molecule. Its amplitude is chosen such that the two lowest vibrational states on the reactant and product side of the barrier are tuned in resonance. The dynamics of the localized superposition of eigenstates created by the laser pulse then leads to tunneling. The time scale for this process is given by the coupling between the two lowest states in a localized basis or by the tunnel splitting in a delocalized basis. In view of the high barrier separating **E1** from **E2** and **Z** in HIP this coupling is extremely small and tunneling takes an extremely long time. Therefore the simple tunneling approach seems to be not appropriate for realizing laser control of ultrafast PT in HIP.

For cases with higher barrier, it has been proposed in Section 3.1.1 and in [127], to combine the tunneling pulse with a second, vibrational state selective pulse which excites the system in the reactant configuration. This requires the availability of a vibrationally excited state which is energetically close to the top of the barrier but still localized in the

reactant well. In addition, to have efficient tunneling there should be a rather localized vibrationally excited state on the product side which is close in energy to the excited reactant state. In Fig. 3.49 the wavefunctions for the vibrationally excited states φ_{91} and φ_{92} are shown, which would be suitable for the PT from **E1** to **Z** using this scheme. The transition energy from the ground state to φ_{91} is 2.07 eV. In order to estimate the pulse parameters necessary for a direct excitation of this state, one has to consider only the population inversion between the two states, $\varphi_0 \rightarrow \varphi_{91}$. Thus any simultaneous excitation of the neighboring excited states is neglected in the following estimates. This assumption is reasonable if the spectral overlap of the pulse with the neighboring states is small. Further, the laser field shall be switched on during the interval $0 \leq t \leq T$ with the assumed form $\mathcal{E}(t) = \mathcal{E}_0 \cos(\omega_L t) \sin^2(t\pi/T)$. For these pulses, the area theorem [136] states, that for resonant excitation the population inversion between these two states is obtained if the pulse area, defined as

$$A = \frac{\mu_{mn}}{\hbar} \int_0^T dt' \, \mathcal{E}(t') = \frac{\mu_{mn} \mathcal{E}_0 T}{2\hbar} \tag{3.17}$$

is equal to π. Here, μ_{mn} is the transition dipole moment matrix element between the two considered states. For the present case $\mu_{0,91} = 2.62 \cdot 10^{-4}$ D which would require $\mathcal{E}_0 = 1.47 E_h/ea_0$ for $T = 1$ ps. Provided the state φ_{91} has been populated, the second step of this control scheme, i.e. the tunneling, is initiated. The detuning between the energy levels corresponding to the wavefunctions shown in Fig. 3.49 is $E_{92} - E_{91} = 9$ meV. The constant field, $\mathcal{E}_\mathrm{p}$, necessary for triggering the complete population inversion follows from $\mathcal{E}_\mathrm{p} = (E_n - E_m)/(\mu_{nn} - \mu_{mm})$ (from Eq. (3.4)), which in the present case is equal to $4.9 \cdot 10^{-4} \, E_h/ea_0$. The tunneling time would be $\tau = h/4|\mu_{mn}|\mathcal{E}_\mathrm{p} = 939$ fs [127].

Alternatively to these *through–barrier* control schemes one can explore the possibility of an above barrier two–pulse pump–dump mechanism as put forward, e.g, in Refs. [125, 137]. Here it is required that, starting from the localized reactant state a delocalized intermediate state can be excited by the pump–pulse. The dump–pulse then induces a transition from this intermediate to some final localized product state. In Fig. 3.49 suitable delocalized states for the pump–dump control of the **E1** to **Z** (φ_{106}) and **E1** to **E2** (φ_{40}) reaction are plotted. The former pathway requires a pump–pulse having $\hbar\omega_\mathrm{L} = E_{106} - E_0 = 2.19$ eV and $\mathcal{E}_0 = 2.33 \, E_h/ea_0$ for population inversion ($T = 1$ ps). The pulse parameters for excitation of φ_{40} are $\hbar\omega_\mathrm{L} = E_{40} - E_0 = 1.44$ eV and $\mathcal{E}_0 = 1.65 \, E_h/ea_0$.

The energies needed for this ground state excitation is already a significant part of the energy difference to the electronically excited state S_1, which is located approximately 6.5 eV above the ground state S_0, as reported in [132].

Looking at the possibility of laser control from this eigenstate point of view, it should in principle be possible to use either the pump–dump or the combined pump and tunnel scheme to control the PT in HIP. The main requirements – namely the presence of well separated reactant and product states and an energy difference between all possible products – are met. Therefore state selective control via the laser frequency should be possible, i.e. one should be able to induce the molecule either to a rotation of the O–H bond into

E2 or transfer the proton to the **Z** configuration by breaking this bond.

Unfortunately, this simple approach does not work for the HIP molecule. The problem becomes obvious, by looking at the amplitude of the electrical field required to reach the vibrational states needed for the transfer process. Due to the smallness of the transition dipole matrix elements for the high overtone transitions, a complete population inversion requires in all cases field intensities above $10^{16}\,\mathrm{W/cm^2}$. This is of course far beyond the energy which can be expected to ionize the molecule. Even the numerical simulations cannot handle fields with this amplitude, as the potential gets distorted well beyond reasonable limits. This prohibits a completion of the transfer process in the enforced time limit of 1 ps per pulse. Simply increasing this time significantly, to reduce the electrical field required, was not considered as a suitable solution of this problem, as the control process has to be faster than the effects of dissipation and IVR. While an isolated two-atomic system might be controllable by using pulses of several 100 ps length, a molecule coupled to the environment or containing couplings to molecular scaffold modes simply distributes the incoming energy evenly to all degrees of freedom. A direct excitation of the desired eigenstates is therefore not realistic. An alternative can be provided by vibrational ladder climbing. Possible scenarios include the multi–pulse, multi–photon scheme as put forward in Ref. [112], for instance, or the use of chirped pulses [138]. For example, the complete population inversion of the transition to the first excited vibrational state of the **E1** structure would require a 1 ps pulse having an intensity of only $0.6 \cdot 10^{12}\,\mathrm{W/cm^2}$. Due to the number of levels to be climbed, this again is unrealistic due to the time required, if dissipative effects are to be included.

Looking at the stationary IR spectrum of HIP calculated for the 2d potential surfaces, one sees that only the O–H stretch vibration is significantly excited with the calculated dipol moment. The O–H bending mode is not visible.

So far the influence of the orthogonal substrate modes has not been included into the calculations. From the results discussed above, it is clear that a simple two–dimensional description of the PT in HIP is not sufficient. Any simulation of the sub-picosecond dynamics should at least include the $n = 4$ mode which modifies the PT distance and therefore reduces the reaction barrier. While normally any coupling to other molecular degrees of freedom is not desirable, as it leads to the distribution of the laser energy via IVR, this mode could actually help the transfer, since it effectively reduces the barrier. In order to estimate the possibility of a direct excitation of the $n = 4$ substrate mode, the gradient of the total dipole along the Q_4 normal mode in the **E1** configuration has been calculated. In linear approximation, a value of $\mu(Q_4) = 0.021 Q_4$ was found. The rather small gradient shows, that a control scheme building on a direct excitation of this promoting mode might not lead to a very efficient isomerization.

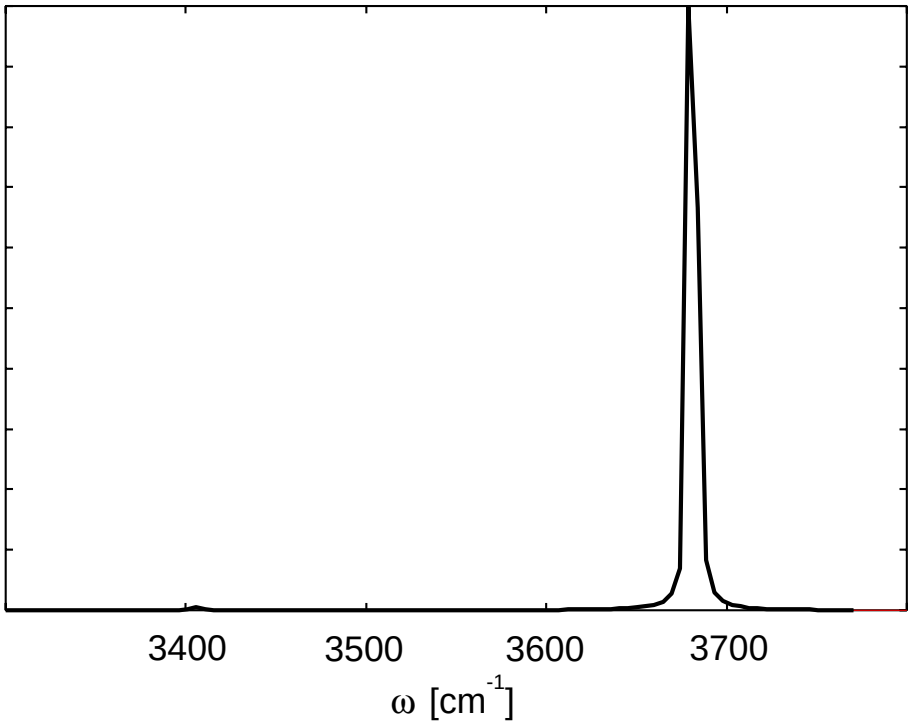

Figure 3.50: The stationary IR spectrum of HIP (IR spectra and linshapes are discussed in more detail in Section 3.3.1). One sees only a single line at the frequency close to the O–H vibrational band. The other mode, which could be observed in this 2d model (i.e. the bending mode of the hydrogen), is not visible for the calculated potential and dipol moment.

3.2.3 Conclusion

In this section, the necessary steps to develop a CRS Hamiltonian using *ab initio* data for the PT in a real molecular system have been implemented for the HIP molecule. The CRS was build for two Cartesian coordinates, allowing the proton to move freely in the molecular plane and including all other vibrations of the molecular scaffold within the harmonic normal mode approximation. One could see, that, as far as it concerns the PT, there are three relevant tautomers. The more interesting PT pathway leads to the zwitterionic state. This reaction has a significant coupling to a normal mode of C2–C3–O1 bending type, while moving from the enol to the transition state configuration. During these calculations, checks for the applicability of different control strategies for this system were made in the frozen substrate approximation. From these, it was found that the organization of the eigenstates would allow on first glance an isomerization control both with the pump–dump as well as with the combined pump–tunnel scheme. However, the highly excited vibrational states needed for the implementation of these schemes require

such intense external fields to populate, that an implementation of these methods is not possible. An efficient control with lower intensity lasers on the other hand, requires too much time to allow the use of a fixed molecular scaffold. At the same time, one sees that for this system the approximation of a frozen substrate is quite good, as only a few heavy atom modes are coupled to the hydrogen motion, which would not be excited by a short pulse.

For the future treatment of the PT in the HIP molecule, one can see that at least the scaffold mode representing the C2–C3–O1 bending has to be included in the dynamics of the proton. If more modes are included, the system should be well suited for the study of IVR processes, as only few modes couple to the hydrogen. For a complete analysis of the IVR processes in the CRS aproach, it is necessary to calculate the full second derivatives matrix $\mathbf{K}(x, y)$, at least in the vincinity of the **E1** configuration. As these matices require the same effort as a frequency analysis to calculate, the generation of the complete CRS surface entails an enourmous amount of computational work. The high vibrational levels required for the transfer in the frozen substrate approximation also show, that a transfer only in the ground state is a difficult proposition. If one does not want to move via an excited electronic state, vibrational ladder–climbing might provide the only alternative in this respect, even after normal modes are included, which would turn the process into a race against time, where the IVR processes compete against the control.

3.3 Laser driven deuterium dynamics in deuterated phthalic acid monomethylester

In this Section, the required steps for the calculation of a CRS Hamiltonian from *ab initio* data found in the last section are applied to the intramolecular proton dynamics in phthalic acid monomethylester (PMME). This molecule is shown in Fig. 3.51 in its equilibrium geometry. It was chosen for this study, because recent experiments by Stenger *et al.*[30] demonstrated coherent vibrational dynamics of the O-H bond in this molecule, using ultrafast IR pump–probe spectroscopy. This indicates, that the movement of the bond is modulated by lower frequency modes of the molecular scaffold, exactly the effect, which the CRS Hamiltonian should be suited to simulate.

3.3.1 Stationary Infrared Spectra and Lineshapes

Before presenting the experimental results and the MCTDH calculations obtained for the PMME molecule, a look is taken at the basics of spectral lineshapes. Some molecular properties, especially the interaction between the different molecular normal modes, can be described via the stationary infrared (IR) spectrum. This results directly from the interaction of the molecular dipole moment $\hat{\mu}$ with an external field. To allow the theoretical

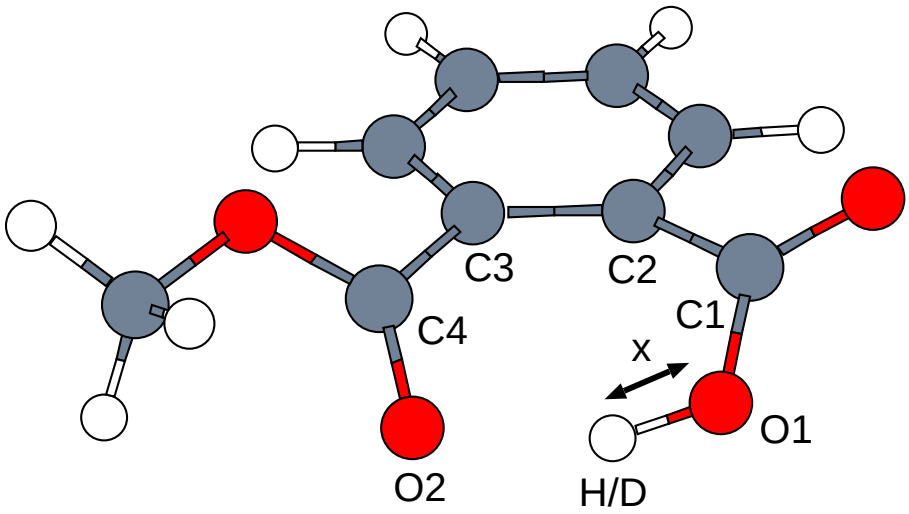

Figure 3.51: The PMME molecule in its equilibrium configuration, as obtained from a geometry optimization on the MP2 level of theory and a 6-31+G(d,p) basis set. The atoms most important for the hydrogen transfer are labeled, and the bond $R_{O1-H/D}$ is singled out as the reaction coordinate x.

description of such a spectrum, one has to employ the idea of linear response theory (Ref. [61], Chapter 3 and 5).

Within this approach, the linear dielectric susceptibility of a quantum system can be obtained from

$$\chi(t) = \frac{i}{\hbar} n_{\mathrm{mol}} \Theta(t) \left(e^{iE_0 t/\hbar} \langle \psi_0 | \, \hat{\mu} \hat{\mathbf{U}}_{\mathrm{mol}}(t) \hat{\mu} \, | \psi_0 \rangle - \mathrm{c.c.} \right) . \tag{3.18}$$

In this equation, n_{mol} is the volume density of the molecule in the sample volume, $\Theta(t)$ is the step function, $|\psi_0\rangle$ is an eigenstate of the operator $\hat{\mathbf{H}}_{\mathrm{mol}}$ of the system, with the energy E_0 and $\hat{\mathbf{U}}_{\mathrm{mol}}(t)$ is the propagation operator for the molecular system. In words, this can be interpreted as multiplying an initial eigenstate of the system with the dipole operator, propagating the resulting, non–stationary wavepacket in time, and calculating the overlap of this propagated state with the initial wavefunction. The half sided Fourier transform of this dipole autocorrelation function results in the absorption spectrum [61]:

$$\alpha(\omega) \sim \Re \int_0^\infty dt \, e^{i\omega t} \langle \psi_0 | \, \hat{\mu} \hat{\mathbf{U}}_{\mathrm{mol}}(t) \hat{\mu} \, | \psi_0 \rangle \, . \tag{3.19}$$

The lines of the stationary spectrum resulting from Eq. (3.19) are generated by the vibrations of the molecule under the influence of an electric field. The lineshape reflects some of the couplings between the normal modes of the molecule and their environment (cf. Fig. 3.52). For the interaction between normal modes there are two main mechanisms, with which they can interact:

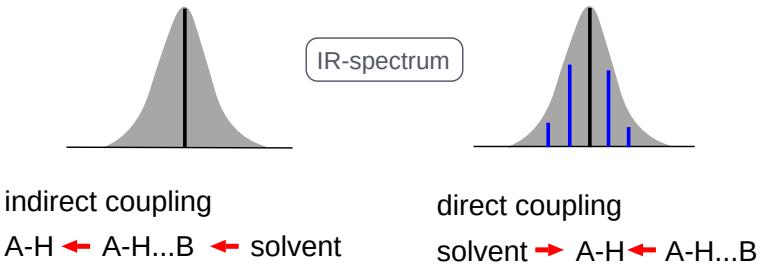

Figure 3.52: The two different approaches to the broadening of hydrogen spectral lines. The left panel shows the approach of Robertson[25], in which an indirect coupling is proposed. In this, the environment couples to the $\mathbf{X-H\cdots Y}$ mode, which then couples to the **X**–**H** vibration, resulting in a broad spectral peak. On the right the model of Ratner[24] proposes a direct coupling of the environment to **X**–**H**, while this vibration couples to $\mathbf{X-H\cdots Y}$ and therefore shows a vibrational progression, which is then hidden by the environmental broadening.

1. The movement along one mode can generate a coupling force in another one (anharmonic coupling). This results in the higher frequency mode (ω_{high}) to be accompanied by a number of vibrational sidebands, separated by multiples of the lower frequency (ω_{low}). So in addition to the main line there are lines at $\omega_{\text{high}} + n \cdot \omega_{\text{low}}$; $n = 1, 2, \ldots$, similar to Frack–Condon progressions in electronic spectroscopy. This is shown in Fig. 3.53a, where the vibrational progression and the red shift of the main line down from $\omega/2\pi c \approx 2350\,\text{cm}^{-1}$ are clearly visible.

2. If multiple excitations of one mode exactly match the frequency of another one, there is a resonance effect, producing a double peak, one red and the other blue shifted. (Fermi resonance between, e.g., a bending overtone and the O–H fundamental vibrational mode.) An example of this is shown in the dotted spectrum of Fig. 3.53c. In this, the peaks have strongly different oscillator strength, as the dipol moment is oriented mainly along the fundamental O–H mode, but one sees that the lines are shifted away from $\omega/2\pi c \approx 2350\,\text{cm}^{-1}$, which is the frequency of the main mode and twice that of the additional one.

3. If both effects are present, the spectrum will be modified by all the factors listed above. This is shown in Fig. 3.53b and the solid spectrum in Fig. 3.53c. In this last spectrum, one also sees, that the interaction of the low frequency mode with the Fermi resonance is strongly affected as well. The spacing of the vibrational progression gets smaller, and between the two main peaks (marked by the arrow) an indirect coupling to the high frequency normal mode, which is not directly coupled to the low frequency mode, becomes visible.

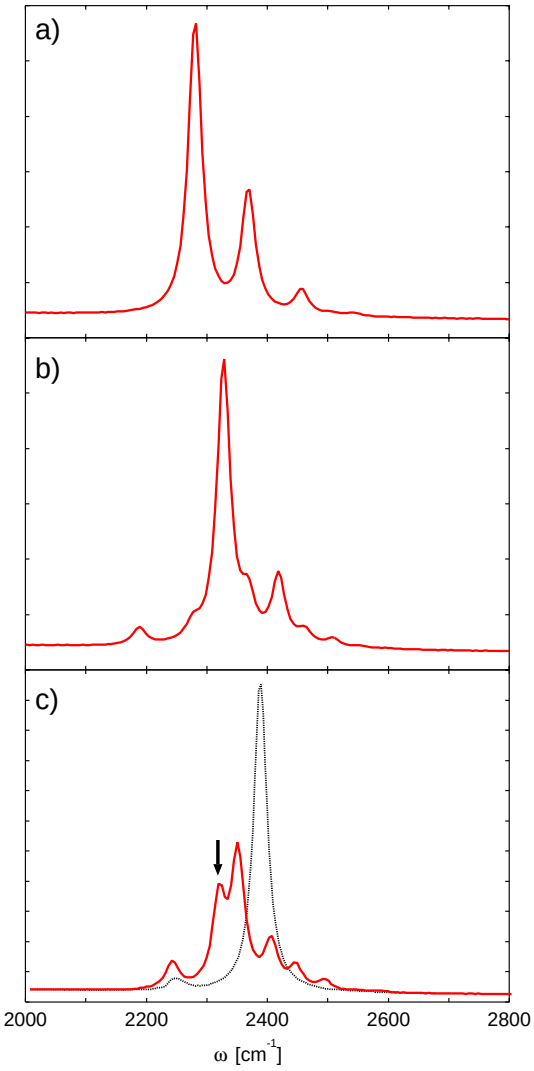

Figure 3.53: Different possibilities for the influence of anharmonic couplings between normal modes on the infrared spectrum. Panel **a)** shows a IR line at $\omega_{\text{main}}/2\pi c \approx 2350\,\text{cm}^{-1}$, coupled to a low frequency mode of $\omega_{\text{low}}/2\pi c = 100\,\text{cm}^{-1}$. The vibrational sidebands, and the fact that the main line is red shifted, are clearly visible. In panel **b)** an additional high frequency mode with $\omega_{\text{high}}/2\pi c = 1150\,\text{cm}^{-1}$ (uncoupled to the low frequency one), is added. Two vibrational quanta in this mode are almost in resonance with the base line, modifying the spectrum, pushing the base IR line to a higher frequency. In panel **c)**, the frequency of the second mode is changed to $\omega_{\text{high}}/2\pi c = 1175\,\text{cm}^{-1}$, bringing its two quanta overtone excitation into exact resonance and producing significant change in the spectrum. (See text, the arrow denotes an indirect coupling, which is also visible later in Fig. 3.54.) For the dotted line, the coupling to the low frequency mode is switched off. This shows the extent of the effects this coupling has on the dynamics.

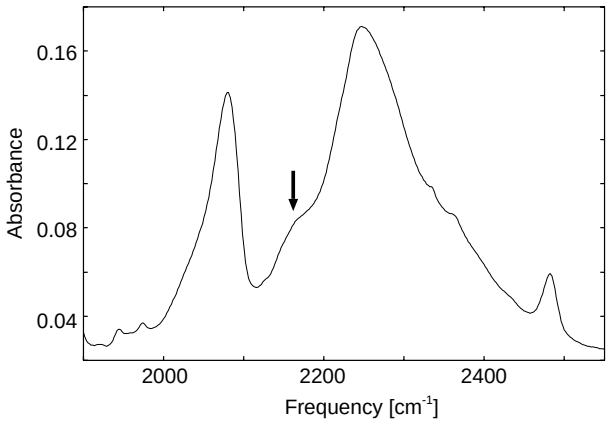

Figure 3.54: The experimental linear O-D stretching absorption spectrum of PMME. The arrow denotes a possible indirect coupling as the one shown in Fig. 3.53c. (Reproduced with permission from [30])

Both of these effects can contribute to the fact, that the spectral lines observed in complex systems often consist of very broad peaks, as all the lines generated can be broadened by the environment. So a double peak generated by a resonance, or a vibrational progression of a very low frequency mode often results in a single, smeared out line in spectrum, with all substructure lost. In Fig. 3.52, the two different approaches to the coupling of these spectral lines to the environment is sketched out. In the indirect coupling model of Robertson[25] the bath only couples to the normal modes, which then modify the O–H vibration. If these broadened normal modes then couple to the O–H, the spectrum will only show a single broad band without substructure. The direct coupling model of Ratner[24] proposes a coupling between the O–H vibration and the normal modes as shown in Fig. 3.53, which then couples to the bath and gets smeared out. This will also result in a broad band, but with a hidden substructure of possible normal mode couplings underneath. If these are present, it is possible to observe them via coherent wavepacket excitations of the normal modes with femtosecond spectroscopy, which motivates the experiments on PMME described in the following section.

3.3.2 Experimental Data

In the experiment the carboxy deuterated derivative of the PMME molecule is used, to avoid the interference of the C-H stretching modes with the observation of the O-D bond vibration. For this PMME-D complex, pump–probe experiments in the mid–infrared were performed, to study the dynamics of the O-D bond. The stationary IR spectrum of the molecule is shown in Fig. 3.54. It shows some typical features of intramolecular hydrogen bonds, namely strong broadening and a significant red-shift compared to typical harmonic frequencies of an O–D vibration calculated via *ab initio* methods. Additionally, in this

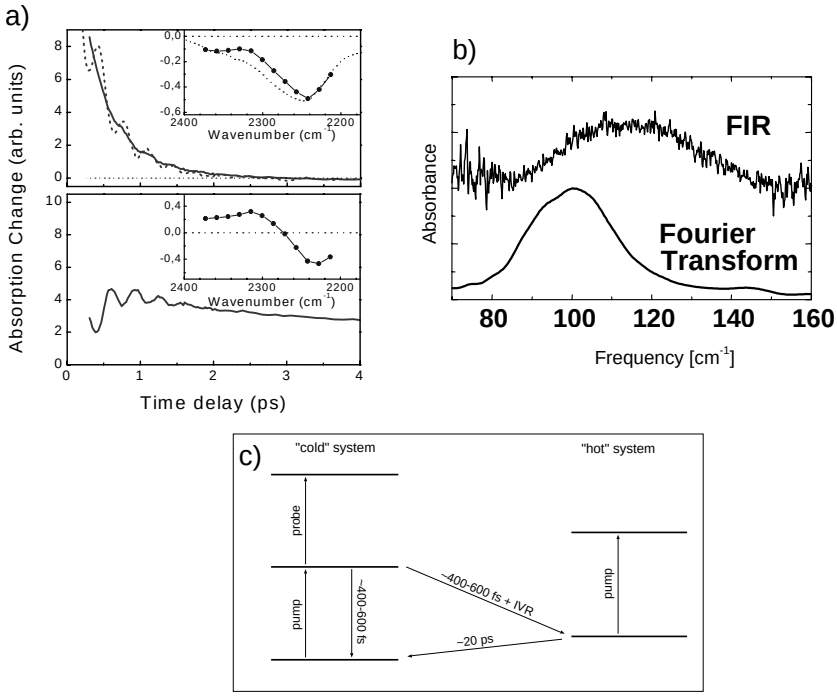

Figure 3.55: a) Temporal evolution (solid lines) and spectra (insets) of the two dominant components from the pump–probe probe spectrum. Plotted is the time–resolved absorbance change for a pump pulses centered at $2300\,\mathrm{cm}^{-1}$ and probe pulses at $2315\,\mathrm{cm}^{-1}$, $2271\,\mathrm{cm}^{-1}$ and $2213\,\mathrm{cm}^{-1}$ (solid lines) and pump at $2100\,\mathrm{cm}^{-1}$ and probe at $2028\,\mathrm{cm}^{-1}$ (upper panel, dashed line). **b)** The Fourier transform of the signal in the lower panel of a), together with the far infrared (FIR) vibrational spectrum of PMME-D. (Reproduced with permission from [30]) **c)** The proposed excitation and relaxation processes for the pump–probe experiment of PMME [139], with the associated timescales.

case the band shows a splitting into two main subbands. As the coupling of the O-D bond dynamics to the other normal modes of the molecule cannot be derived from the stationary spectrum, the pump–probe approach is necessary for this. The experimental setup consisted of an infrared laser source providing pulses of duration $t = 130\,\mathrm{fs}$ and $1\,\mu\mathrm{J}$ energy (approximately $1.3 \cdot 10^{11}\,\mathrm{W/cm}^2$). The target molecule PMME-D was prepared in a solution of non-polar C_2Cl_4. Further details of the experimental setup can be found in [30].

The results of the pump–probe measurements are shown in Fig. 3.55. There are two main features visible in the absorption change, one showing an exponential decay with a time constant of $\tau_1 \approx 400\,\mathrm{fs}$, with weak oscillations superimposed. The second component shows strong oscillations up to a time of $t_{\mathrm{osc}} \approx 1.5\,\mathrm{ps}$ and a slow relaxation with a time constant of $\tau_2 \approx 20\,\mathrm{ps}$. From the experimental data, the decay time τ_1 was interpreted as

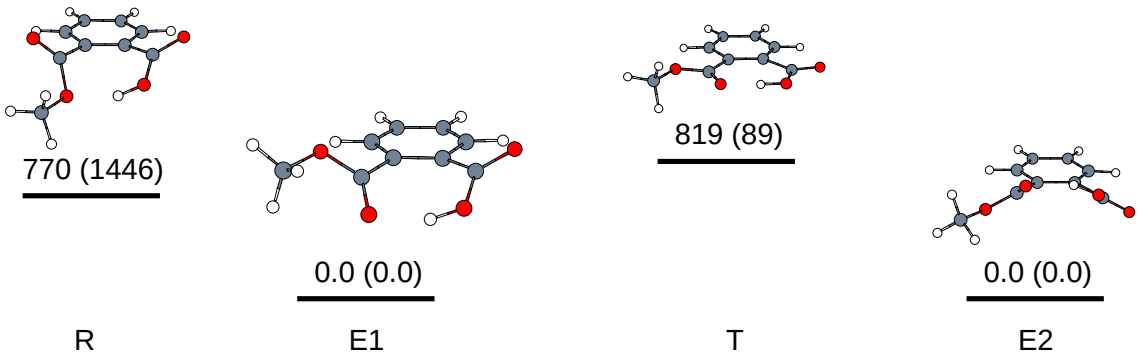

Figure 3.56: Various conformations of PMME at its stationary points. The numbers give the energies of the geometry, with respect to the lowest energy conformer, in cm^{-1}. The first number results from a MP2 calculation, in brackets the corresponding value for a DFT/B3LYP calculation is shown. Both times, a Gaussian 6-31+G(d,p) basis set was used.

the vibrational lifetime of the first excited state ($\nu_{OD} = 1$) of the O-D vibration. The other time constant τ_2 was identified with the excitation and subsequent decay of low frequency normal modes in PMME-D. This is shown in the levle scheme (Fig. 3.55c) with the relevant time constants. The key feature here is the fact that the system can return to a "hot" vibrational ground state of the O–D bond, i.e. one where the bond is in the ground state, but the molecular scaffold is in an excited state. This "hot" ground state can be observed via the measurements of the coherent oscillations in the pump–probe spectrum. These can be interpreted as a coherent excitation of a vibrational wavepacket in a low frequency normal mode, caused by the laser pulse pumping the system from $\nu_{OD} = 0$ to $\nu_{OD} = 1$ and then transfering energy to the molecular scaffold. Further details about the experimental data and interpretations can be found in [30].

The challenge to the theory now is, to construct a suitably accurate model of the O-D bond dynamics in PMME-D, to see if the interpretations of the experimental results can be supported by quantum dynamical calculations. In the next sections, the energy relaxation processes are modeled on the basis of IVR processes only, i.e. no dissipation to a bath is included.

3.3.3 The CRS Hamiltonian

As in the calculation for HIP (Section 3.2), the calculation of the CRS Hamiltonian for PMME starts with the analysis of the stationary states of the molecule, as produced by quantum chemistry programs. In the following, all calculations are performed with the GAUSSIAN98 program package [133] (example input files can be found in Appendix D.1). To treat the hydrogen bonding correctly, the MP2 method, or alternatively a DFT with

		MP2	DFT/B3LYP
bonds	H-O1	0.983	0.992
	O1-C1	1.343	1.330
	C1-C2	1.518	1.534
	C2-C3	1.488	1.494
	C4-O2	1.235	1.229
	O2-H	1.702	1.539
angles	H-O1-C1	111.2	112.4
	O1-C1-C2	119.4	120.2
	C1-C2-C3	128.0	129.8
	C2-C3-C4	124.2	124.9
	C3-C4-O2	125.4	125.9
dihedrals	H-O1-C1-C2	-9.4	-8.3
	O1-C1-C2-C3	**38.9**	**25.3**
	O2-C4-C3-C2	**-37.1**	**-23.8**

Table 3.7: Equilibrium geometry parameters of PMME for the lowest energy conformer from the MP2 and DFT/B3LYP calculations. Bond lengths are given in Å, angles in degree. The labels correspond to the ones given in Fig. 3.51.

the B3LYP functional are used. The basis set used for all calculations is a Gaussian 6-31+G(d,p). The resulting most stable configurations are shown in Fig. 3.56 for the MP2 method, the energies relative to the minimum energy conformation are given therein for both methods.

In Table 3.7 the geometry parameters of the most stable conformer, for the bonds and angles relevant to the hydrogen bonding, are listed for both methods. One can see, that the molecule is not planar in its lowest energetic state. From this, it easily follows, that there is an isoenergetic enantiomer, created by mirroring the molecule on the plane of the ring system. These two are separated by a planar (apart from the methyl group) transition state. These states are labeled in Fig. 3.56 as **E1** and **E2** for the minima, and **T** for the transition state between them. An additional isomer is the hydrogen–bonded rotamer **R** with respect to the ester group, which is of much higher energy than **E1** and **E2**. The biggest difference between the MP2 and the DFT methods is, that the minimum energy structure predicted by DFT theory is more planar than the one calculated by MP2, which also results in a significantly lower barrier between the enantiomers. In the following, the MP2 method is used to generate the CRS potential surface, as this is expected to be a more reliable approximation than DFT. The MP2 results give a barrier between the enantiomers of sufficient height to assume that the molecule remains localized in one of the configurations **E1** or **E2**. Configuration **E1** was then chosen as the starting point for the construction of a reaction surface for the dynamics of the intramolecular hydrogen

bond, O1–D$\cdots$O2. The analysis of the stationary points also shows, that there is no stable configuration with the hydrogen connected to the ester group. Therefore the dynamics does not result in a true transfer reaction (as there is no second minimum to transfer to), but only produces a vibration of the hydrogen bond. As the molecule is not planar, the representation of this vibration in Cartesian coordinates either has to take all three degrees of freedom of the hydrogen into account, or restrict the movement to reduced, one dimensional reaction coordinate, only describing the length of the O–D bond. As a frequency calculation at the **E1** configuration shows a normal mode corresponding to an almost pure OD stretching vibration, restricting the deuterium motion to one dimension should be a good approximation for small amplitude oscillations.

Following these initial considerations, the CRS Hamiltonian is build for a Cartesian reaction coordinate described by $\mathbf{x} = (x \equiv R_{OD}, y = 0, z = 0)$ (i.e. the coordinate system is rotated in such a way, that the x direction points along the OD bond, as indicated in Fig. 3.51). The reference geometry $\mathbf{Z}^{(0)}$ for the harmonic normal modes, describing the remaining degrees of freedom, is set to the **E1** configuration (cf. Section 2.2, page 25ff).

The one dimensional reference potential, calculated with the MP2 method along the defined reaction coordinate, is shown in the upper panel of Fig. 3.57. Also plotted are the three lowest eigenstates $\nu_{\mathrm{OD}} = 0, 1, 2$ resulting from the solution of the reference part of the CRS Hamiltonian $\hat{\mathbf{H}}_{\mathrm{sys}} |\phi_a\rangle = E_a |\phi_a\rangle$. To solve the Schrödinger equation, the Fourier grid method was used (Appendix A.2 and [99]). To allow the interaction of the molecule with an electric field, the change of the dipole moment along this coordinate has been calculated as well. The resulting dipole is nearly linear, with a value of $\mu(x = x_{\mathrm{eq}}) \approx 7\,\mathrm{D}$ and a slope of $d\mu/dx \approx 1.6\,\mathrm{D}/a_B$ at x_{eq}. From the level spacing in the potential one can see, that this is clearly an anharmonic mode. While a harmonic mode would have equidistant levels, in this case the level spacing decreases by more than $200\,\mathrm{cm}^{-1}$ when comparing ω_{01} to ω_{12}. This potential would only be poorly represented by a harmonic approximation, even though there is no real large amplitude displacements along it, due to the missing second minimum. One can see from the eigenfunctions that the dynamics of the bond, upon excitation to a state consisting of $\nu_{\mathrm{OD}} = 0$ and $\nu_{\mathrm{OD}} = 1$, can be expected to take place within a range of about $x_{\mathrm{eq}} \pm 0.4 a_B$ around the potential minimum.

To build the normal mode part of the CRS Hamiltonian, the harmonic modes of the molecular scaffold, without the moving deuterium, have to be calculated. For this, the force constant matrix for the molecule has to be generated for each point on the reference potential. The resulting set of force constants then has to be transformed following the algorithm described in Section 2.2, page 25ff. The result of this is a set of matrices $\mathbf{K}(x)$ and forces $\mathbf{f}_n(x)$, both depending on the reference coordinate x. The matrices are diagonal for $x = 0$, and then contain the square of the normal mode frequencies on the diagonal. Moving away from the equilibrium, off–diagonal coupling elements start to appear. The forces are all zero at $x = 0$, and only start to appear for a displaced deuterium atom. Taking into account the possible displacement of the deuterium within the reference potential,

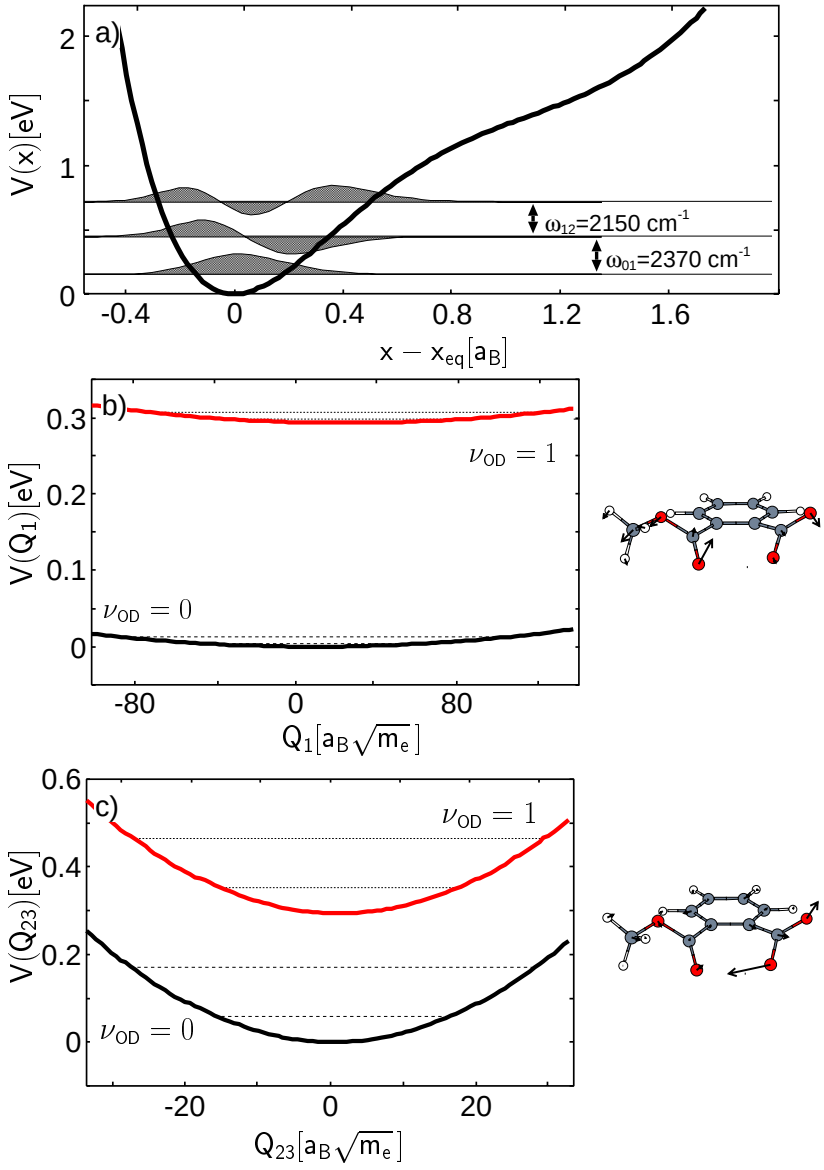

Figure 3.57: In panel **a)** the 1d potential energy, calculated with MP2 and a 6-31+G(d,p) basis set, along the reaction coordinate in PMME is shown, together with the three lowest eigenstates. The coordinate system has been shifted by $x_{\text{eq}} = 0.98$ Å$= 1.85\, a_B$, to start at zero in the equilibrium position. Panels **b)** and **c)** show the effective potentials for two of the normal modes, together with a characterization of the modes.

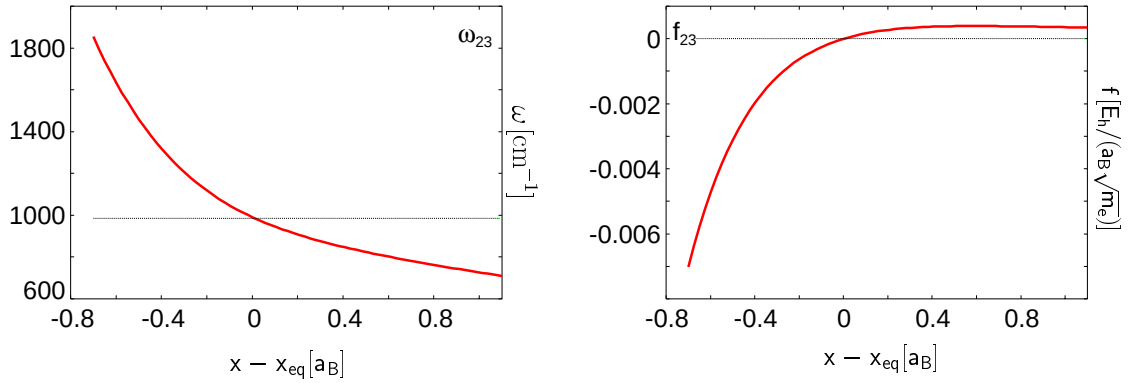

Figure 3.58: Frequency and force acting on normal mode ν_{23} of PMME.

these normal modes for the CRS Hamiltonian have been classified with respect to their reorganization energy (given by Eq. (2.40)) at the representative value $x_{\text{eq}} + 0.4a_B$. At this point the mode with the strongest coupling is ν_{23} with a frequency of $\omega_{23}/2\pi c = 985\,\text{cm}^{-1}$. The values of $\mathbf{f}_{23}(x)$ and $(K_{23,23}(x))^{1/2}$ are plotted in Fig. 3.58. Both the force acting on this normal mode, and its approximate frequency (given by the square root of the diagonal element of the force constant matrix) show a strong change for smaller OD bond length. This can be explained by looking at the character of the normal mode, shown in Fig. 3.57c. Its main component is a displacement of the O in the OD bond toward the D atom. It is clear, that this sort of movement is severely hampered, if the OD bond is shortened. Due to the large forces resulting from this, one can assume, that for this region of the potential the harmonic approximation breaks down. As is shown later in the dynamical calculation, this region will fortunately not be reached by the wavepacket. This analysis has to be done for each of the modes to be included into the CRS Hamiltonian.

Looking at the situation at $x_{\text{eq}} + 0.4a_B$, the total reorganization energy at this point is $E_{\text{reorg}} = 231\,\text{meV}$. More than half of this is located in the strongest coupled mode ν_{23}, which therefore strongly affects the dynamics of the hydrogen bond. As the experimental results showed an oscillatory signal with a frequency of around 100cm^{-1}, in addition to this mode, the strongest coupling one with a frequency below 200cm^{-1} was identified as ν_1 at $\omega_1/2\pi c = 68\,\text{cm}^{-1}$. These two modes (and all the ones added in further steps), are listed in Table 3.8 with their frequency and reorganization energy at $x_{\text{eq}} + 0.4a_B$. The vibrationally diabatic (VD) potentials $V_{aa}(q_n)$ for the two modes ν_1 and ν_{23} are shown in Fig. 3.57b and c. These potentials have been obtained from

$$\begin{aligned} \langle\phi_a|\,\hat{\mathbf{H}}_{\text{mol}}\,|\phi_a\rangle &\approx E_a + \sum_n \left(\hat{\mathbf{T}}_n + \frac{1}{2}\langle\phi_a|\,K_{nn}(x)\,|\phi_a\rangle\, q_n^2 - \langle\phi_a|\,f_n(x)\,|\phi_a\rangle\, q_n\right) \\ &= E_a + \sum_n \left(\hat{\mathbf{T}}_n + V_{aa}^{(n)}(q_n)\right), \end{aligned} \tag{3.20}$$

where the mode coupling ($\propto K_{mn}(x)$) has been neglected. These modes correspond to

mode i	$\omega_i/2\pi c$ (cm^{-1})	ΔE_i (eV)	SPF	grid (au)	DVR (points)	added for
x	**2370**	–	7	-0.8 – 1.1	40	3d
ν_{23}	985	$1.273{\cdot}10^{-1}$	C_x	-100.0 – 100.0	40	3d
ν_1	68	$9.469{\cdot}10^{-3}$	5	-250.0 – 250.0	40	3d
ν_3	147	$8.572{\cdot}10^{-3}$	5	-205.0 – 225.0	32	9d
ν_5	201	$8.925{\cdot}10^{-3}$	C_5	-175.0 – 200.0	32	9d
ν_7	263	$1.758{\cdot}10^{-2}$	5	-175.0 – 175.0	32	9d
ν_9	306	$9.143{\cdot}10^{-3}$	C_7	-175.0 – 175.0	32	9d
ν_{13}	507	$1.216{\cdot}10^{-2}$	5	-150.0 – 150.0	32	9d
ν_{24}	1011	$7.537{\cdot}10^{-3}$	C_{13}	-125.0 – 125.0	32	9d
ν_6	227	$2.286{\cdot}10^{-3}$	1	-200.0 – 200.0	24	19d
ν_8	283	$1.714{\cdot}10^{-3}$	1	-200.0 – 200.0	32	19d
ν_{10}	340	$0.816{\cdot}10^{-3}$	1	-150.0 – 150.0	32	19d
ν_{11}	412	$3.810{\cdot}10^{-3}$	1	-150.0 – 125.0	32	19d
ν_{14}	563	$5.714{\cdot}10^{-3}$	1	-150.0 – 150.0	24	19d
ν_{19}	754	$5.578{\cdot}10^{-3}$	1	-125.0 – 125.0	24	19d
ν_{20}	846	$4.898{\cdot}10^{-3}$	1	-125.0 – 125.0	32	19d
ν_{21}	861	$0.544{\cdot}10^{-3}$	1	-125.0 – 125.0	24	19d
ν_{25}	1048	$1.769{\cdot}10^{-3}$	1	-100.0 – 100.0	24	19d
ν_{47}	**2169**	$2.694{\cdot}10^{-3}$	1	-100.0 – 100.0	32	19d

Table 3.8: All the substrate modes, which couple strongly to the reference potential at $x = 0.4\,a_B$. The modes are grouped according to the dimension of the calculation they were included in, and list the grid parameters for the MCTDH program in columns four (number of SPF, where C_i means, that this mode was combined with the i^{th} mode to a 2d SPF), five (range of the grid) and six (the number of grid points). Both the bold normal mode and the sum of the two boxed ones are close to resonance to the $\nu_{OD}(0 \to 1)$ transition, which could provide a good relaxation channel.

extreme cases (ν_{23}: strongest coupling, ν_1: lowest frequency), and can be used (together with the reaction coordinate) to construct a minimal 3d model of the system. The two modes contain already 57% of the reorganization energy at $0.4a_B$ and include a low frequency mode to introduce the oscillations of the system observed in the experiment. This model is extended in two further steps: First six more modes with reorganization energies greater than 6 meV (about 50 cm^{-1}) can be identified which also influence the hydrogen bond. These six modes are listed in the second block of Table 3.8. Together with the first three, one now has a 9d model, which contains about 85% of the total reorganization energy. For the largest model simulated in this work, the next 10 normal modes with respect to decreasing coupling strength were selected to build a 19d model containing 96% of the reorganization energy at $x_{\mathrm{eq}} + 0.4a_B$. From this one can see, that the remaining energy is spread out in ever smaller portions over all the remaining modes. Adding further modes brings no real improvement of the model, as the very small amount of energy not assigned shows, that all further modes are more or less uncoupled and do not interact with the oscillators already present at a time scale of below 2 ps. The models containing the modes presented in Table 3.8 are all constructed without further approximations, i.e. all off diagonal elements $K_{mn}(x)$ coupling two modes present in the model are included in the Hamiltonian.

3.3.4 MCTDH Results

The CRS Hamiltonians for the PMME models from the last section now are used in the time dependent Schrödinger equation Eq. (2.41). Together with a suitable initial wavefunction and a driving laser field, this will result in a dynamical wavepacket simulation for the deuterium dynamics in PMME-D. As an exact solution of the high dimensional problem is beyond the capabilities of todays computers, the problem is studied with the MCTDH method, presented in Section 2.4.4, which is especially suited to problems in the form of the CRS Hamiltonian (cf. page 49). The following dynamical calculations are performed using the Heidelberg MCTDH program package [140], which provides a flexible way to implement the CRS potential, generate initial wavefunctions, apply external fields to the system and analyse the results.

The implementation of the CRS Hamiltonian calculated in the last section into this program requires one further approximation step. Up to now the data for V_{CRS} exists on a grid of points (namely on the points for which the force constant matrix was calculated). The MCTDH program requires the potential in an analytical form for the whole domain in which the grid is defined. This makes it necessary, to fit the values obtained for $\mathbf{K}(x)$ and $\mathbf{f}_n(x)$ at discrete values of x to continuous functions of x. Therefore, all the data required for a model was fitted to a set of polynomials ($f(x) = \sum_n C_n x^n$) or powers of exponentials ($f(x) = \sum_n C_n \exp\{\pm nx\}$). The choice of the kind of function to fit to was guided by the form of the data generated by the *ab initio* calculations. For instance, the forces for mode ν_{23}, shown in Fig. 3.58, are well suited for a fit to the exponential function. Most of the

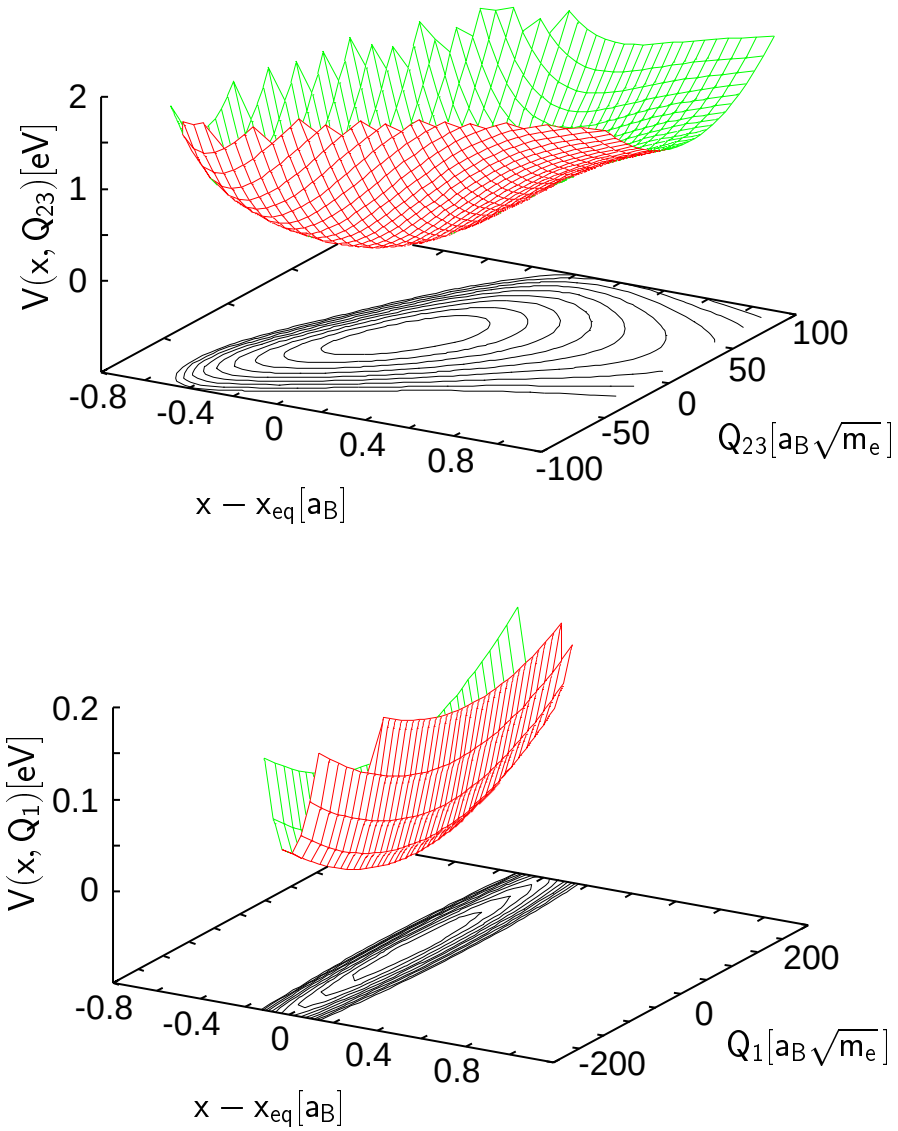

Figure 3.59: 2d cuts through the effective potential of PMME along the two normal modes ν_1 and ν_{23}. The cuts are for the 3d model, for each cut the cutting plane is at a value of zero for the mode left out. The anharmonic coupling is nicely visible in the upper panel.

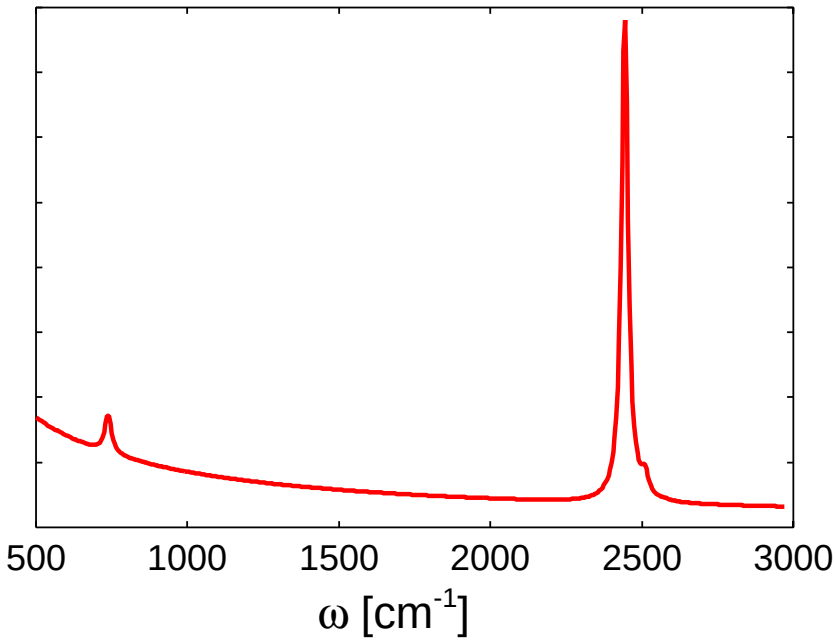

Figure 3.60: Stationary IR spectrum of the 3d PMME simulation. It results from the Fourier transform of the autocorrelation function from a 5 ps propagation of the dipole shifted ground state wavefunction. The rise for lower ω is a numerical artefact of the calculation.

other data could be fitted with simple polynomials up to fourth order.

The resulting analytical functions can then easily be included into the MCTDH package, which then allows the analysis of the resulting multidimensional surface by plotting various cuts of it. A set of exemplary 2d cuts through the 3d model potential is shown in Fig. 3.59. For all the following calculations, the reaction coordinate x is represented on a grid from $-0.8 \ldots 1.1 a_B$ with 40 points, as listed in Table 3.8. Example input files for the MCTDH programm are given in Appendix D.2.

3d calculation

The first calculation for the PMME molecule are done for the 3d model, including only the two modes ν_{23} and ν_1. This is the only calculation, in which the reaction coordinate was not combined with mode ν_{23} to a 2d mode. Both modes have seven 1d SPF instead. As an initial step to all further calculations, the ground state wavefunction of the CRS Hamiltonian has to be calculated. This is done using a relaxation method in "imaginary time" ([101] and note on page 42).

The zero point energy and the position expectation values for this ground state $|\psi_0\rangle$ are given in Table 3.9. Looking at the value for the reaction coordinate, one sees, that the

	3d	9d (TDH)	9d (MCTDH)	19d
ground state energy [eV]	0.210	0.371	0.358	0.816
$\langle x \rangle$ $[a_B]$	0.0345	0.0516	0.0434	0.0579
$\langle q_{23} \rangle$	0.97	2.5040	1.88	3.29
$\langle q_1 \rangle$	11.29	14.8871	13.78	16.91
$\langle q_3 \rangle$	–	-5.5724	-4.42	-6.90
$\langle q_5 \rangle$	–	-3.6963	-2.93	-4.44
$\langle q_7 \rangle$	–	4.2857	3.27	5.44
$\langle q_9 \rangle$	–	2.4640	2.02	3.16
$\langle q_{13} \rangle$	–	1.9558	1.44	2.52
$\langle q_{24} \rangle$	–	-0.7246	-0.54	-0.92
$\langle q_6 \rangle$	–	–	–	2.72
$\langle q_8 \rangle$	–	–	–	1.13
$\langle q_{10} \rangle$	–	–	–	0.70
$\langle q_{11} \rangle$	–	–	–	-1.84
$\langle q_{14} \rangle$	–	–	–	-1.69
$\langle q_{19} \rangle$	–	–	–	-1.13
$\langle q_{20} \rangle$	–	–	–	0.99
$\langle q_{21} \rangle$	–	–	–	0.13
$\langle q_{25} \rangle$	–	–	–	0.48
$\langle q_{47} \rangle$	–	–	–	-0.03

Table 3.9: The zero point energies and the positions on the grid of the ground state wavepackets for the models of different dimensionality. The position expectation value for the normal modes is given in coordinates mass weighted with the electron mass $[a_B\sqrt{m_e}]$. $\langle x \rangle$ is given with respect to $\langle x_{\mathrm{eq}} \rangle$.

anharmonicity of the reference potential already results in a expectation value away from zero. This, in turn, "switches on" the interaction between the normal modes, which would be zero for $x = 0a_B$. As a result, the minima of the normal modes are also shifted away from zero for the ground state. One sees, that the low frequency mode ν_1, due to its low force constant, is shifted by a much larger value than ν_{23}, even though its coupling to the reaction coordinate is much weaker.

To generate a stationary spectrum for this model system, one has to follow the outline given in Section 3.3.1. The eigenstate $|\psi_0\rangle$ is multiplied with the dipole moment operator of the system, and the resulting non–stationary state is propagated with the MCTDH program without any external field. The overlap of the time dependent function calculated with the initial function $\mu\,|\psi_0\rangle$ gives an autocorrelation function, whose Fourier transform in turn gives the spectrum of the system. The results for this procedure are plotted in Fig. 3.60. In this spectrum one can identify three contributions. The main peak visible results from the transition from $\nu_{\mathrm{OD}} = 0$ to $\nu_{\mathrm{OD}} = 1$ in the reaction coordinate. The smaller peak at around $700\mathrm{cm}^{-1}$ is the signature of mode ν_{23}, which has been red-shifted by its couplings to the reaction coordinate (as can be seen in Fig. 3.58, the frequency of this mode decreases for $x > 0$), and its interaction with the low frequency mode. The last contribution is from the mode ν_1, which adds a weak vibrational progression to the main peak. If one looks ahead to the higher dimensional models, for which these calculations have been repeated, this result will, qualitatively, stay the same. All the additional modes considered only introduce small shifts in the location of the peaks and overall broadening. Due to their small coupling strengths and non–resonant frequencies, they add no further structure to the spectrum.

Comparing the calculated with the experimental spectrum plotted in Fig. 3.54, one sees only a single peak at the correct frequency but no splitting into two subbands is observed. Only a slight vibrational progession is found. To understand this, one has to look at the limitations of the model: The molecule is calculated with a fixed scaffold, only the hydrogen is allowed to move. Therefore all other possible configurations of the molecule are not included in the simulations. A configuration like the rotamer shown in Fig. 3.56 is not included in the model, althogh at the MP2 level they should not be populated at room temperature. At the same time, the coupling of the hydrogen movement to a normal mode vibration does not contain enough oscillator strength to produce the two peaks of nearly equal height found in the experimental spectrum for this model. This can be caused by a limitation of the model, e.g. a wrong frequency for a normal mode resulting from the MP2 approximation, which moves the mode away from a resonance, it can also point to the fact that another scaffold configuration, e.g. the rotamer, which has a slightly weaker H–bond, could be responsible for this peak structure. In addition to the fixed scaffold, the reaction coordinate was restricted to one dimension, disallowing any movements away from the line given by the OD bond. Such a restriction normally results in a potential with a higher frequency, than the one generated from a system allowed to

move along all three degrees of freedom. In addition, the Fermi–resonance with the real bending overtone might give rise to a double peak structure, as seen in Fig. 3.53c. In the harmonic normal mode approximation, mode ν_{40} reminds of a bending vibration which, in the full 3d description, would have a frequency of 1460cm^{-1} and an overtone relatively close to the O–D frequency. Another simplification is, that the dipole moment μ has only been calculated for the reaction coordinate. Due to this, the wavepacket $\mu\,|\psi_0\rangle$ is only shifted along this coordinate. All the oscillator strength in the normal modes therefore only results from the couplings between them and x. Adding a dipole moment along the normal modes as well might increase the signature of one of these lines significantly. Perhaps the biggest difference between the model and reality is that the experiment has been performed in solution, while all the *ab initio* calculations for the CRS Hamiltonian have been made for a isolated molecule. This can change the character of some of the normal modes significantly, e.g. hindering the large amplitude rotations of the ester group. Looking at the lineshapes in Fig. 3.53, it would be enough for one normal mode to change its frequency into a favorable resonance with the transition in the reaction coordinate, to generate a completely different spectrum.

Keeping the limitations of the model in mind, the following calculations concentrate on the excitation in resonance with the single peak generated by the simple 1d model. This treatment will be justified by the reproduction of the periodic, coherent wavepacket excitation in the results, which match the most most prominent experimental result, i.e. the periodic modulation of the pump–probe signal. The next step therefore is the calculation of the wavepacket dynamics with the CRS Hamiltonian. To do so, the CRS Hamiltonian is augmented with a dipole term in the form

$$\hat{\mathbf{H}}_{\text{field}} = -\mu(x)\mathcal{E}(t) \quad \text{with} \quad \mathcal{E}(t) = E_0 \sin^2(\pi t/\tau)\cos(\Omega t) \quad (0 \le t \le \tau). \tag{3.21}$$

This type of excitation by a $\sin^2$–pulse was already used in the previous sections. For the present calculation, the parameters of the pulse are: $\tau = 300\,\text{fs}$, $E_0 = 5 \times 10^{-4}\,E_h/ea_B$ and $\Omega/2\pi c = 2445\,\text{cm}^{-1}$ (fundamental ν_{OD} transition in the 3d potential), as plotted in Fig. 3.61a. This driving field only populates the first excited state in the reaction coordinate appreciably.

In Fig. 3.61c-d the dynamics of the expectation values for the reaction coordinate and the substrate modes ν_1 and ν_{23} is shown. The field induces a rapid oscillation in the reaction coordinate, with a frequency corresponding to that of the $\nu_{\text{OD}} = 0 \rightarrow 1$ transition. One can see clearly, that the vibration is not moving around zero, but around the displaced expectation value $\langle x\rangle = 0.0345 a_B$ calculated for the ground state wavefunction. The range covered by the dynamics reaches approximately from -0.01 to $0.09\,a_B$, while the variance of the wavepacket oscillates slightly, but remains on average constant around $0.12\,a_B$. This shows, that the total system stays well localized around the potential minimum.

Due to the relatively strong anharmonic couplings between x and ν_{23} in V_{CRS} the fast oscillations of $\langle x\rangle$ are imposed on the dynamics of $\langle q_{23}\rangle$. This can be seen in Fig. 3.61c. The force $f_{23}(x)$ is acting in a way, that $\langle q_{23}\rangle$ is pushed to lower values if $\langle x\rangle$ is at the

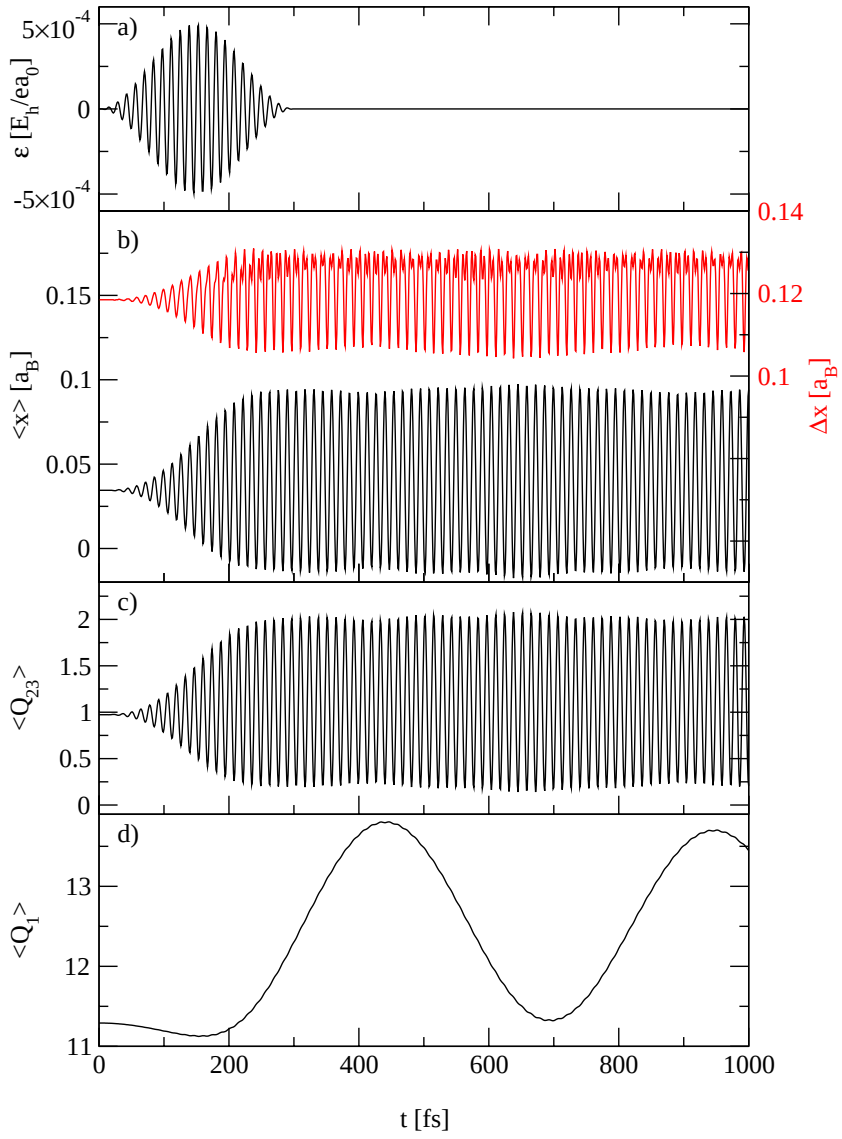

Figure 3.61: The development of the expectation values of the reaction coordinate and the normal modes. The upper panel shows the laser field acting on the system, which induces the dynamics. Panel **b)** shows the value and the variance of the reaction coordinate x, the other two the expectation value of the modes ν_{23} and ν_1 (in units of $[a_B\sqrt{m_e}]$).

outer turning point. Overall the excitation of ν_{23} is rather small due to the large frequency mismatch between these two coordinates.

Looking closely at the fast oscillations of $\langle x \rangle$, one can see that their amplitude is modulated with a period of around 500 fs. This is caused by the anharmonic coupling to the substrate mode ν_1 whose dynamics is shown in Fig. 3.61d. This mode is only weakly coupled to x, compared to ν_{23}, so it gets excited, but does not show a direct imprinting of the fast oscillations in x on its dynamics. If one analyses the character of this normal mode (shown in Fig. 3.57c), one can see, that an increase of $\langle q_1 \rangle$ causes a compression of the hydrogen bond, which then is reflected in a decreased amplitude of $\langle x \rangle$.

A further analysis of the 3d model calculations showed only marginal values for effects like energy and population redistribution between the modes. These processes are much better visible in the calculations for the 9d model presented in the next section. Therefore all the other methods to extract information from the calculation are presented there, together with a short comparison of the results for the 9d system with the ones obtained in this section for the 3d model.

9d calculation

As mentioned in the last section, the stationary spectrum of the 9d model produces no qualitative difference to the 3d results. The only difference is a slight shift in the fundamental transition frequency $\nu_{\mathrm{OD}} = 0 \rightarrow 1$ to $\Omega/2\pi c = 2430\,\mathrm{cm}^{-1}$, which was used in the following in the laser pulse driving the dynamics. The other parameters of the laser remain the same.

Before the MCTDH calculation on the 9d model is presented, a look is taken at the results from a TDH calculation with this 9d CRS Hamiltonian. This is done to show the effects of the multiconfiguration approach on the dynamics.

As for the 3d case, the initial state is generated by relaxing the system to its lowest energy state. The zero point energy and the mode expectation values for this state are given in Table 3.9. As each additional mode adds its zero point energy to the system, obviously the resulting ground state has a higher total energy than the one for the 3d model. This also results in a wavefunction which has a larger energy component in the anharmonic couplings than before, which in turn leads to higher values for $\langle x \rangle$, $\langle q_1 \rangle$ and $\langle q_{23} \rangle$, as shown in Table 3.9.

Starting from this initial function, the mode dynamics generated by the laser is plotted in Fig. 3.62. One sees, that the basic features already seen for the 3d model remain the same. The reaction coordinate is excited at its resonance frequency, oscillating around its initial value. As a result of the stronger couplings, the amplitude of the vibration is higher. The fast oscillation again couples directly to the dynamics of $\langle q_{23} \rangle$, while $\langle q_1 \rangle$ gets excited at its own frequency. Looking closer one sees, that one feature of the 3d results is missing from the TDH calculation. There is no noticeable influence of the dynamics of $\langle q_1 \rangle$ on the amplitude of the oscillations of $\langle x \rangle$. So even though additional modes were added, the 9d

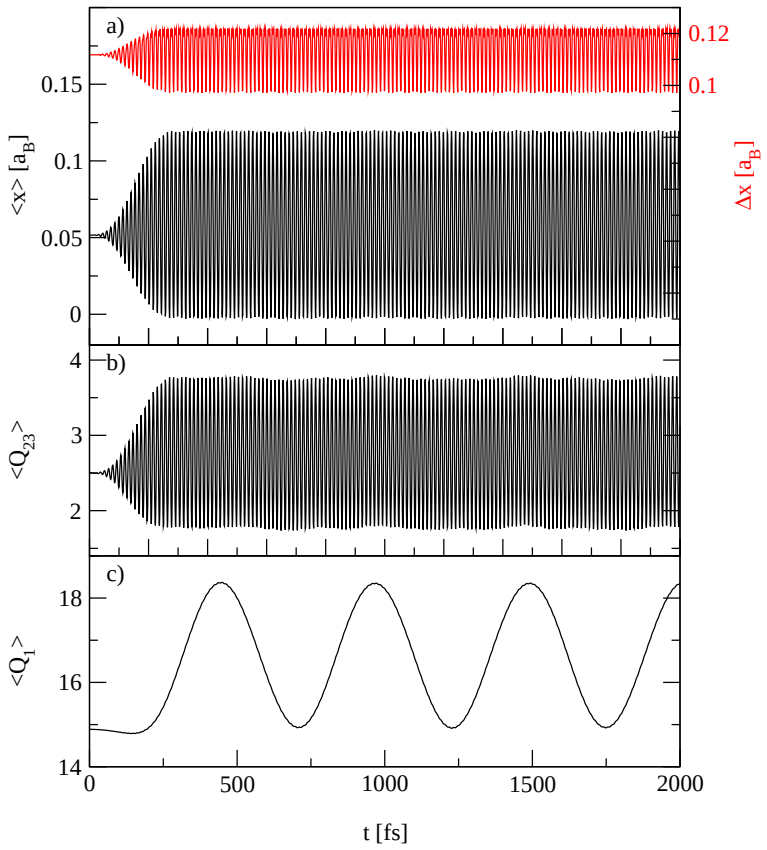

Figure 3.62: Same as in Fig. 3.61, only for the 9d model in TDH limit. The laser field has been omitted, as it only differs marginally in frequency from the one shown there.

model in TDH approximation shows less coupling between the modes than the 3d model in a MCTDH calculation. Keeping this in mind, one can now move to the 9d MCTDH results.

For the description of the 9d model, the possibility to combine modes into 2d SPF was used, to increase efficiency. The mode combination reduces the size of the SPF basis set required as correlations within the combined modes are treated explicitly [108]. At the same time the total number of modes is reduced, decreasing the effort further. Of course, this is partly offset by the larger size of the SPFs for the combined modes, which now require the propagation of numerically exact 2d wavepackets. To treat the strongest coupling in the 9d model explicitly, the reaction coordinate x has been combined with the strongest coupled mode ν_{23} using 7 SPFs. The combinations for the other modes have been chosen based on frequency matching and using 5 SPFs: ν_1, (ν_3, ν_5), (ν_7, ν_9), and (ν_{13}, ν_{24}). This, and the grid parameters used for the modes, is listed in Table 3.8 (page 142). This implementation results in a model with 5 MCTDH "particles" and a total of

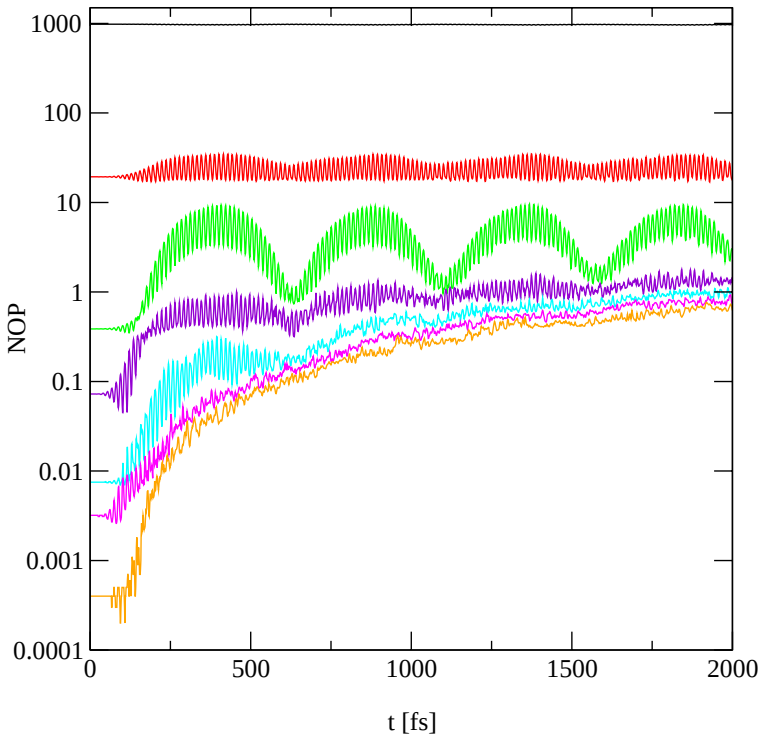

Figure 3.63: Natural orbital population (scaled to 1000=100%) for the combined mode (x, ν_{23}) in the 9d MCTDH calculation.

4375 $(= 7 \cdot 5^4)$ configurations for the MCTDH propagation. To give a comparison, this configuration requires the storage of 20 615 000 grid-points (4375 configurations with 4712 grid-points each). Assuming the storage of the wavefunction in double precision complex numbers, needing 16 bytes each, this requires approximately 315MB of memory. The full grid, in contrast, would have $6.87 \cdot 10^{13}$ grid-points, needing on the order of 1PB of storage.

The relaxation with the MCTDH method produces a ground state, which is slightly below the one generated by the TDH calculation. This is to be expected, as the multi-configuration wavepacket is more flexible and therefore can find a configuration which is closer to the "true" ground state. Due to the lower energy, the value of $\langle x \rangle$ is also lower, resulting in lower mode couplings and overall lower absolute values for the $\langle q_i \rangle$, as can be seen in Table 3.9.

To check the convergence of the multiconfiguration approach, one can take a look at the natural orbital population (NOP) for each mode. These natural orbital can be seen as a basis for the MCTDH wavefunction. They are obtained as the eigenvectors of the operator $\rho_{jl}^{(\kappa)}$ defined in Eq. (2.138) in Section 2.4.4. As with any basis set, there is in principle an infinite number of them, but for the numerics, a finite subset has to be picked. (For an exact definition of the NOP, see [108].) The number of orbitals for each mode is equal to the number of SPFs provided for it. To check the quality of the set, the

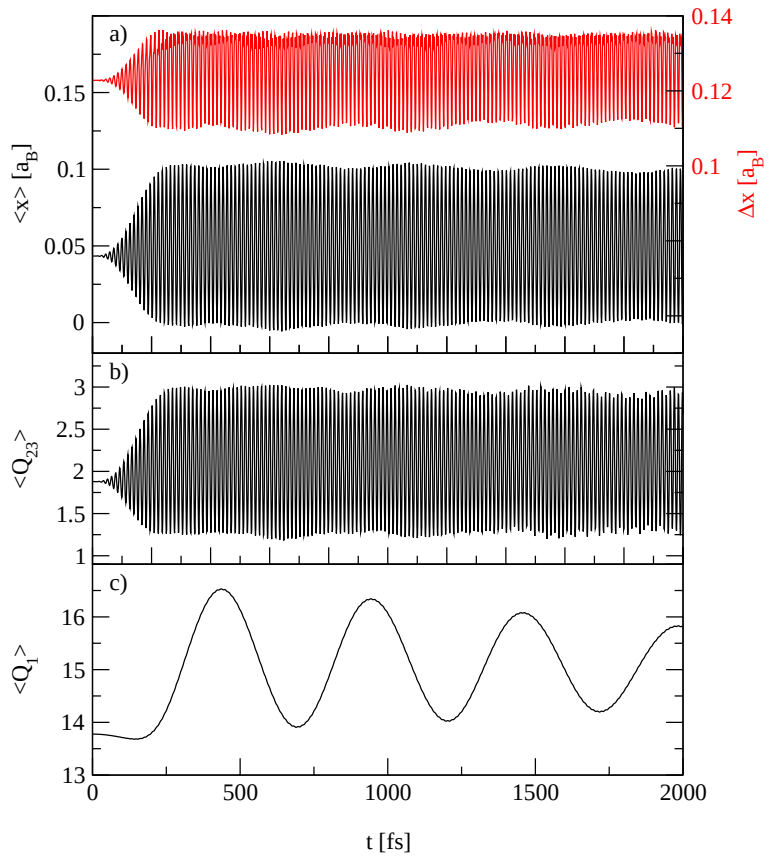

Figure 3.64: Same as in Fig. 3.62, only for the MCTDH calculation of the 9d model.

populations of all orbitals present have to be calculated, which is given by the eigenvalues of the above operator. If the largest resulting population is larger than a threshold value, one can assume that more orbitals are needed. This threshold is dependent on the system and on the quantity one wants to calculate, but normally a value below 0.1% population in the least important orbital can be considered safe. The development of the NOP for the combined mode (x, ν_{23}) is plotted in Fig. 3.63 for the whole propagation. One can see, that the seven orbitals provided for this mode are quite sufficient for the initial state, but for longer propagation times even the lowest orbital approaches a value close to 0.1% occupation. This shows, that for longer propagations more and more SPFs are needed, to treat the interactions between the modes correctly.

The mode dynamics, driven by the laser field, for this setup is presented in Fig. 3.64, this time for an interval up to 2 ps. Again the results do not differ much from the 3d or 9d TDH plots, with two exceptions. The first is, that now the modulation of $\langle x \rangle$ by the dynamics of $\langle q_1 \rangle$, which has already been seen in the 3d model, can be seen even more clearly. The other is the fact, that after the 2 ps propagation, one can clearly see a decay in the amplitude of the $\langle q_1 \rangle$ oscillations. As both these effects have not been seen

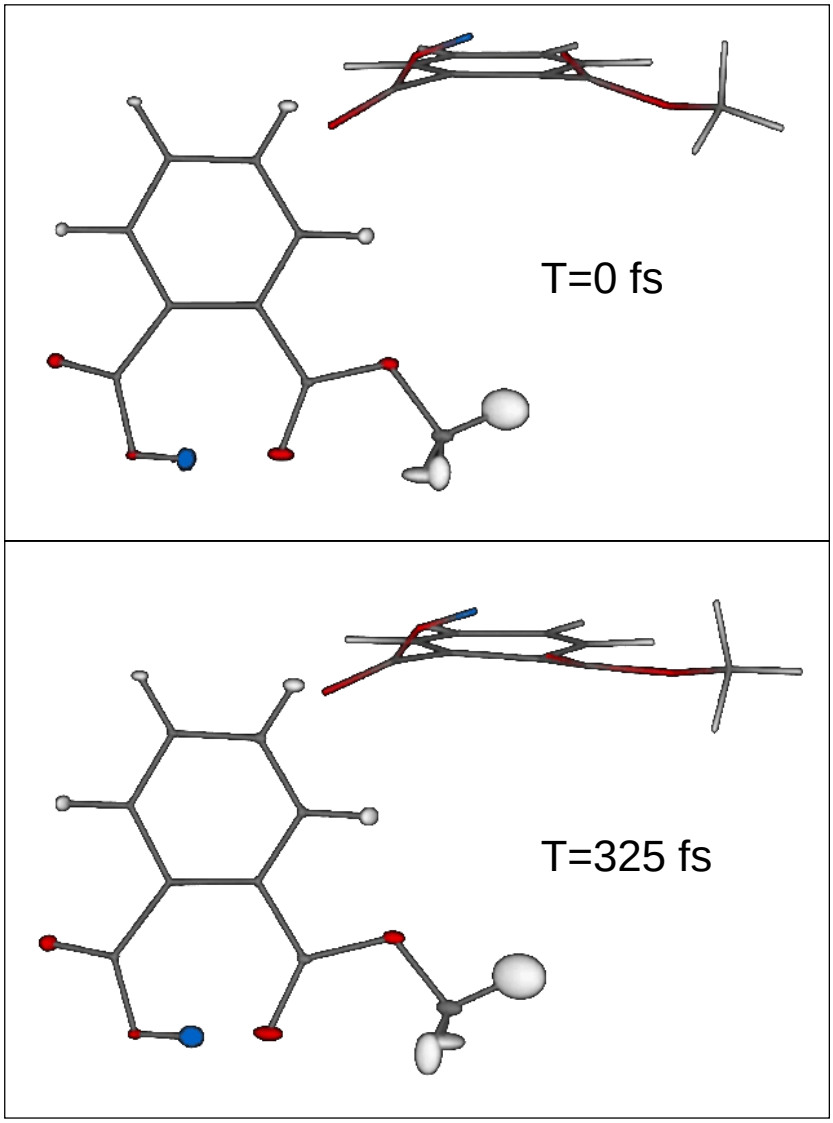

Figure 3.65: Two snapshots of the molecular scaffold for the 9d model, at $t = 0\,\mathrm{fs}$ (top) and $t = 325\,\mathrm{fs}$ (bottom). In these pictures, the variance of the MCTDH functions along the normal modes is translated back to the Cartesian coordinates of the scaffold in the form of the different axis lengths for the ellipsoids representing the scaffold atoms. (Figures curtesy of M. Dahlmann and C. Salzmann.)

in the 9d TDH calculation, using exactly the same CRS Hamiltonian, these are obviously multiconfiguration effects, which are neglected by the approximations made in TDH. The displacements along the normal modes can be translated back to Cartesian coordinates to visualize the scaffold movement caused by the laser pulse. Two snapshots of this movement are shown in Fig. 3.65. In these pictures, not only the position of the scaffold atoms is transformed back from the normal mode picture, but also the variance for each mode is translated back to cartesian coordinates (Eq. (2.36)).

$$\Delta\mathbf{x} = \mathbf{m}^{-1/2}\mathbf{U}\,\Delta\mathbf{q} \tag{3.22}$$

This is only an approximation, as the orientation of the variance is lost due to the fact that the rotations and translation are not contained in the normal modes. Therefore one has to define an arbitrary coordinate system, wihch will then form the different axes of the ellipsoids used to represent the atoms. In these one sees, that the very low frequency mode ν_1 is responsible for the very large variance in the location of the hydrogens in the ester group, i.e. the scaffold is very "floppy" in this region, resulting in widely spread ot wavepackets. This can also be seen in the time evolution of the system. After 325 fs the ester group shows significant rotations, which are well visible in the wireframe edge-on view in the upper right of the panels. This is the effect of the slow oscillations in the mode ν_1, shown in Fig. 3.64.

After the analysis of the mode expectation values a more detailed view of the dynamics is provided by inspection of the populations of the zeroth-order states and the energies of the uncoupled vibrationally diabatic 1d potentials of the Hamiltonian. These values are calculated for the potentials $V_{aa}^{(n)}(q_n)$, as given in Eq. (3.20) for the eight normal modes of the system, neglecting the couplings. For the energies, only the potentials for the ground state of the OD mode are considered, i.e. only the expectation values $\langle\Psi(t)|\,\hat{\mathbf{t}}_n + V_{00}^{(n)}(q_n)\,|\Psi(t)\rangle$ are calculated. The overlap with the zero order states also takes into account the change of the potential when doing the transition $\nu_{\mathrm{OD}} = 0 \rightarrow 1$, so that the populations are calculated for states of the form

$$\Psi_{(a)i_1\ldots i_n}(x, q_1, \ldots, q_f, t) = \psi_a \prod_{n=1}^{f} \varphi_n^{(a)i}(q_n, t) = |a\rangle \prod_i \left|n_i^{(a)}\right\rangle, \tag{3.23}$$

where ψ_a is an eigenstate in the calculated 1d potential of PMME, and $\varphi_n^{(a)i}$ is the i^{th} eigenstate in the potential $V_{aa}(q_n)$, generated by the function in the reference potential for mode q_n. The values for the populations then are calculated via

$$P_{(a)i_1\ldots i_n}(t) = \left|\left\langle\Psi_{(a)i_1\ldots i_n}(x, q_1, \ldots, q_f, t)|\Psi(t)\right\rangle\right|^2. \tag{3.24}$$

The definition of these zero order states allows one to address the substrate mode interstate and intrastate coupling. The strength of these effects can be assessed by estimating the matrix elements $\left\langle\Psi_{(a)i_1\ldots i_n}\right|\hat{\mathbf{H}}\left|\Psi_{(b)i_1\ldots i_n}\right\rangle$ for the interstate and $\left\langle\Psi_{(a)i_1\ldots i_n}\right|\hat{\mathbf{H}}\left|\Psi_{(a)i_1\ldots i_n}\right\rangle$

for the intrastate transitions. If one neglects the rather small change in frequency for the moment, i.e. sets $\langle a| K_{nn}(x) |a\rangle = \langle b| K_{nn}(x) |b\rangle = \omega_n$, the matrix elements can be estimated as

$$\begin{aligned}\langle a| \prod_i \left\langle n_i^{(a)}\right| \hat{\mathbf{H}} \prod_i \left|m_i^{(b)}\right\rangle |b\rangle = \\ -\sum_k \langle f_k\rangle_{ab} \left\langle n_k^{(a)}\right| q_k \left|m_k^{(b)}\right\rangle \prod_{i\neq k} \delta_{n_i m_i} \\ +\frac{1}{2}\sum_{k,l} \langle K_{kl}\rangle_{ab} \left\langle n_k^{(a)}\right| q_k \left|m_k^{(b)}\right\rangle \left\langle n_l^{(a)}\right| q_l \left|m_l^{(b)}\right\rangle \prod_{i\neq k,l} \delta_{n_i m_i}\end{aligned} \tag{3.25}$$

and

$$\begin{aligned}\langle a| \prod_i \left\langle n_i^{(a)}\right| \hat{\mathbf{H}} \prod_i \left|m_i^{(b)}\right\rangle |a\rangle = \\ E_a \prod_i \delta_{n_i m_i} + \sum_k \delta_{n_k m_k}\epsilon_k \\ -\sum_k \langle f_k\rangle_{aa} \left\langle n_k^{(a)}\right| q_k \left|m_k^{(b)}\right\rangle \prod_{i\neq k} \delta_{n_i m_i} \\ +\frac{1}{2}\sum_{k,l} \langle K_{kl}\rangle_{aa} \left\langle n_k^{(a)}\right| q_k \left|m_k^{(b)}\right\rangle \left\langle n_l^{(a)}\right| q_l \left|m_l^{(b)}\right\rangle \prod_{i\neq k,l} \delta_{n_i m_i}.\end{aligned} \tag{3.26}$$

Within this approximation, the matrix elements for $\left\langle n_k^{(a)}\right| q_k \left|m_k^{(b)}\right\rangle$ can be estimated by

$$\begin{aligned}\left\langle n_k^{(a)}\right| q_k \left|m_k^{(b)}\right\rangle &= \sum_{l_k} \sqrt{\frac{\hbar}{2\omega_k}}\,\mathrm{FC}(n_k, l_k, \Delta g_{ab}) \\ &\quad\times \left(\sqrt{m_k+1}\delta_{l_k,m_k+1} + \sqrt{m_k}\delta_{l_k,m_k-1} - 2g_k(a)\delta_{l_k,m_k}\right).\end{aligned} \tag{3.27}$$

In this equations, the dimensionless shift between the VD potential curves is introduced as $g_n(a) = -q_n^{(a)}\sqrt{\omega_n/2\hbar}$, with $q_n^{(a)}$ being the shifted minimum position in state $|a\rangle$. Further, $\mathrm{FC}(n_k, l_k, \Delta g_{ab})$ is the Franck-Condon overlap integral between two harmonic oscillators displaced by $\Delta g_{ab} = g_n(a) - g_n(b)$ with respect to each other.

These estimates show, that the coupling between excitations of the O–D vibration and excitations within the normal modes is determined by constants of the form $\langle a| K_{mn}(x) |b\rangle$ and $\langle a| f_n(x) |b\rangle$. As the shift of the minimum positions of the VD potentials is rather small, the Franck-Condon integral takes on its maximum value for $M_n = K_n$. This implies that the coupling causes mostly transitions with $\Delta N = \pm 1$. The forces and coupling constants for the modes of the 3d model, ν_1 and ν_{23} are given in Table 3.10. From these one can see, that the strongest effect is generated by the constant $\langle \psi_0| f_{23}(x) |\psi_1\rangle$, which is linear in q_{23}. All other coefficients are at least one order of magnitude lower and only influence the dynamics slightly.

Fig. 3.66 shows the populations $P_{a,i_{23},i_{1}\ldots}$ for various VD zeroth-order states. Here the subscript labels the VD state $|a\rangle$ and the respective vibrational quantum numbers of the

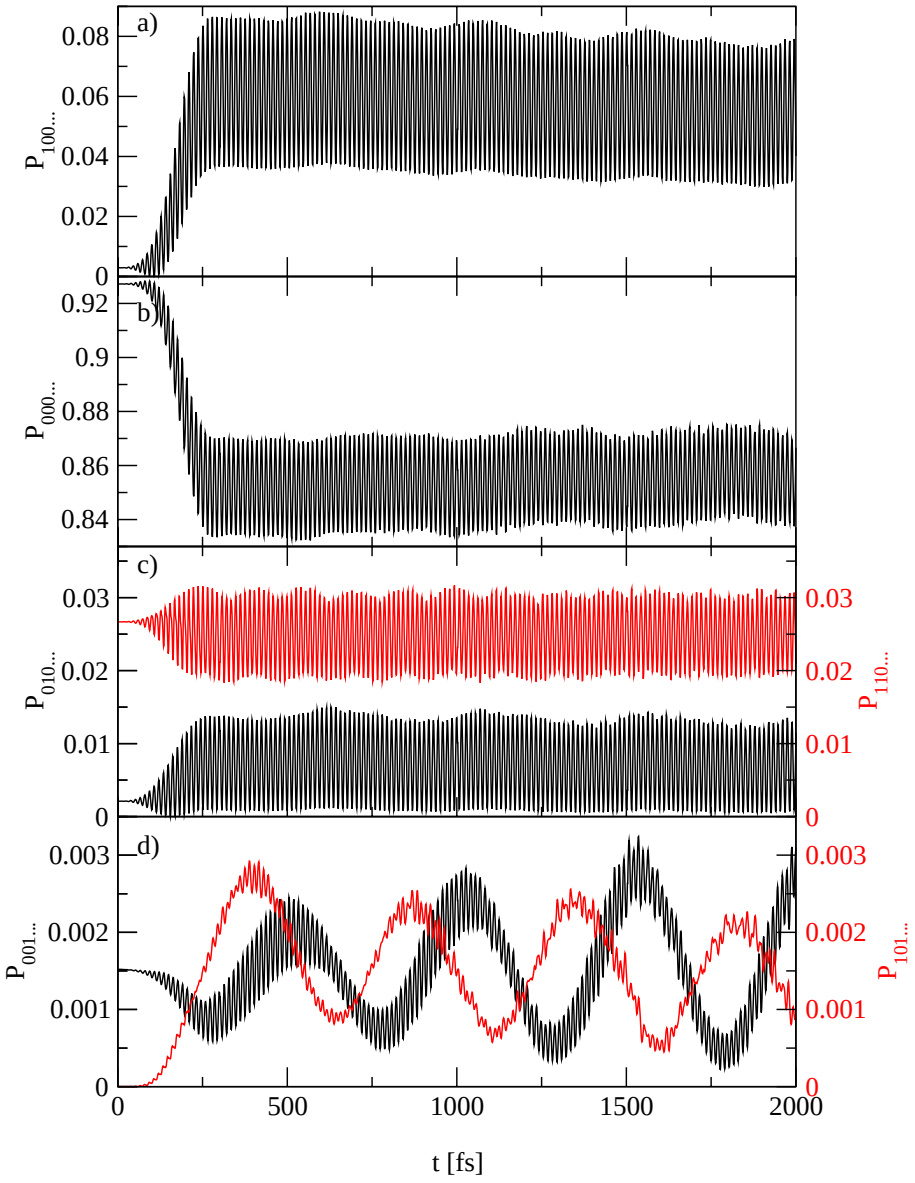

Figure 3.66: Time evolution of the populations $P_{(a)i_1\ldots i_n}(t)$ of vibrational states in the VD potentials $V_{aa}(\{q_n\})$, under the influence of the laser plotted in Fig. 3.61. In panel **a)** the first exited state of the reaction coordinate ($a = 1$, $i_1 = \cdots = i_n = 0$) and in **b)** the corresponding ground state ($a = 0$, $i_1 = \cdots = i_n = 0$) is plotted. Panel **c)** plots the first excited state along the strongly coupled mode ν_{23} for $a = 0$ (black) and $a = 1$ (red). The same for mode ν_1 is shown in panel **d)**.

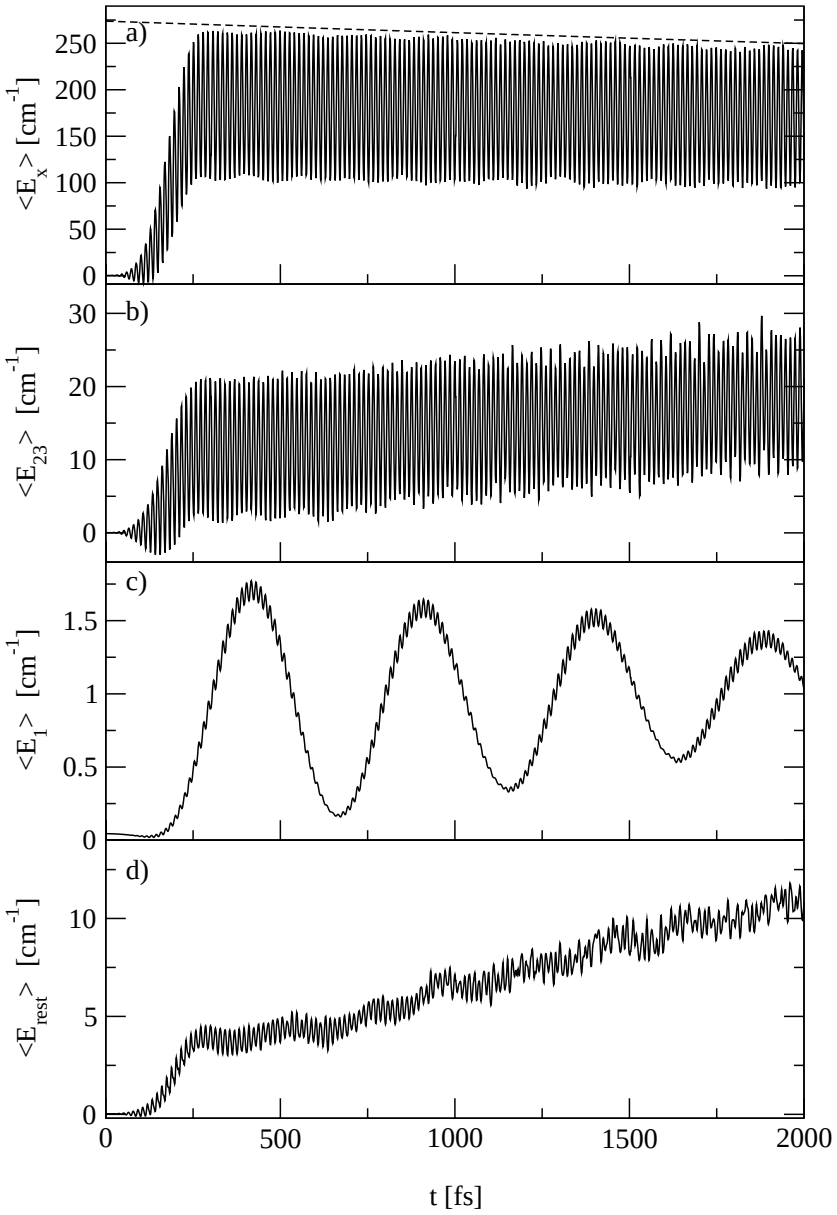

Figure 3.67: Expectation values for the uncoupled single mode Hamiltonians according to Eq. (3.20), under the influence of the laser plotted in Fig. 3.61. Plotted is the difference to the initial value of the energy at time zero, in cm^{-1}. In the upper panel **a)**, the energy of the reaction coordinate is plotted. The dashed line shows an exponential decay with $\tau \approx 20\,\mathrm{ps}$. The other panels show: **b)** mode ν_{23}, **c)** mode ν_1 and **d)** the six remaining modes.

$\bullet$	$\langle\psi_0\vert \bullet \vert\psi_0\rangle$	$\langle\psi_1\vert \bullet \vert\psi_1\rangle$	$\langle\psi_0\vert f(x) \vert\psi_1\rangle$
$K_{1,1}$	$8.69{\cdot}10^{-8}$	$9.15{\cdot}10^{-8}$	$6.37{\cdot}10^{-10}$
f_1	$8.82{\cdot}10^{-7}$	$2.50{\cdot}10^{-6}$	$-1.66{\cdot}10^{-6}$
$K_{23,23}$	$2.01{\cdot}10^{-5}$	$1.95{\cdot}10^{-5}$	$2.12{\cdot}10^{-6}$
f_{23}	$7.71{\cdot}10^{-6}$	$2.15{\cdot}10^{-5}$	$-2.00{\cdot}10^{-4}$
$K_{1,23}$	$-2.82{\cdot}10^{-8}$	$-2.79{\cdot}10^{-8}$	$-1.62{\cdot}10^{-8}$

Table 3.10: The expectation values of the forces and the second derivative matrix elements, giving the coupling constants for eq. (3.25) and (3.26). All values are given in atomic units.

mode. The quantum numbers of the other substrate modes are taken to be zero. In the upper two panels **a)** and **b)** of this Figure, the population dynamics of the reaction coordinate for $\nu_{\mathrm{OD}} = 1$ and $\nu_{\mathrm{OD}} = 0$, with the other VD modes in their vibrational ground states. Here, the state coupling is reflected in the rapid out-of-phase oscillations of $P_{000\ldots}$ and $P_{100\ldots}$. Simultaneously, the state $\Psi_{010\ldots}$ is excited, for example, via a $\Delta N_{23} = 1$ transition as shown in Fig. 3.66c, such that its fast oscillations are out-of-phase with the dynamics of $P_{100\ldots}$. In contrast to this, the population $P_{110\ldots}$ shows, that the zero order states are only an approximation, as this state is already slightly populated in the ground state of the total wavefunction. Compared to $P_{010\ldots}$, this value only oscillates around its starting value, and does not show an overall increase via excitation.

The populations of the states $\Psi_{001\ldots}$ and $\Psi_{101\ldots}$ (corresponding to ν_1), as they are shown in Fig. 3.66d, are one order of magnitude below the one connected to ν_{23} discussed above. Their behavior follows the pattern already seen in the mode expectation values in Fig. 3.64. While the strongly (via $\langle f_{23}\rangle$) coupled mode ν_{23} oscillates at the driving frequency of the OD bond, the vibrations of ν_1 are only slightly modulated by this, while the main dynamics takes place at the low frequency of this mode. At the same time, one can observe a decay of the maximum amplitude for the population $P_{101\ldots}$, while at the same time $P_{001\ldots}$ is increasing. This shows the decay of the first excited state of the reaction coordinate back to the ground state. The decay is also visible in panel **a)**, which shows a slow decay of the population. At the same time, $P_{001\ldots}$ is increasing. As both processes take place at a different rate, with the decay of $P_{100\ldots}$ being faster, one has an indication for a complex pattern of vibrational energy redistribution into other modes. For this, the substrate mode-mode coupling terms are of importance as well. Additionally, the influence of the remaining modes on the OD dynamics leads to low-frequency modulations of the populations, which can also be seen in Fig. 3.66. In principle, in this representation all substrate modes are vibrationally excited in both VD states. This obscures a clear interpretation of the low-frequency modulation in, for instance, $P_{100\ldots}$. It should be noted that in terms of

the dynamics the population of these vibrationally excited VD states reflect nuclear wave packet motion in the different VD potentials of Fig. 3.57. However, the present situation appears to be more complex as compared to the case of simple vibronic excitation due to the relatively strong interstate coupling.

Further support for the IVR processes taking place in this mode can be seen from the behavior of the expectation values $\langle E_{i=x,n} \rangle$ of the uncoupled Hamiltonians defined by Eq. (3.20). In Fig. 3.67 this behavior is plotted for the reaction coordinate, the two modes ν_{23} and ν_1 and the sum of all the remaining modes. The energies are plotted as their difference from the initial value in units of cm^{-1}. For the reaction coordinate $\langle E_x \rangle$ in Fig. 3.67a, one can see an initial increase due to laser excitation and subsequent slow decay. The fast oscillations are again due to the coupling to the ν_{23} mode as can be seen by comparison with $\langle E_{23} \rangle$ in Fig. 3.67b. The slower modulations apparent in $\langle E_x \rangle$ and $\langle E_{23} \rangle$ are mostly due to the interaction with the ν_1 mode, whose energy $\langle E_1 \rangle$ is plotted in Fig. 3.67c. This mode again is not influenced strongly by the fast oscillation of the reaction coordinate, but follows its own vibration period of about $t_1 = 500\,\mathrm{fs}$. The process of IVR from the reaction mode to the other modes can be seen from the decay of $\langle E_x \rangle$ and the parallel increase of $\langle E_{23} \rangle$ and the total energy of all the remaining modes $\langle E_{\mathrm{rest}} \rangle$, plotted in Fig. 3.67d. The dashed line in Fig. 3.67a shows an exponential function with a decay time of $\tau = 20\,\mathrm{ps}$, which is the time–constant for the IVR processes in the isolated 9d model. Most of this energy flows into the mode ν_{23}, while the rest is distributed over all other vibrations of the scaffold.

What can also be seen from the energy expectation values of the energy, especially from $\langle E_{23} \rangle$, is the fact that the MCTDH algorithm starts to decrease in accuracy after the first picosecond. While a part of the "ragged edge" of the energy oscillations is due to the small number of sample points, a part of this is caused by the limited accuracy of the numerics and the only approximate treatment of the intermode couplings. Calculations for a longer time would therefore need additional SPFs to increase the quality of the results.

19d calculation

The 19d model for the PMME molecule is an extension of the 9d model in the previous section. To the nine modes, combined in the same way with the same number of SPFs as in the smaller model, additional 10 modes (given in Table 3.8) are included in TDH approximation, i.e. uncoupled and with one SPF per mode. This means that the number of configurations in the MCTDH calculation remains at $N = 4375$, as in the 9d case. The initial, ground state wavefunction for the dynamics are again generated by a relaxation method. The resulting mode expectation values are given in Table 3.9. Following the trend of the previous results, the zero point energy is again higher, leading to a higher offset in $\langle x \rangle$ and therefore slightly higher displacements in all other modes $\langle q_i \rangle$.

The laser pulse used for the 19d model has the same parameters as that for the 9d one, with the exception of the frequency, which again is slightly shifted to $\Omega/2\pi c = 2355\,\mathrm{cm}^{-1}$.

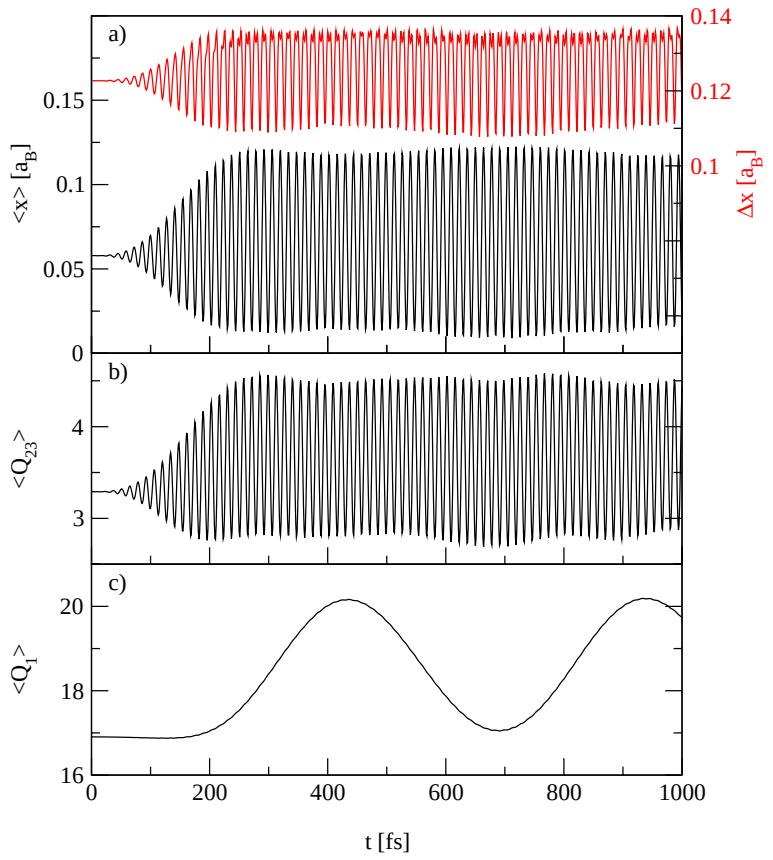

Figure 3.68: Same as in Fig. 3.61 and Fig. 3.64, only for the 19d model.

The results for the propagation are plotted in Figs. 3.68 (for the mode expectation values), 3.69 (for the zero order state populations) and 3.70 for the mode energy expectation values. The plots show no additional effects of the increased number of modes, beyond the trends already identified in the previous calculations. The most prominent change is that the higher energy in the anharmonic couplings again lead to a larger amplitude of the high frequency oscillations coupled to the reaction coordinate. On top of that, no qualitative change of the dynamics could be observed.

This shows, that the 9d model already includes all the important modes, which influence the dynamics of the molecular vibrations. All further modes, which could be included, are too weakly coupled and do not change the result significantly. Additionally, all modes beyond the ones of the 9d model can only be added efficiently in the TDH approach, as the numerical effort of the MCTDH method is limited by the number of configurations resulting from a high number of SPFs in multiple dimensions. Even with this simplification, this larger model is at the limit of the capabilities of the available computers. As no new effect are to be expected on this time scale, the calculations were not extended to a converged MCTDH basis set for the 19d Hamiltonian.

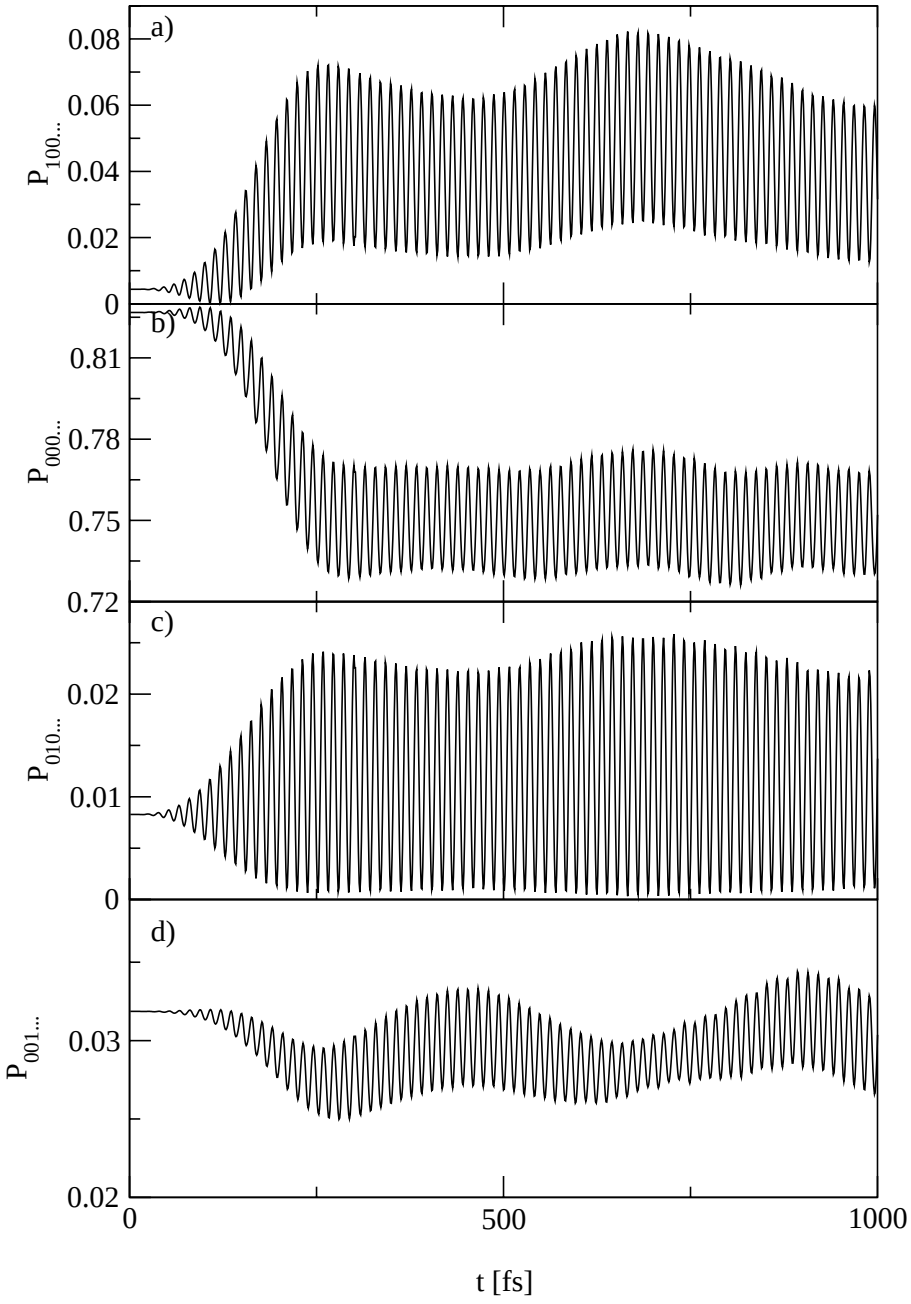

Figure 3.69: Same as in Fig. 3.66, only for the 19d model.

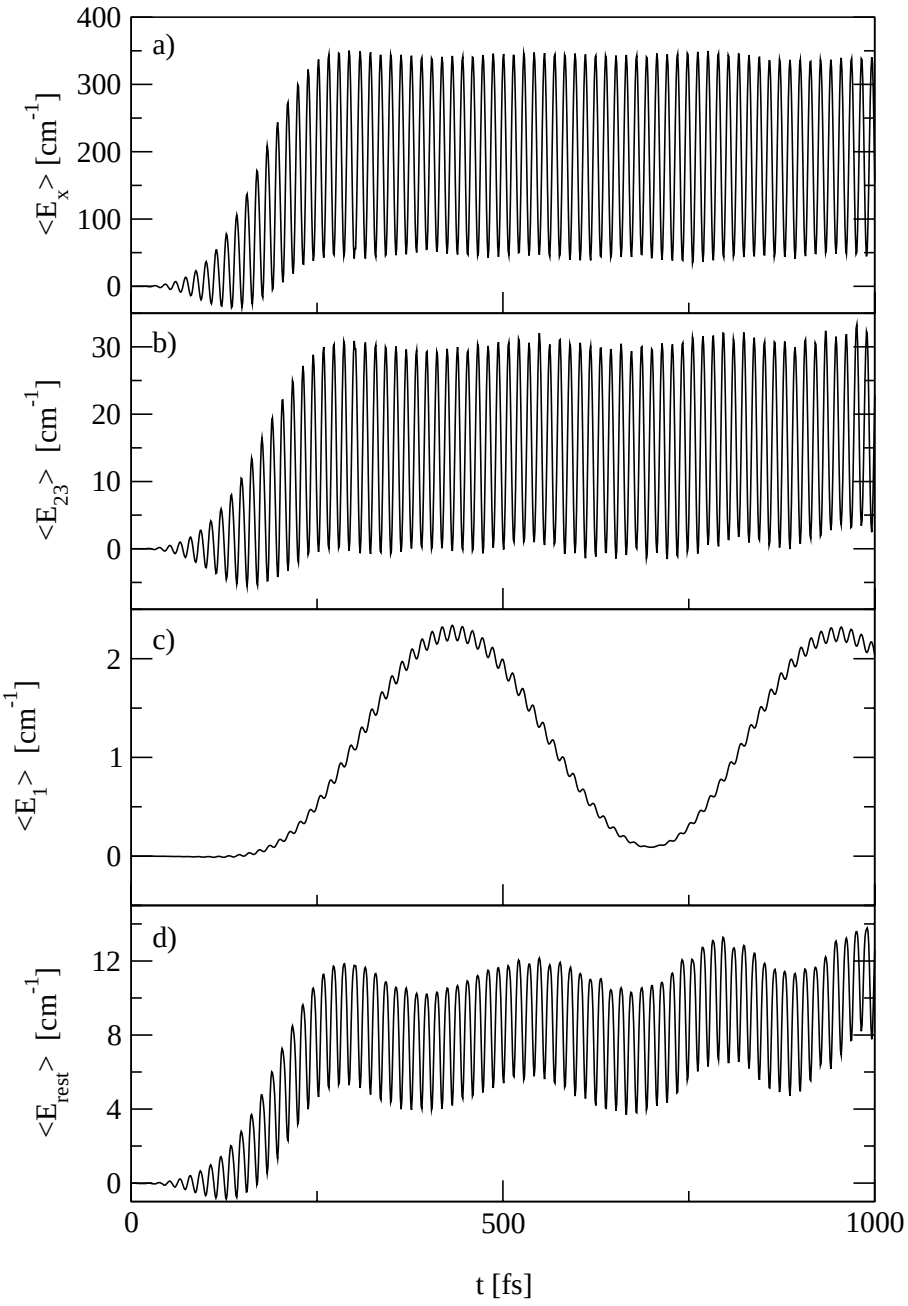

Figure 3.70: Same as in Fig. 3.67, only for the 19d model.

3.3.5 Molecular Dynamics Calculations for PMME in Solution

The energy and population relaxation times found with the MCTDH simulations in the last section are much longer than the experimentally observed decay of $\nu_{\mathrm{OD}} = 1 \rightarrow 0$ with a time constant of $T_1 \approx 400\,\mathrm{fs}$. This points toward a strong influence of the solvent on the mode relaxation of the PMME molecule. To get an idea about the effects generated by a solvent shell, a molecular dynamics (MD) calculation is made for a PMME molecule in solution. A short overview over some aspect of MD simulations is given in Appendix C, but a more detailed review can be found in the literature [141, 142]. For most of the following calculations, the Gromacs program package (V2.0) [143, 144] has been used.

To determine the interaction of an external solvent on the relaxation processes inside a molecule, the theory of linear response [61] has to be used. With this, one is able to relate the classical forces acting on parts of the molecule to the reservoir correlation functions of the reduced density matrix theory, presented in Section 2.3.3, page 37. This correlation functions are directly connected to the effective population relaxation time T_1, describing the exponential decay constant for the dissipation of energy from a harmonic oscillator to the bath [98, 145, 146]. It should be sufficient to study the harmonic approximation, as the CRS Hamiltonian in this work consists only of a nearly harmonic (at least near the minimum) reaction potential, and a set of harmonic normal modes. For this setup, the relaxation time T_1 for an oscillator of frequency ω_0 can be calculated from

$$\frac{1}{T_1} = \frac{\tanh(\beta\hbar\omega_0/2)}{\beta\hbar\omega_0/2}\frac{\zeta(\omega)}{2}, \tag{3.28}$$

with $\beta = 1/k_B T$ and the friction spectrum

$$\zeta(\omega) = 2\int_0^\infty dt\,\zeta(t)cos(\omega t). \tag{3.29}$$

The friction spectrum is the Fourier transform of the time dependent friction, defined by

$$\zeta(t) = \frac{\beta}{\mu}\left\langle F(t)F(0)\right\rangle, \tag{3.30}$$

with the μ the mass connected to the coordinate and $\langle F(t)F(0)\rangle$ the classical correlation function of the force along the relevant coordinate [98]. This force–force autocorrelation function is the data, which can be provided by a classical MD simulation. As explained in Appendix C, the forces on each particle have to be calculated for each MD step anyway, so to generate the relevant autocorrelation function, one just has to have direct access to this data, and project the resulting force on the desired effective coordinate (i.e. a molecular bond or a more complex normal mode).

As a solvent for the PMME molecule CCl_4 was chosen, as this molecule is a bit easier to handle than C_2Cl_4, which was used in the experiment. The MD parameters for this molecule are the default values from the Gromacs program and the literature [147, 148].

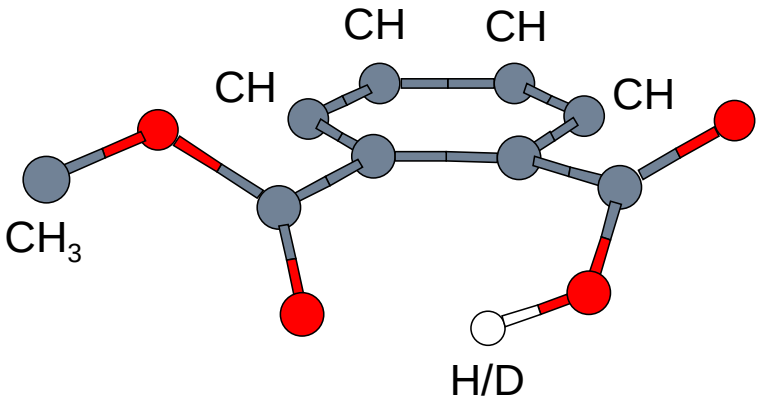

Figure 3.71: The PMME model for the MD simulation. All hydrogen atoms, except the one responsible for the hydrogen bond, are removed and included in combined heavy atom centers.

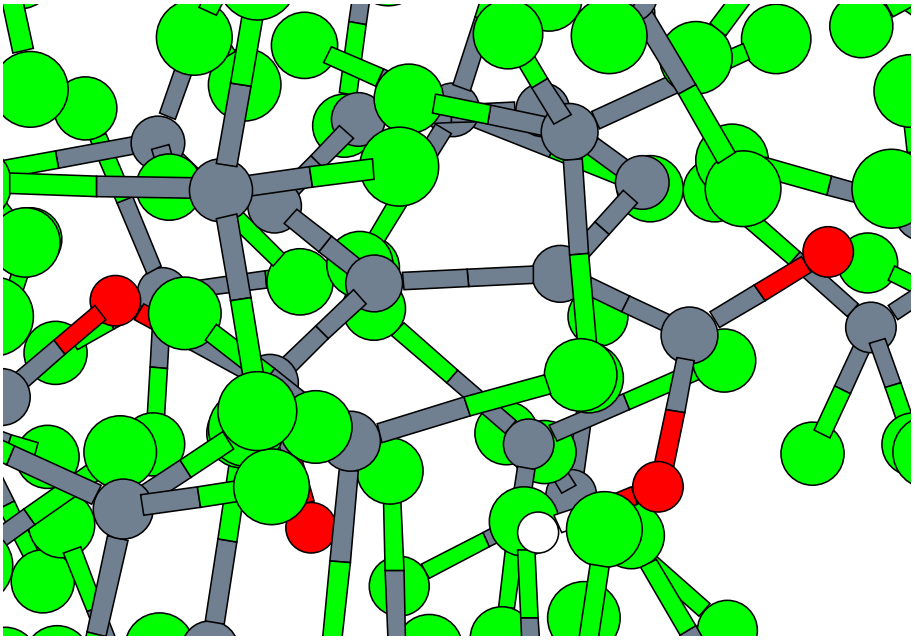

Figure 3.72: PMME surrounded by the CCl_4 solvent molecules. Ones can see, that the solvent is packed extremely tight around the solute molecule.

Furthermore, the usual procedure for a MD simulation is to combine all H atoms not directly relevant to the calculation with neighboring heavy atoms to so called combined centers, to avoid the small time-steps needed for the propagation of the light particles. The PMME model resulting from this approximation is plotted in Fig. 3.71, where only the hydrogen relevant for the intermolecular hydrogen bond is left uncombined. This simplified PMME molecule is set into a cubic box with 724 CCl_4 molecules. The size of the box is set to an edge length of 5Å, with periodic boundary conditions. This reproduces the density of CCl_4 from the literature [149], and produces a solvent environment large enough to result in several solvent shells around the PMME molecule. The temperature of the bath is set to a value of 300 K. To implement the linear response theory given above, the molecular geometry has to be kept fixed during the calculations. While this is normally done by defining a set of constraints, which keep all the bonds and angles in the molecule fixed, but allow rotation and translation, in this calculation simply the whole PMME molecule is frozen in place. This prohibits the rotation, but removes the effort necessary to generate a suitable set of constraints, which can be difficult for systems containing planar rings. In these systems, a constraint method can also lead to numerical instabilities, which are avoided by fixing the PMME completely. The effects of this simplification should be rather small, as the solvent is very dense, and would not allow large translations or rotations anyway.

In addition to the standard MD procedure of using combined atoms for the light hydrogens, the parameters for the Lennard–Jones interaction potential for PMME is set to the standard values provided by Gromacs, which in turn are taken from the GROMOS molecular modeling package [147]. In addition to the LJ interaction, each atom in the molecule carries a partial charge, which can result in Coulomb interaction with the solvent. The partial charges in PMME are calculated within standard quantum chemistry already done for the system. The default method of GAUSSIAN to calculate the charges is the Mulliken method [134]. This approach is easy to calculate, but the results are often not accurate enough for MD simulations, as the strong Coulomb forces often dominate the dynamics, and therefore require highly precise charges. Therefore, the partial charges of a molecule to be treated with MD simulations should be calculated via a more refined method. What is normally used is called CHELP (Charges via Electrostatic Potential) [150], which fits the potential generated by a set of point charges to the one generated by the electronic wavefunctions. In this specific simulation, the partial charges do not play any role, as the solvent is not polar, i.e. all atoms of the CCl_4 molecule carry a charge of zero. Because only a single PMME molecule is used, and the atoms within a single molecule are only allowed to interact via bond forces, there is no Coulomb interaction in the whole system of PMME and solvent. A sample input for Gromacs can be found in Appendix D.3.

The simulation with these parameters does not allow a good representation of the forces acting on the single proton in the reduced PMME model. For non polar environments there is nearly no interaction between the proton and the surrounding molecules, as the LJ forces

between the hydrogen and the solvent are zero. In further analysis of the model it turns out, that the frequency of the O–H vibration is much to high for the coupling to the solvent to lead to a relaxation time on the order of 2 ps. Therefore the relaxation observed in the experiment has to be explained with processes involving other normal modes and the T_1 time of the O–H coordinate is of no direct interest.

What can be calculated with small errors from the simulation, is the force acting along the normal mode coordinates of the two most relevant modes, ν_1 and ν_{23}. The error results from the simplification with the combined atoms, which means that the forces calculated for the MD simulations do not act on the same scaffold, as the one defined by the normal modes. But as the displacement vectors on the hydrogens are relatively small for the two modes considered, this should only produce a small offset from the actual value.

To produce a useful force–force autocorrelation function, it is necessary to average over the results of several MD runs with independent starting conditions. At the same time, the total length of the runs has to be long enough to result in a "clean" Fourier transform, i.e. one where the true vibrational effects of the solvent are larger than the numerical noise, which always accompanies the statistical forces of a MD simulation. A longer autocorrelation function also increases the accuracy of the discrete Fourier transform. The following calculations are based on 30 MD runs with a length of 30 ps each. For each of these runs a new set of random solvent velocities, consistent with a temperature of 300 K is generated. Before the MD simulation for the autocorrelation function is started, the configuration is equilibrated for five additional ps, to guarantee a statistical distribution of the solvent molecules.

The classical MD forces acting on the PMME scaffold shown in Fig. 3.71 are then extracted for each time step of the simulation, and projected on the normal mode vectors for ν_1 and ν_{23}. For this projection the forces on the hydrogens not included in the MD model are set to zero. The autocorrelation function of this force, averaged over all 30 runs is presented in the upper panel of Fig. 3.73. The friction spectrum resulting from these functions, according to Eq. (3.28), is presented in the lower panel of the same Figure. In this plot one can see, that the non–polar solvent produces nearly featureless spectrum, without any significant peaks. The oscillations visible in the autocorrelation function result in the numerical noise visible in the spectrum below $100\,\mathrm{cm}^{-1}$. The other features visible are several small peaks around $700\,\mathrm{cm}^{-1}$. These correspond to the principal C–Cl vibrations of the classical CCl_4 model. According to this results, the T_1 time of the ν_{23} mode, which samples the spectrum at $985\,\mathrm{cm}^{-1}$, is on the order of ~ 100 ps, i.e. the mode couples only weakly to the solvent at its natural frequency. In contrast to this, ν_1 samples its friction spectrum at $68\,\mathrm{cm}^{-1}$. Therefore, even though its spectrum is nearly identical to the one for ν_{23}, its T_1 time is on the order of ~ 2 ps, which is a little too long compared to the experimental value of ~ 500 fs. To get better results for this time, it would be necessary to average over even more MD runs, as the frequency of the ν_1 mode falls in the region of the strong numerical noise at the lower end of the spectrum.

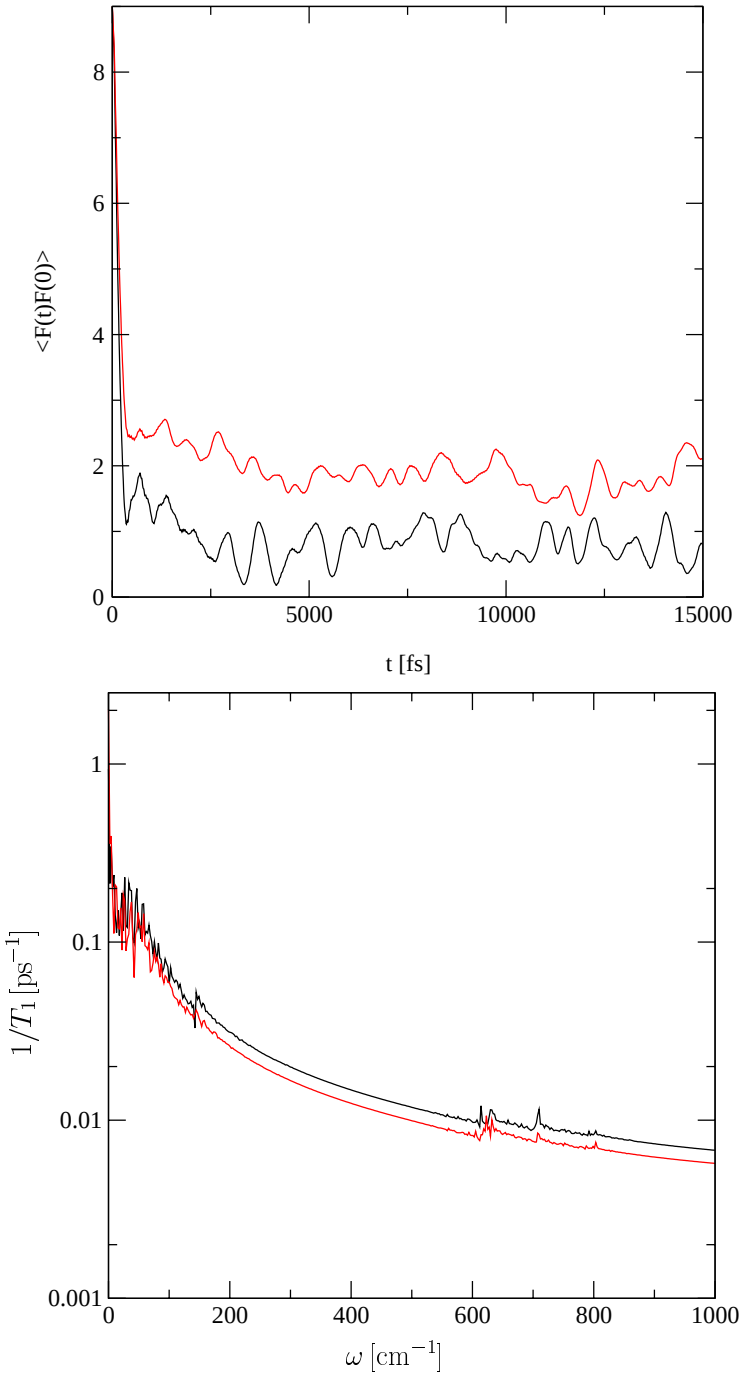

Figure 3.73: The upper panel shows the force–force autocorrelation function of the solvent, exerted on the normal modes ν_1 (black) and ν_{23} (red) of PMME. In the lower panel the spectrum of these functions is shown, scaled to the inverse lifetime [ps^{-1}] at the relevant frequency.

3.3.6 Conclusion

In this section, for the first time extensive simulations for a "real life" molecule using the CRS Hamiltonian were presented. To build the Hamiltonian, only data from *ab initio* simulations has been used, and the dynamics of the system has been calculated in the MCTDH method. The simulation of the Hamiltonian was implemented for models with different numbers of dimensions, to test the behavior of a multidimensional CRS Hamiltonian and the performance of the MCTDH method. The approach to build the Hamiltonian was simplified by selecting only a single reaction coordinate, so that only along this straight one dimensional line the second derivative matrix of the molecular system had to be determined. This simplification makes it possible to calculate only on the order of 10 *ab initio* points to define the total reaction potential and the normal modes for it. This is in contrast to the nearly 200 points necessary for a good 2d potential in the HIP molecule. At the same time, the quantum chemistry showed, that the PMME molecule has significantly different geometries and energies, when treated with DFT methods, compared to the MP2 calculations. Therefore the computationally much cheaper DFT method cannot be used to build the CRS Hamiltonian in this case, and the more accurate, but much more demanding MP2 approach had to be used. As each point on the reaction surface took about one day to calculate on an Origin3000 computer (R14000 CPUs), one can quickly see, that the one dimensional limit is the only way of getting results for this kind of system (i.e. one, where the DFT methods are not reliable) in a reasonable time.

The second derivative matrices of the molecular potential at the points on the reaction surface then give all the necessary data to build the CRS Hamiltonian from the harmonic normal modes of the molecular scaffold. This form of the Hamiltonian, as already presented for the HIP molecule, allows the treatment of the PMME molecule in nearly full dimensionality. The only degrees of freedom, which are neglected are the two coordinates of the hydrogen, which are kept fixed. It was shown in [151], that it is possible to treat this nearly full dimensional PMME model within the TDH approximation. This large number of dimensions cannot be handled by the more accurate MCTDH method, which was applied in this work. Therefore, it was necessary, to select from this set of normal modes the most important ones at each point of the reaction surface. These were selected by analysing the reorganization energy for the single modes at the potential points. This selection allows one, to reduce the dynamics again, from the full dimensional system, to one which only contains the most important modes, dominating the dynamics, thereby enabling one to study the model in reduced dimensionality, but increased numerical accuracy. Applying the MCTDH method to the reduced model with the most important modes produces results in an acceptable time, while the same approach would be prohibitively expensive for the full dimensional model. At the same time the TDH calculations for the 9d model showed, that most of the relaxation effects are only prominent in the multiconfiguration approach, i.e. the increased accuracy is necessary to model the IVR processes one is interested in. The largest model examined was the 19 dimensional one, which contains

almost the complete reorganization energy of the full CRS picture.

For these models of different dimensionality the dynamics after excitation with a laser pulse tuned to the transition frequency $\nu_{\mathrm{OD}} = 0 \rightarrow 1$ as well as the stationary IR spectrum was examined. From the stationary spectrum one could see that the CRS model with a fixed scaffold and only a 1d reaction coordinate does not reproduce the double peak structure seen at the OD vibration frequency in the experiment. This shows, that the limited CRS model cannot reproduce the effects of the proton dynamics completely, even though the normal modes add flexibility to the molecular scaffold. This probably means that additional effects may be generated by large amplitude motions of the scaffold or via a coupling to an overtone of the bending mode of the O–D bond. As this type of motion cannot be modeled with the limited computing power available, the study had to be limited to the effects visible in the present model.

However, this limited approach has several advantages over calculations using other potential surfaces, i.e. unrelaxed molecular potential. With the CRS Hamiltonian it is, at least locally, possible to generate a potential surface with full dimensionality, which allows the identification of the relevant degrees of freedom without prior knowledge about the normal modes of the molecule. The formalism of the Hamiltonian used is also well suited to the application of the efficient MCTDH method, as it is already written in a factorized form, and contains all the couplings in the potential energy operator.

As mentioned above, the combination of the CRS Hamiltonian with the MCTDH method allows one to study the molecule on different levels of accuracy (by including different numbers of normal modes) and to tailor the numerical effort for the calculations (by increasing or reducing the number of configurations in the MCTDH equations). In the calculations presented, vibrational wavepacket simulations after a laser excitation of the OD bond were made for 3d, 9d and 19d models. The most notable results of these simulations were the observation of the effects of the anharmonic coupling between the modes, which led to a modulation of the OD stretching vibration. The most notable can be seen on a time scale of about 500 fs, which corresponds to one of the low frequency normal modes, modulating the deuterium bond geometry. This is in accord with the experimental observation of coherent vibrational dynamics in this system (Fig. 3.55). Additionally it was shown, that in the MCTDH model the population excited by the laser pulse into the $\nu_{\mathrm{OD}} = 1$ state decays slowly back into the ground state $\nu_{\mathrm{OD}} = 0$. This effect was not observed in the TDH calculations made in this and previous works [151]. The decay time calculated for the 9d model is on the order of 20 ps, which is much longer than the experimentally observed time scale of $T_1 = 400$ fs. This result was not changed by including a further 10 modes for the 19d model. The additional modes were only included in the TDH limit, as the numerical effort to converge the 9d model was already very high. The calculation of the first 300 fs on this accuracy needed approximately 13:30h on a Pentium III with 866 MHz to obtain the numerically converged result. Including the additional 10 modes in the TDH limit increased this time to 67:00h on the same computer. This shows, that it is

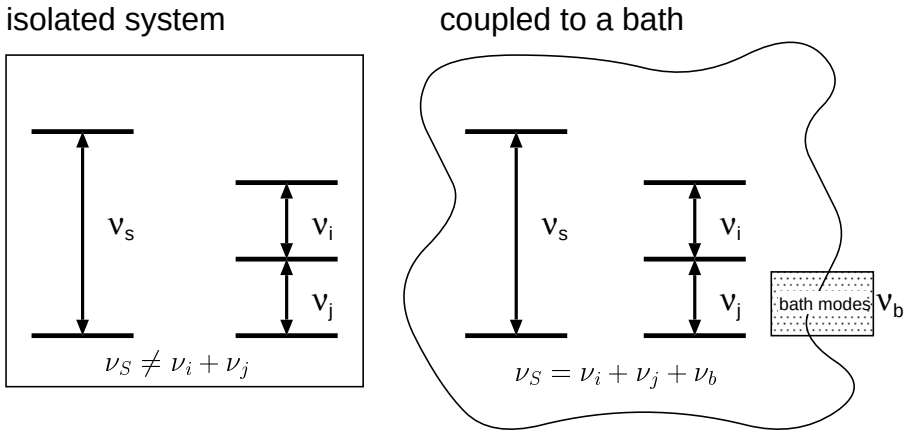

Figure 3.74: The fast decay of the experimentally observed oscillations can be explained by the coupling to the environment. In the left panel a system is shown in which the system frequency ν_s is not matched by the normal mode frequencies ν_i and ν_j. An exitation in the system cannot get easily rid of its energy in this case. If a bath is added to the picture, one has an additional continuous band of bath modes (shown on the right). Any energy mismatch between the system and the normal mode frequencies can now be compensated by a bath mode from this band, allowing a much faster relaxation.

unfeasible to obtain fully converged results for this model with the available hardware.

The fact that the inclusion of this 10 additional modes in TDH limit does not open visible new relaxation channels cannot be clearly attributed to a single cause. The numerical approximations of the model do probably not allow for a relaxation, as was observed in the 9d TDH simulations as compared to the MCTDH ones. Another reason could simply be that the additional modes are to weakly coupled to produce any effects on this time scale. From the smallness of the reorganization energy missing from the 9d model, one can assume that, even if the TDH limit is responsible for some of behavior, the decay time will not decrease by much in a converged 19d model. This shows, that it is necessary to take a closer look at the effects of the solvent on the quantum dynamics.

In Fig. 3.74, the possible effects of a bath is sketched out. The addition of a solvent provides the system with a continuous set of bath modes, which can act as a sink for the energy released in a relaxation process. For isolated PMME a direct transition $\nu_{OD} = 1 \rightarrow 0$ is not possible, therefore the energy would have to be transferred to the normal modes as listed in Table 3.8 in a higher order process. As there is no mode in direct resonance with the system frequency, a transition of this type would also be slow. The normal modes with the best energy match are highlighted in Table 3.8: ν_{47} and the sum of ν_{24} and ν_{25} are close to the system frequency. With an additional bath, this energy mismatch can be buffered

via the solvent modes to allow processes in the form

$$h\nu_{OD} = 1 \longrightarrow \sum_i h\nu_i + h\nu_{\text{solvent}}$$

where i is a set of suitable normal modes. If the frequency band of the solvent phonons is sufficient to move the normal modes plus solvent into exact resonance with the system, this can decrease the relaxation time by orders of magnitude.

The MD calculations made To study these solvent effects, classical MD calculations for a non-polar solvent (CCl_4) similar to the one used in the experiment (C_2Cl_4) were performed. To connect the results from the classical description of the solvent to the quantum picture of the molecule the theory of linear response has been used. The friction spectrum obtained for these calculations then would have to be used in a dissipative quantum simulation (Eq. (2.101)) of the molecular model. Due to the limitations of the MD simulations the results in this work are only used as a first estimate of the possible effects. They show, that the coupling of the normal modes to the bath phonons is only efficient for modes with a frequency $\nu < 200\text{cm}^{-1}$ unless one hits a resonant mode of CCl_4. From the results of the calculations for PMME, one sees that the inclusion of a solvent potentially decreases the decay time in low frequency molecular normal modes by an order of magnitude to around 2 ps. This is only a first, relatively crude estimate, but already much closer to the experimentally observed times of $T_1 = 400\,\text{fs}$. Further improvements in this respect can be expected from a more exact treatment of environmental effects, including dissipative quantum simulations.